2013

ADVANCED STUDIES ON TRANSFER IMPEDANCE WITH APPLICATION TO AFTER-TREATMENT DEVICES AND MICRO-PERFORATED PANEL ABSORBERS

Xin Hua
University of Kentucky, huaxin0210@gmail.com

STUDENT AGREEMENT:

I represent that my thesis or dissertation and abstract are my original work. Proper attribution has been given to all outside sources. I understand that I am solely responsible for obtaining any needed copyright permissions. I have obtained and attached hereto needed written permission statements(s) from the owner(s) of each third-party copyrighted matter to be included in my work, allowing electronic distribution (if such use is not permitted by the fair use doctrine).

I hereby grant to The University of Kentucky and its agents the non-exclusive license to archive and make accessible my work in whole or in part in all forms of media, now or hereafter known. I agree that the document mentioned above may be made available immediately for worldwide access unless a preapproved embargo applies.

I retain all other ownership rights to the copyright of my work. I also retain the right to use in future works (such as articles or books) all or part of my work. I understand that I am free to register the copyright to my work.

REVIEW, APPROVAL AND ACCEPTANCE

The document mentioned above has been reviewed and accepted by the student's advisor, on behalf of the advisory committee, and by the Director of Graduate Studies (DGS), on behalf of the program; we verify that this is the final, approved version of the student's dissertation including all changes required by the advisory committee. The undersigned agree to abide by the statements above.

Xin Hua, Student

Dr. David W. Herrin, Major Professor

Dr. James M. McDonough, Director of Graduate Studies

ADVANCED STUDIES ON TRANSFER IMPEDANCE WITH APPLICATION TO AFTER-TREATMENT DEVICES AND MICRO-PERFORATED PANEL ABSORBERS

DISSERTATION

A dissertation submitted in partial fulfillment of the
requirements for the degree of Doctor of Philosophy in the
College of Engineering
at the University of Kentucky

By

Xin Hua

Lexington, Kentucky

Director: Dr. David W. Herrin, Professor of Mechanical Engineering

Lexington, Kentucky

2013

ABSTRACT OF DISSERTATION

ADVANCED STUDIES ON TRANSFER IMPEDANCE
WITH APPLICATION TO AFTER-TREATMENT DEVICES AND MICRO-PERFORATED PANEL ABSORBERS

This work is primarily comprised of five self-contained papers. Three papers are applications oriented. A common element in the first three papers is that micro-perforated panels (MPP), the permeable membranes in diesel particulate filters, and a source impedance are all modeled as a transfer impedance. The first paper deals with enhancing the performance of micro-perforated panels by partitioning the backing cavity. Several different backing schemes are considered which enhance the performance without increasing the total volume of the MPP and backing. In the second paper, a finite element modeling approach is used to model diesel particulate filters below and above the plane wave cutoff frequency. The filter itself is modeled using a symmetric finite element model and results are compared to plane wave theory. After the transfer matrix of the filters is known, it is used in three-dimensional finite and boundary element models. The third paper is a tutorial that shows how a source impedance can be modeled using transfer impedance approaches in finite element analysis. The approach used is useful for better understanding the resonance effects caused by pipes upstream and downstream of the exhaust. The fourth paper examines the best practice for the two-load transmission loss measurement. This method was integral to obtaining the measurements for validating the diesel particulate filter models. The fifth paper proposes transmission and insertion loss metrics for multi-inlet mufflers. It is shown that the transmission loss depends on the amplitude and phase relationship between sources (at the inlets) whereas insertion loss depends on both the source strength and impedance for each inlet.

KEYWORDS: transfer impedance, micro-perforated panel, diesel particulate filter, source impedance, muffler and silencer

Xin Hua
Student's Signature

17th December, 2013
Date

ADVANCED STUDIES ON TRANSFER IMPEDANCE
WITH APPLICATION TO AFTER-TREATMENT DEVICES AND MICRO-PERFORATED PANEL ABSORBERS

By

Xin Hua

Dr. David W. Herrin
Director of Graduate Studies

17th December, 2013
Date

To my family

ACKNOWLEDGEMENTS

I would like to first and foremost express my deepest gratitude to my advisor Professor David Herrin for his invaluable guidance and support, and for encouraging me to perform this work. His insightful and witty comments have made my PhD life very enjoyable. I am grateful to Professor Tingwen Wu for chairing my committee and for the great help on my research work. I would also like to thank Professor Keith Rouch, Professor Michael Seigler and Professor Qiang Ye for being my committee members and providing valuable suggestions. I am also grateful to Professor Andrew Seybert for the useful discussions even after his retirement.

My time at Lexington, Kentucky has been intellectually and socially enriched by the friends I have made. I would like to thank all my former and current colleagues, Huangxing Chen, Gong Cheng, Zhe Cui, Jun Han, Rui He, Quentin Hunsucker, Changjian Jiang, Jiazhu Li, Wanlu Li, Jiawei Liu, Jinghao Liu, Srinivasan Ramalingam, Kangping Ruan, Shishuo Sun, Peng Wang, Yitian Zhang, and Limin Zhou.

Finally and definitely not the lest, I would like to thank my parents and my wife for their support and love.

TABLE OF CONTENTS

LIST OF TABLES

LIST OF FIGURES

Chapter 1 INTRODUCTION

1.1 Background

1.1.1 Acoustic Impedance and Transfer Impedance

Sound is a result of pressure or density disturbances in a compressible medium like air and propagates as a wave (Fahy 2001). These pressure disturbances, around an ambient pressure, are known as acoustic pressure or sound pressure (p) with the unit Pascal (Pa). The velocity of these particle fluctuations is known as acoustic particle velocity (v) with unit m/s. Acoustic impedance (Z) is defined as the ratio of sound pressure p to the particle velocity v. It indicates how much sound pressure is generated by a given medium vibration. The unit of acoustic impedance is the Rayl (named after Lord Rayleigh).

Assuming that the particle velocity is continuous across an acoustic element like a perforate, the acoustic behavior of the element can be described as a transfer impedance. A transfer impedance is defined as the ratio of the pressure difference on the two sides of the element (Δp) and the particle velocity (v) through it. A transfer impedance is a type of series impedance according to the circuit analogy as shown in Figure 1.1. Accordingly, the impedance in front of the acoustic element is the summation of the transfer impedance of the element and the impedance behind it.

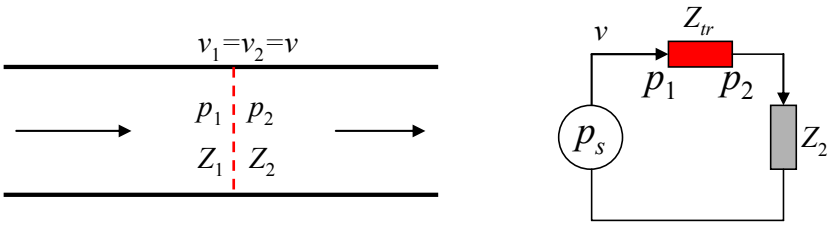

Figure 1.1 Schematic of transfer impedance (left) and circuit analogy (right).

1.1.2 Applications of Transfer Impedance

A transfer or series impedance is used to model a variety of acoustic phenomenon. For example, it is used to model perforates and micro-perforated panel absorbers, permeable membranes and screens, covers for acoustic materials, and the source impedance of a muffler.

Perforated elements are commonly used in muffler systems or for enclosure or barrier walls. In dissipative mufflers, they typically are place in front of fiber and foam absorbers to hold and protect the material. Moreover, they provide some acoustical resistance and are especially effective if the flow is substantial through the perforate. Additionally, perforates also smooth the exhaust flow inside mufflers to help minimize the back pressure and reduce the flow noise. The thickness of perforates is usually small and the particle velocities at the two sides are almost identical. Thus they are usually modeled as transfer impedance (Melling, 1973; Sullivan, 1979; Rao and Munjal, 1986; and Elnady, 2003).

Micro-perforated panels are usually made of metals or plastics with a large number of tiny holes. The hole diameter and the porosity are usually around 1 mm and 1%. They are primarily used as sound absorbers. Compared with traditional sound absorbing materials like foam and fiberglass, micro-perforated panels are light weight, nonflammable, cleanable, durable, and fiber free. Similar to perforates, micro-perforates can also be used to protect sound absorbing materials. Micro-perforates can be excellent sound absorbers if the particle velocity is high in the perforations. When a micro-perforates is positioned approximately a quarter wavelength in front of rigid wall, the particle velocity inside the holes is high and viscous friction in the holes is maximized. Micro-perforated panels have been utilized in mufflers, HVAC ducts, building interiors, engine enclosures, and noise barriers.

The permeable membranes in diesel particulate filters can also be modeled using the transfer impedance approximation (Allam and Abom, 2005). A diesel particulate filter or DPF is an after treatment device used to trap particulates from diesel engines. Though similar to catalytic converters, they differ by introducing

a less direct path through the filter. Instead of a straight-through path, exhaust gases must penetrate through a permeable cell wall before exiting the filter.

Acoustical sources in intake and exhaust systems and HVAC systems can be modeled as a combination of a source strength and a source impedance. The concept of an acoustical source impedance also arises from the circuit analogy as shown in Figure 1.2. Similar to an electrical source, an acoustical source can be divided into an ideal pressure source and a series source impedance. It follows that a source impedance is just another type of transfer impedance.

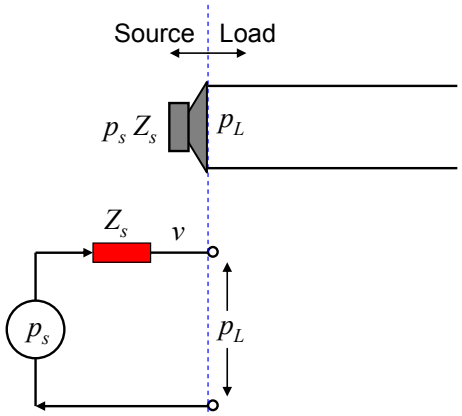

Figure 1.2 Source impedance and its circuit analogy.

The source impedance is significant in duct acoustics. It is used to characterize how reflective the source is. When the sound wave generated from the source encounters an area change (or muffler) downstream, part of the wave will reflect back towards the source as shown in Figure 1.3. Once the reflected wave hits the source, it reflects again and propagates away from the source. The amplitude and phase of the wave reflected from the source is a function of the source impedance.

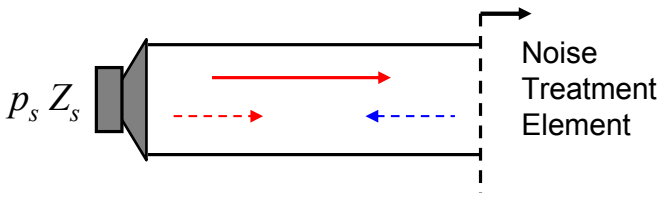

Figure 1.3 Sound propagation in ducts.

1.1.3 Gaps of Transfer Impedance Applications

This research will look at extending some of the current applications where the transfer impedance model is typically applied. This will include: a. improving the sound absorption performance of micro-perforated panels, b. developing 3D models for diesel particulate filters, c. simulating source impedances in finite element models, and d. modeling multi-inlet exhaust systems. Though transfer impedance is well understood, there are some application gaps.

Micro-perforated panel (MPP) absorbers have some notable disadvantages. Mainly, they are a banded absorber that is effective when the particle velocity is high. This occurs when the MPP is space approximately 1/4, 3/4, 5/4 … (2*(n+1)-1)/4 wavelengths away from a wall. This thesis looks at ways to improve the sound absorption performance by designing backing cavities.

A diesel particulate filter (DPF) unit, a type of exhaust after-treatment device, usually contains hundreds or thousands of parallel capillary tubes with permeable ceramic walls. The acoustical behavior of these walls is very similar to transfer impedance (Allam, 2005 and Allam, 2006). The research investigates the 3-D numerical simulation approach for modeling DPF units.

This research also examines how to include the source impedance model in a numerical simulation of a muffler. If the source impedance can be included, the acoustical behavior of the entire intake and exhaust system can be better understood.

1.2 Contributions

The research documented in this thesis is application focused and consists of five self-contained papers. The first three papers examine applications of the transfer impedance concept just described. The fourth paper examines best practices for the two-load method for measuring transmission loss. In the fifth paper, metric for multi-inlet transmission loss are suggested and validated.

1) The sound absorptive performance of micro-perforated absorbers was improved by designing special backings. Specially designed backings enhance the sound absorption at low frequencies while improving the broadband performance.

2) Integrated a one-dimensional model for diesel particulate filters into a three-dimensional model using the finite element method. Results indicate that filters can provide substantial attenuation when properly integrated into a complete exhaust system.

3) Suggested an approach for including the source impedance in a finite element model for an intake and exhaust system. The model is helpful for better understanding resonances in the inlet pipe.

4) The best practice for the two-load transmission loss measurement approach is examined. The effect of using a conical adapter to transition between the muffler inlet and outlet is examined. It is shown that adapters should be as long as possible in order to avoid contamination of the measurement at low frequencies. Additionally, it is shown that selecting a downstream microphone reference is preferred for reactive mufflers.

5) A metric for determining the insertion loss of multi-inlet mufflers is recommended. It is shown that the insertion loss is most easily determined by using a superposition approach. This approach is validated via both measurement and simulation.

1.3 Organization

The organization of this dissertation is as follows.

Chapter 2 provides some general background reviewing the definition of a transfer impedance as well as methods to measure it. The major usages of transfer impedance are reviewed. These include the modeling of perforated panels, permeable ceramic walls and acoustic source impedance.

The five papers form the bulk of this dissertation and comprise Chapters 3 though 7. Chapter 3, the first paper, suggests several methods for enhancing the performance of micro-perforated panels by partitioning the backing cavity. A micro-perforated panel (MPP) is similar to a normal perforate except the holes are slits are millimeter to sub-millimeter size. The acoustic resistance is high in the holes so they are most effective when the particle velocity is high. Accordingly, a MPP absorber is best thought of as a system comprised of the panel itself and a backing cavity. It is shown that the performance of the MPP absorber is improved by partitioning the backing cavity into multiple cavities having different lengths. This provides broadband and enhanced low frequency absorption. Several different backing schemes are considered which enhance the performance without increasing the total volume of the MPP and backing.

In chapter 4, the second paper, a procedure for simulating diesel particulate filters in muffler and exhaust systems in three-dimensions is developed. The developed method integrates the model developed by Allam and Åbom (Allam and Åbom, 2005 and Allam and Åbom, 2006) into both acoustic boundary element and finite element models so that higher frequencies can be dealt with. Plane wave propagation is assumed through the DPF unit itself, and the diesel particulate filter is modeled using a transfer matrix defined between nodes or elements on the upstream and downstream sides. This so called “element-to-element” connection permits a non-uniform sound pressure distribution on both upstream and downstream sides of the DPF unit.

Chapter 5, the third paper, first shows how an acoustical source impedance is equivalent to a transfer impedance. Then, it is shown how a source impedance can be incorporated into an acoustic finite element model. A short duct is used to model the source and a transfer impedance is used to model the source impedance. The transfer impedance is used to relate the sound pressure in the short duct to the sound pressure on the downstream side of the source.

Chapter 6, the fourth paper, reviews the two-load method to measure sound transmission loss using an impedance tube. Several practical aspects on applying this method are discussed. Since a size mismatch between a muffler and impedance tube is unavoidable (especially when measuring DPF units), the effect of adding a conical adaptor is analyzed in the first part of the chapter. The selection of the reference is investigated by comparing measured results for both upstream and downstream microphone locations. An error analysis is conducted and it is shown that selecting a downstream microphone as a reference is preferred.

In Chapter 7, the fifth paper, metrics are suggested for characterizing the sound attenuation of multi-inlet mufflers. Both transmission and insertion loss metrics are defined for the multiple inlet case and two separate procedures are used for calculations. One is a superposition method based on transfer matrix theory and the other is an impedance matrix approach. Both concepts are shown to be equivalent. Determination of the insertion loss for a two-inlet muffler was then demonstrated and validated using both procedures for a two-cylinder small engine muffler. It is shown that each approach can be extended to the n-inlet situation though the superposition approach is preferred.

Chapter 8 summarizes the current work.

Chapter 2 REVIEW OF TRANSFER IMPEDANCE AND ITS MEASUREMENTS

2.1 Transfer Impedance

Acoustic impedance (Z) is defined as the ratio of the sound pressure (p) to the particle velocity (v) and can be expressed as

$$Z = \frac{p}{v} \tag{2.1}$$

For thin and acoustically transmittable materials, the impedance difference at the front and back sides of the material is defined as the transfer impedance. It is also known as acoustic flow resistance (Ingard, 1985) or separation impedance (Morfey, 2000). Since the thickness of the material can be ignored compared to an acoustic wave length, the particle velocity at both sides of the material is usually assumed to be equal. In that case, the transfer impedance can be defined as

$$Z_{tr} = \frac{p_1 - p_2}{v} \tag{2.2}$$

where p_1 and p_2 are the sound pressure at each side of the material.

2.2 Modeling of Transfer Impedance

The transfer impedance concept is widely used to model perforated panels in HVAC ducts (Wu, 1997), permeable ceramic walls inside DPF units (Allam and Abom, 2005) and the protective films and covers of sound absorptive linings (Wu, 2003). Moreover, an acoustic source in a duct system can be modeled as a transfer impedance where the source is modeled as a combination of an ideal pressure source connected to a series (i.e., transfer) impedance.

2.2.1 Transfer Impedance for Perforates

A transfer impedance will have both real and imaginary parts. The real and imaginary parts are termed the resistance and reactance respectively. Many equations have been developed for the transfer impedance of regular perforates. For instance, Elnady (2004) definite the transfer impedance as

$$\theta = \mathrm{Re}\left\{\frac{jk}{\sigma C_D}\left[\frac{t}{F(\mu')}+\frac{\delta_{re}}{F(\mu)}f_{\mathrm{int}}\right]\right\}+\frac{1}{\sigma}\left[1-\frac{2J_1(kd)}{kd}\right] \tag{2.3}$$

$$\chi = \mathrm{Im}\left\{\frac{jk}{\sigma C_D}\left[\frac{t}{F(\mu')}+\frac{0.5d}{F(\mu)}f_{\mathrm{int}}\right]\right\}-\left(\frac{1-\sigma^2}{\sigma^2 C_D^2}\right)\frac{u_n}{6c} \tag{2.4}$$

where θ is the real part, χ is the imaginary part, t is the thickness of the perforate, d is the hole diameter, σ is the porosity, k is the wave number, c is the speed of sound, C_D is the orifice discharge coefficient, J is the Bessel function, ρ is the fluid density, v is the kinematic viscosity, μ is the adiabatic dynamic viscosity, μ'=2.179 μ, and

$$F(\mu)=1-\frac{4J_1(Kd/2)}{Kd\cdot J_0(Kd/2)} \tag{2.5}$$

$$K=\sqrt{-\frac{j\omega}{\upsilon}} \tag{2.6}$$

$$\delta_{re}=0.2d+200d^2+16000d^3 \tag{2.7}$$

$$f_{\mathrm{int}}=1-1.47\sqrt{\sigma}+0.47\sqrt{\sigma^3} \tag{2.8}$$

The normalized transfer impedance for a micro-perforated panel with circular holes can be expressed as (Maa, 1975 and 1998)

$$Z_{tr} = \frac{32\eta t}{\sigma\rho_0 c d^2}\left(\sqrt{1+\beta^2/32}+\frac{\sqrt{2}}{32}\beta\frac{d}{t}\right)+j\frac{\omega t}{\sigma c}\left(\left(1+1/\sqrt{9+\beta^2/2}\right)+0.85\frac{d}{t}\right) \quad (2.9)$$

where η is the dynamic viscosity of air, t is the thickness of the MPP, σ is the porosity, ρ_0 is the density of the air, c is the speed of sound, d is the single hole diameter, ω is the angular frequency, and

$$\beta = d\left(\frac{\rho_0\omega}{4\eta}\right)^{\frac{1}{2}} \quad (2.10)$$

is the perforate constant. For MPP absorbers with rectangular perforations, the transfer impedance can be expressed as (Maa, 2000),

$$Z_{tr} = \frac{12\eta t}{\sigma\rho_0 c d^2}\left(\sqrt{1+\beta^2/18}+\frac{\sqrt{2}}{12}\beta\frac{d}{t}\right)+j\frac{\omega t}{\sigma c}\left(\left(1+1/\sqrt{25+2\beta^2}\right)+\frac{1}{2}F(e)\frac{d}{t}\right) \quad (2.11)$$

where

$$e = \sqrt{\left(1-\frac{d^2}{4l^2}\right)} \quad (2.12)$$

is the eccentricity of the ellipse and $F(e)$ is the incomplete elliptic integral of the first kind which is expressed as

$$F(e) = \int_0^{\frac{\pi}{2}} \frac{d\theta}{\sqrt{1-e^2\sin^2\theta}} \quad (2.13)$$

2.2.2 Transfer Matrix Modeling and Numerical Modeling

The transfer impedance can be modeled as a two-port acoustic element. The four-pole matrix for the element can be expressed as

$$\begin{pmatrix} p_1 \\ v_1 \end{pmatrix} = \begin{bmatrix} 1 & Z_{tr} \\ 0 & 1 \end{bmatrix} \begin{pmatrix} p_2 \\ v_2 \end{pmatrix} \tag{2.14}$$

With the four-pole matrix, the behavior of perforates in built-up systems can be evaluated (Wu, 2003, Lee, 2004 and Tao, 2005).

In numerical simulations, such as finite or boundary element models, a node-to-node transfer relationship is commonly applied to model the transfer impedance. It is expressed as

$$\begin{Bmatrix} v_{n1} \\ v_{n2} \end{Bmatrix} = \begin{bmatrix} \frac{1}{Z_{tr}} & -\frac{1}{Z_{tr}} \\ -\frac{1}{Z_{tr}} & \frac{1}{Z_{tr}} \end{bmatrix} \begin{Bmatrix} p_1 \\ p_2 \end{Bmatrix} \tag{2.15}$$

where v_{n1} and v_{n2} are the particle velocities for both sides of the corresponding element.

2.3 Measurement of Transfer Impedance

Several approaches can be applied to measure transfer impedance. These include the impedance subtraction method (Wu, 2003), two-load method (ASTM, 2009 and Song, 2000), two-source method (Munjal, 1990 and Tao, 2003), one-cavity method (Wu, 2003), and flow resistance method (Mechel, 1965). Except for the flow resistance method, all other methods use an impedance tube, and thus the measured results are only valid below the cutoff frequency beyond which the plane wave assumption fails. The cutoff frequency f_{cut} for cylindrical impedance tubes can be determined by the equation (Pierce, 1981)

$$f_{cut} = 1.84 \frac{c}{\pi d_t} \tag{2.16}$$

where d_t is the diameter of the impedance tube. At low frequencies, Mechel (1965) showed that the static flow resistance is nearly equivalent to the acoustic resistance. Hence, the transfer impedance is sometimes approximated as the static flow resistance as a rough approximation.

2.3.1 Impedance Subtraction Method

The transfer impedance of perforates is most easily determined using the impedance subtraction method. This method is illustrated in Figure 2.1. A pair of calibrated microphones without phase mismatch is mounted in an impedance tube. The source on the left end is normally random noise, so that the impedance at all frequencies can be measured simutanously. The transfer function H_{12} is measured between microphone 1 and microphone 2. Accordingly this transfer function is the sound pressure ratio between the two microphones with amplitude and phase. The pressure reflection coefficient R_c can be obtained using the equation (ASTM, 1998)

$$R_c = \frac{B}{A} = \frac{H_{12} - e^{-jks}}{e^{jks} - H_{12}} e^{2jk(l+s)} \tag{2.17}$$

where s is the spacing between two microphones, and l is the distance between microphone 2 and the sample position, A and B denote the incident and reflected wave amplitudes respectively.

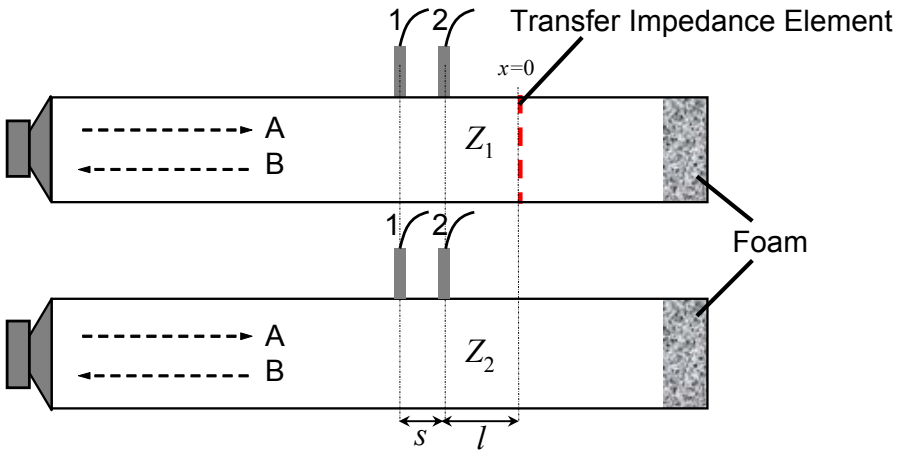

Figure 2.1 Schematic of measuring transfer impedance using impedance subtraction method.

Then, the impedance Z at the position $x=0$ is calculated using

$$Z = \frac{P}{u}\bigg|_{x=0} = \frac{A+B}{(A-B)/\rho c} = \rho c \frac{1+R}{1-R} \tag{2.18}$$

Two impedances are measured, one with the transfer impedance element inserted at $x=0$ (Z_1) and one with the element absent (Z_2). The transfer impedance of the tested element is then

$$Z_{tr} = Z_1 - Z_2 \tag{2.19}$$

Since a highly reflective termination will increase the error for measuring impedance (Bodén, 1986, Seybert, 1981 and Schultz, 2007), it is recommended to place sound absorption at the end of the impedance tube. This process has been standardized in ASTM E1050 (ASTM, 1998). In addition, the sound absorption coefficient can be determined from the measured reflection coefficient via

$$\alpha = 1 - |R|^2 \tag{2.20}$$

2.3.2 Two-Load Method

The two-load Method (ASTM, 2009 and Song, 2000) is used to determine the transfer matrix for resistive elements like fibers or foams, or mufflers or silencers. After the transfer matrix is determined, the bulk properties of a fiber or foam can be determined. Additionally, the transmission loss of an absorptive sample or muffler can be determined. The transfer impedance can also be determined after the transfer matrix is determined. A schematic illustrating the method is shown in Figure 2.2.

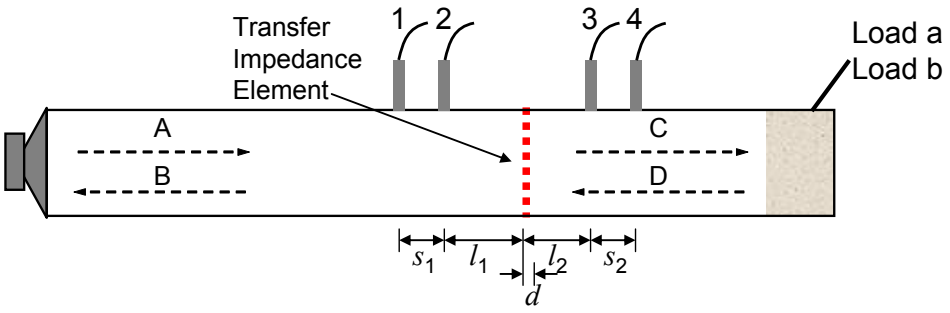

Figure 2.2 Schematic of measuring transfer impedance using two-load method.

Like the impedance subtraction method, the loudspeaker is placed at one end of the impedance tube. Two microphone positions are downstream and two upstream, and the transfer impedance element is inserted in the middle of the tube. Measurements are made between a reference and each of the four microphones. Either the source can be used as a reference or one of the microphones. Two configurations or acoustic loads are required. The acoustic load is normally modified by changing the termination. For each configuration, three transfer functions are measured if one of the microphones is used as a

reference (four transfer functions are measured if the source is used as a reference). Based on the 6 measured transfer functions, the transfer matrix T can be calculated. More details of two-load method will be discussed in Chapter 6.

Then, the sound reflection coefficient with anechoic termination can be obtained using the equation (Yoo, 2008)

$$R = \frac{T_{11} + \left(T_{12}/\rho c\right) - \rho c T_{21} - T_{22}}{T_{11} + \left(T_{12}/\rho c\right) + \rho c T_{21} + T_{22}} \tag{2.21}$$

where T_{ij} is the corresponding element of the measured transfer matrix. The transfer impedance can be expressed as

$$Z_{tr} = \rho c\left(\frac{\left(1+R\right)}{\left(1-R\right)} - 1\right) \tag{2.22}$$

2.3.3 Other Methods

There are a couple methods that are variants of the first two. One is a variant method of the two-load method, called the two-source method or two-source location method (Munjal, 1990 and Tao, 2003). The schematic of the measurement setup is shown in Figure 2.3. Instead of using different load configurations, two different source location configurations are used. It requires the source at one end of the impedance tube for the first measurement, and then the source is switched to the other end for the second measurement. Both configurations can share the same termination at the no-source end. The algorithm is the same as for the two-load method.

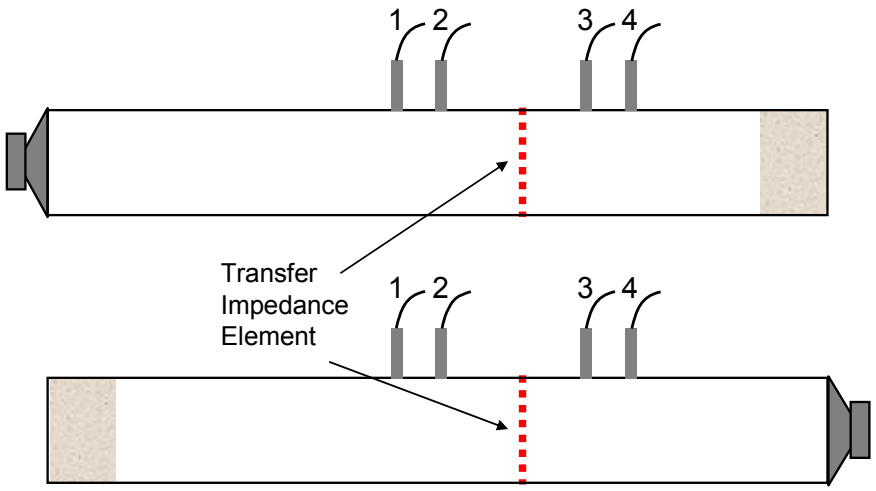

Figure 2.3 Schematic of measuring transfer impedance using two-source method.

Another measurement method is the one-cavity method (Wu, 2003), which is a variant method of the impedance subtraction method. The measurement setup is nearly identical to the impedance subtraction method except a rigid termination is used as shown in Figure 2.4. Instead of measuring the impedance Z_2 without the transfer impedance element, the impedance Z_2 is determined theoretically using

$$Z_2 = -j\rho c \cot(kL) \tag{2.23}$$

where L is the length of the cavity behind the transfer impedance element. A rigid termination is assumed.

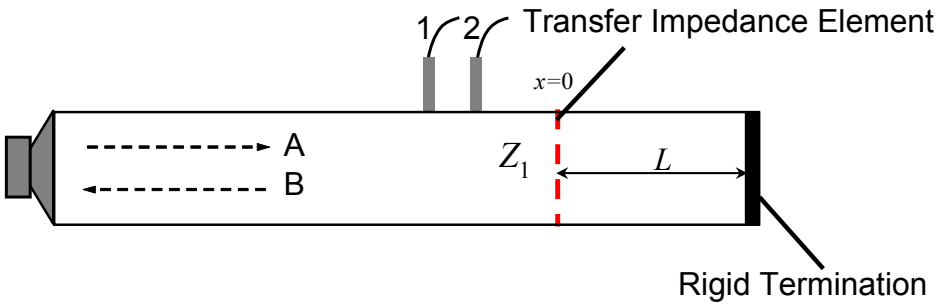

Figure 2.4 Schematic of measuring transfer impedance using rigid cavity method.

Melling and Ingard proposed another two-microphone method to measure transfer impedance at high sound pressure levels (Melling 1973, Ingard 1985). As shown in Figure 2.5, one microphone is placed anterior to the test element and the other is mounted in the rigid end of the impedance tube. The impedance behind the element can be calculated using Equation (2.23) and the impedance anterior to the element can be calculated using

$$Z_1 = \frac{H_{12}\rho c}{j\sin(kL)} \tag{2.24}$$

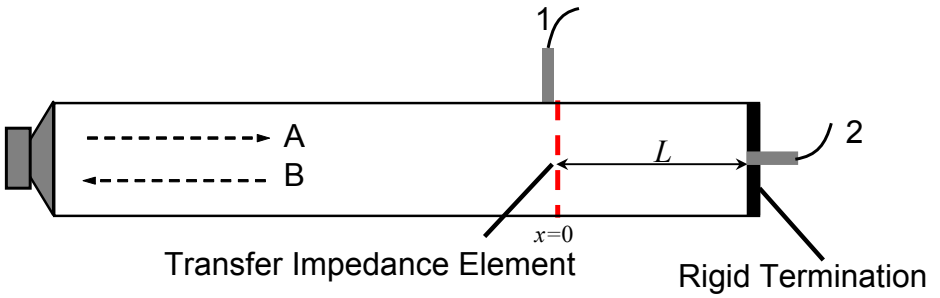

Figure 2.5 Schematic of measuring transfer impedance using Melling's two-microphone method.

2.3.4 Flow Resistance

Flow resistance (r_s), also known as airflow resistance, is defined as the ratio of static air pressure drop ΔP across a medium to the airflow velocity (u) through it. Flow resistivity (σ) is obtained by dividing the flow resistance by the thickness (t) of the medium. The flow resistance and resistivity are expressed as

$$r_s = \frac{\Delta P}{u} \tag{2.25}$$

$$\sigma = \frac{r_s}{t} \tag{2.26}$$

The flow resistance can approximate the fluctuating acoustic fields at low frequencies (Mechel, 1965, Ingard, 1985 and Pierce, 1991). This represents the resistance part of the transfer impedance. For materials that cannot easily be cut or mounted inside the impedance tube, the flow resistance test is an alternative method to obtain the transfer impedance of the material. For example, samples of the permeable membranes in diesel particulate filters are difficult to procure. However, it is important to note that this is an approximation and the reactance is ignored. However, the reactance is ignored.

The schematic of the flow resistance measurement is shown in Figure 2.6. The flow rate and the pressure difference inside the tube are measured by a hot-wire anemometer and pressure gauge respectively.

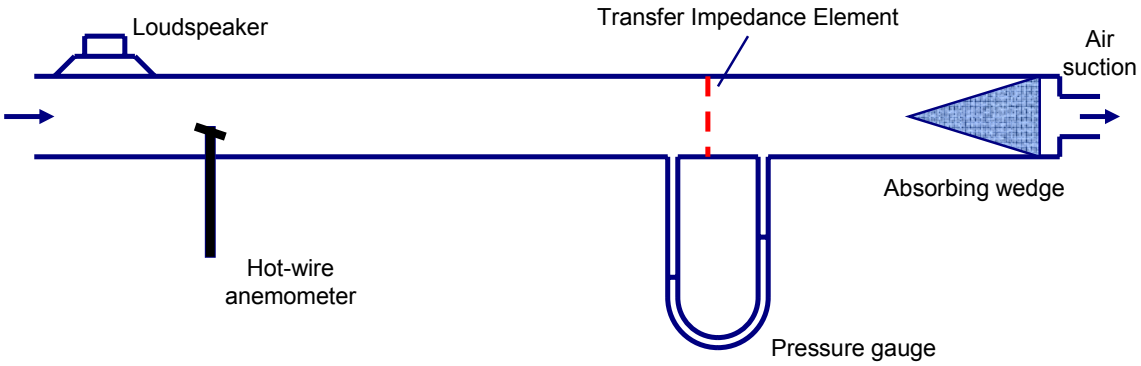

Figure 2.6 Schematic of the flow resistance measurement (Mechel, 1965).

This method has been standardized in ASTM C522-03 (ASTM, 2003) as shown in Figure 2.7. The test apparatus requires 1) a suction generator or positive air supply to produce a uniform flow rate, 2) flowmeter(s) to measure the volume velocity through the test specimen, 3) differential pressure measuring device(s) to measure the static pressure difference between the two sides of the specimen, and 4) a specimen holder. The flow resistance test rig in University of Kentucky is shown in Figure 2.8.

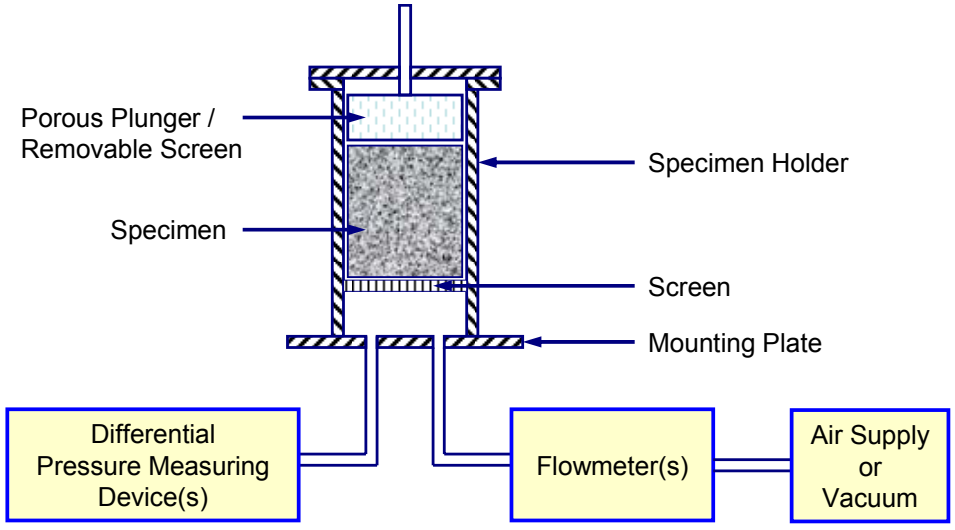

Figure 2.7 Schematic of measuring flow resistance (ASTM, 2003).

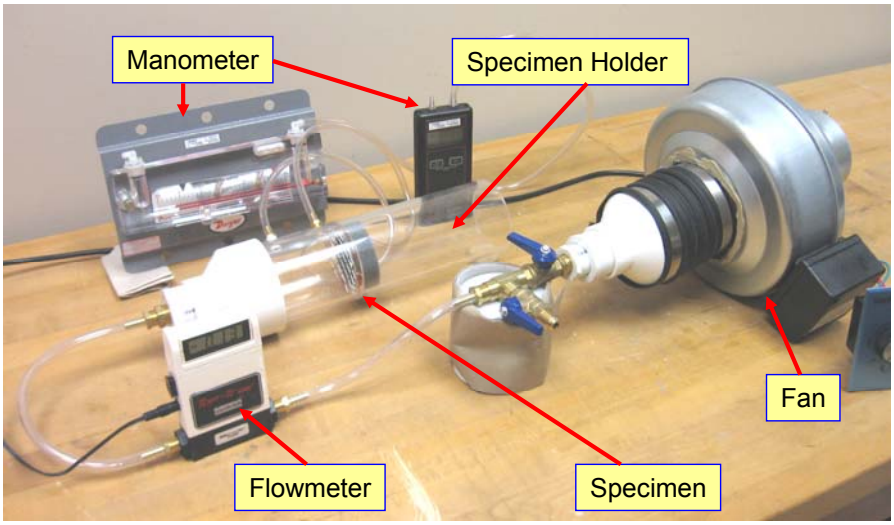

Figure 2.8 Flow resistance test rig in University of Kentucky.

A weighted piston method (Ingard, 1994 and Ingard, 2010) is an alternative to measure the flow resistance. It requires a vertically placed straight transparent tube with lubrication on the interior surface, a size-matched piston that is able to almost contact with the tube but drop smoothly under the influence of gravity, and a test sample mounted and sealed at the bottom of the tube as shown in Figure 2.9. When the piston at the top of the tube is released, it will drop and push the air downwards and out of the tube through the sample at the bottom. If the friction is ignored, the gravity of the piston will be identical to the pressure difference at the two sides of the sample. This method assumes that the piston reaches terminal velocity quickly and drops at a constant speed. The measured flow resistance r_s can be calculated using the measured falling speed v and piston weight Mg.

$$r_s = \frac{S_s Mg}{S_p^2 v} \tag{2.27}$$

where S_s and S_p are the cross-sectional area of the piston and the test sample respectively.

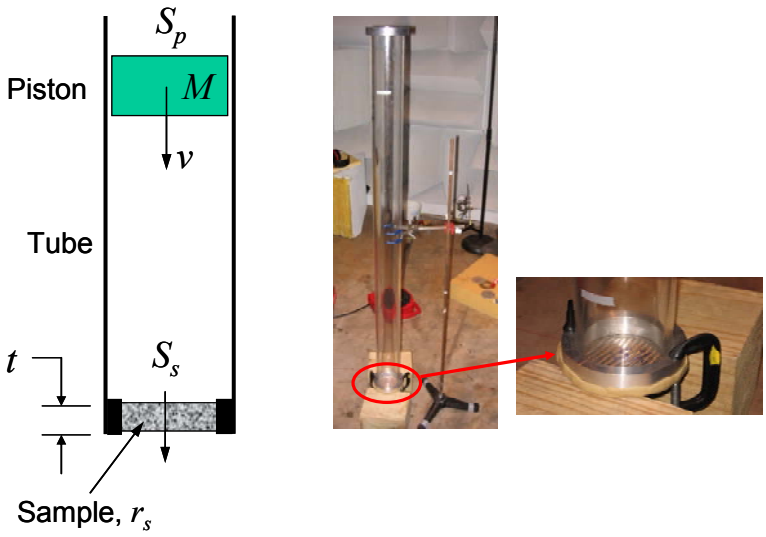

Figure 2.9 Schematic and photograph of weight piston method to measure flow resistance.

This approach is especially applicable to determine the flow resistance through the permeable membrane of a DPF (Allam and Åbom, 2005). The flow resistance (R_1) of a DPF unit can be obtained by measuring the pressure drop across the DPF under a certain flow speed. The flow resistance of the permeable membrane (R_w) can be calculated by

$$R_w = \frac{4R_1 d_{h1} LN}{A} \tag{2.28}$$

where d_{h1} is the cell dimension, L is the cell length, N is the number of open channels, and A is the cross-sectional area of the DPF.

Chapter 3 BROADBAND MICRO-PERFORATED PANEL ABSORBER

3.1 Introduction

Micro-perforated panel (MPP) absorbers are a promising replacement for traditional sound absorbing materials like fibers and foams since they are light weight, nonflammable, cleanable, durable, and fiber free. In light of these advantages, MPP absorbers have been utilized in mufflers (Allam, 2009 and Masson, 2008), HVAC ducts (Wu, 1997), building interiors (Kang, 2005), engine enclosures (Corin, 2005), and noise barriers (Pan, 2004 and Asdrubali, 2007).

MPP absorbers are normally manufactured from steel, aluminum or plastic and have uniformly distributed sub-millimeter sized holes and low porosity (typically under 5%).The first generation MPP absorbers were metal panels with circular perforations. In order to reduce the manufacturing cost, slit-shaped perforations have become common recently. Slits are pressed or cut into the metal in lieu of by laser or chemical reaction.

MPP absorbers are most often spaced from a rigid wall. In fact, it is best to think of the absorber as a system consisting of both the panel and backing cavity. Air oscillates back and forth in the perforations. Since the perforations are small, the acoustic resistance is high. Accordingly, frictional losses are greatest when the particle velocity in the pores is maximized. This roughly corresponds to spacing the panels a quarter acoustic wavelength from the wall. Hence, larger cavity depths are required to extend absorption to lower frequencies.

Whereas foams and fibers provide excellent broadband absorption above a certain frequency, the frequency range that MPP absorbers perform acceptably in is banded and much narrower due to the sound absorbing mechanism. Absorption is minimal when the particle velocity in the perforations is low. Accordingly, the spacing from the wall controls the frequencies of effectiveness and the absorption is greatest when the MPP is approximately $^1/_4\lambda$ $^3/_4\lambda$ $^5/_4\lambda$ … away from the wall where λ is the acoustic wavelength. Absorption is low in

frequency ranges corresponding roughly to multiples of a half acoustic wavelength.

Moreover, MPP absorbers generally do not perform as well as a fiber or foam even at the frequencies they are designed for. Yairi et al. (Yairi, 2005), Toyoda and Takahashi (Toyota, 2008), and Liu et al. (Liu, 2007) demonstrated that performance is comparable to traditional absorbing materials only when the backing cavity is partitioned. Probably, the most common partitioning used has been a honeycomb. In most cases, no effort has been made to vary the cavity depth.

Liu and Herrin (Liu, 2010) used boundary element simulation to investigate the reason for improved performance with partitioning. The study indicated that partitioning disrupts wave propagation behind the MPP and forces the MPP to behave like a traditional local reacting absorber. It was shown that acoustic waves that propagated normal to the panel were attenuated equally well with or without a partitioned substrate. The sound pressure due to grazing waves (propagating parallel to the MPP absorber) was essentially unaffected if partitioning was not used.

Efforts have been aimed at improving the broadband absorption of MPP absorbers. For example, double (Zou, 2005, Tao, 2005, Sakagami, 2006, and Sakagami 2009) or multi-layer (Ruiz, 2011, Bravo, 2013) MPP absorbers have been suggested. Though the absorptive performance is improved, multi-layer MPP absorbers effectively double the materials cost and are more difficult to install. Additionally, partitioning should be installed between the layers to improve their effectiveness.

Others have considered varying the cavity depth. For example, Jiang (Jiang, 2006) and Liu et al. (Liu, 2007) investigated using a triangular prism backed cavity. Sum (Sum, 2006) recommended a parallel stepped configuration. However, these approaches do not lend themselves to typical box-shaped enclosures.

The work in this chapter focuses on improving single-layer MPP absorbers by developing a partitioned backing. The backing is designed so that cavity depth is increased which provides lower frequency absorption without adding additional volume. Moreover, the cavity depth is varied so that broadband frequency absorption is achieved. The normal incidence sound absorption of the newly designed backings was measured using a square impedance tube. Diffuse incidence absorption was measured using a reverberation chamber.

Several design concepts were considered. They include two-channel and three-channel arrangements as shown in Figure 3.1. By wrapping one channel around the others, the length of a single channel can be increased by well over 50%. In doing so, the low frequency absorption will be improved. Moreover, the lengths of channels can be varied to create a broadband absorber. The newly created backings are called a folded two-channel and folded three-channel. These ideas are similar to those proposed by Wirt (Wirt, 1975) for ordinary perforated panels.

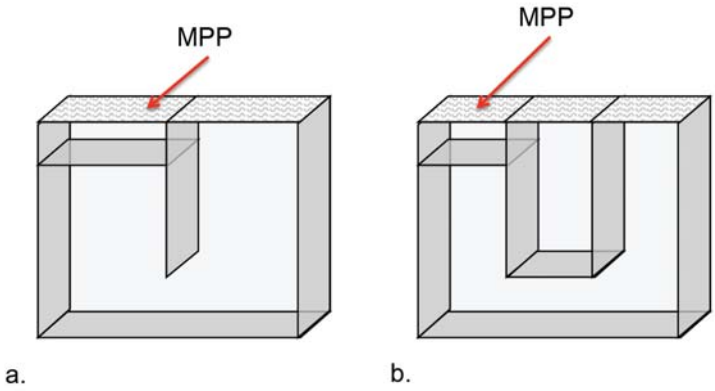

Figure 3.1 Schematics showing the folded a) two-channel and b) three-channel design concepts

3.2 Maa's Model and Equivalent Parameters

3.2.1 Maa's Model for Micro-Perforated Panels

As with other perforates, researchers have generally assumed that acoustic particle velocity is continuous due to the small thickness. Accordingly, Maa (Maa, 1975 and Maa 1998) modeled the MPP as a transfer impedance and expressed the impedance as:

$$Z_{tr} = \frac{32\eta t}{\sigma\rho_0 c d^2}\left(\sqrt{1+\beta^2/32}+\frac{\sqrt{2}}{32}\beta\frac{d}{t}\right)+j\frac{\omega t}{\sigma c}\left(\left(1+1/\sqrt{9+\beta^2/2}\right)+0.85\frac{d}{t}\right) \quad (3.1)$$

where η is the dynamic viscosity of air, t is the thickness of the MPP, σ is the porosity, ρ_0 is the density of the air, c is the speed of sound, d is the single hole diameter, ω is the angular frequency, and

$$\beta = d\left(\frac{\rho_0\omega}{4\eta}\right)^{\frac{1}{2}} \quad (3.2)$$

is the perforate constant. For MPP absorbers with rectangular perforations, Maa (Maa, 2000) proposed a modified model which is similar to the circular perforation MPP model and is expressed as,

$$Z_{tr} = \frac{12\eta t}{\sigma\rho_0 c d^2}\left(\sqrt{1+\beta^2/18}+\frac{\sqrt{2}}{12}\beta\frac{d}{t}\right)+j\frac{\omega t}{\sigma c}\left(\left(1+1/\sqrt{25+2\beta^2}\right)+\frac{1}{2}F(e)\frac{d}{t}\right) \quad (3.3)$$

where

$$e = \sqrt{\left(1-\frac{d^2}{4l^2}\right)} \quad (3.4)$$

is the eccentricity of the ellipse and $F(e)$ is the incomplete elliptic integral of the first kind which is expressed as

$$F(e) = \int_0^{\frac{\pi}{2}} \frac{d\theta}{\sqrt{1 - e^2 \sin^2 \theta}} \tag{3.5}$$

The impedance at the surface of a conventional MPP absorber is expressed as

$$Z = Z_{tr} - j \cot\left(\frac{\omega D}{c}\right) \tag{3.6}$$

where D is the air cavity depth behind the MPP. It can be observed that the porosity, thickness, hole diameter, and the cavity depth govern the performance of the MPP absorber. The effect of varying the cavity depth is shown in Figure 3.2 .

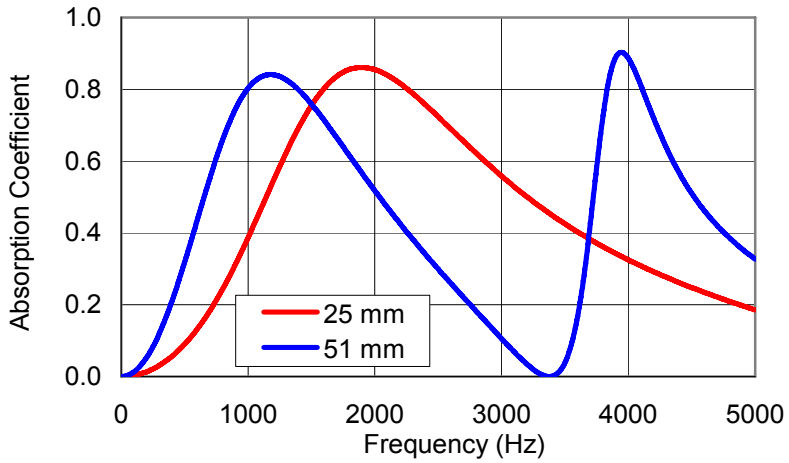

Figure 3.2 Typical absorption coefficients for a MPP absorber with different cavity depths.

Notice that an extremely low absorption band cannot be avoided when the cavity depth is approximately half of an acoustic wavelength. Moreover, increasing the cavity depth lowers the frequency of the high absorption band.

3.2.2 Equivalent Parameters based on Maa's Model

At first glance, Maa's model seems difficult to apply to less expensive second-generation MPP absorbers where slits are pressed or cut into metal. Although the sound absorbing mechanism is the same, Maa's equations cannot be applied directly due to the slit being irregular in shape (i.e., not circular or elliptical). Moreover, the slit is often pressed through the material at an angle and the dimensions of the slit are not consistent through the thickness.

However, Liu et al. (Liu, 2013) used a nonlinear least-square data-fitting (NLLSF) algorithm to estimate equivalent parameters (usually porosity and hole size) from the measured absorption. The absorption of a sample with a given cavity depth is first measured and then a least-square data fitting algorithm is used to select a porosity and hole diameter that minimizes the error. The algorithm has been used to investigate dust or water contamination and the effect of manufacturing variability.

A collection of micro-perforated panels with different porosities was measured. Their equivalent porosities and diameters were calculated to characterize each sample using the method above. The scatter plot for equivalent parameters is shown in Figure 3.3. The results show that the equivalent diameters cluster around 0.25 mm while the equivalent porosities vary dramatically from 2 to 8 percent. Accordingly, the equivalent porosity for this particular manufacturing approach can be related to manufacturing parameters like cutting depth and time. Figure 3.4 compares NLLSF absorption coefficients with 2 and 8 percent porosity. From the results, it is evident that the MPP with 2 percent effective porosity performs better.

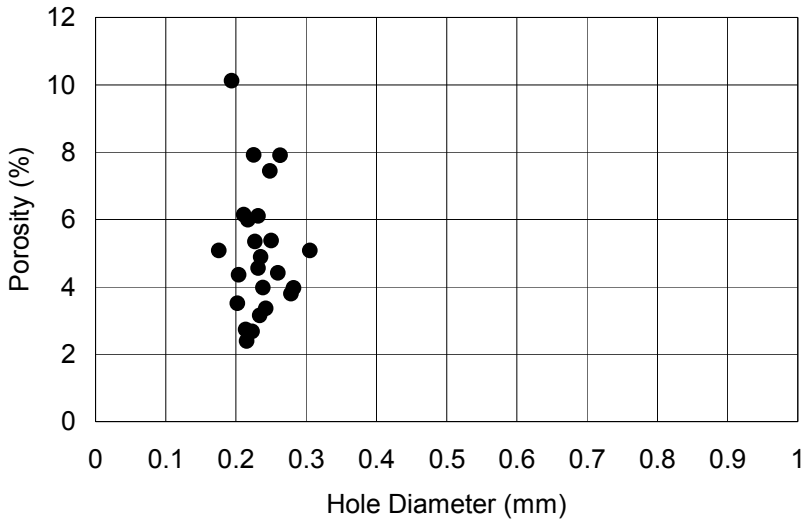

Figure 3.3 Geometric parameter scatter plot for a class of MPP with slit perforations.

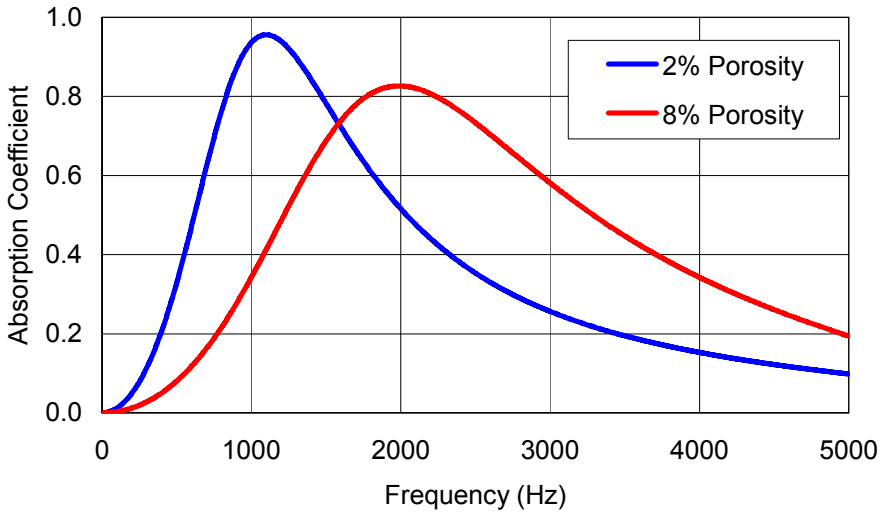

Figure 3.4 Comparison of fitted sound absorption for equivalent porosities of 2 and 8 percent. Equivalent hole diameter is 0.25 mm and the backing cavity depth is 25 mm.

In the current effort, the method was used to determine the equivalent porosity and hole size of a MPP with slit perforations so that Maa's theory could be used for the simulation models. The sound absorption of an MPP sample was measured using ASTM E1050 (1998) with a two-inch cavity behind it. Maa's model was then fitted to the measured data from 200 to 1500 Hz. The fitted equivalent hole size and porosity were 0.26 mm and 8% respectively. The fitted and measured absorption are compared in Figure 3.5.

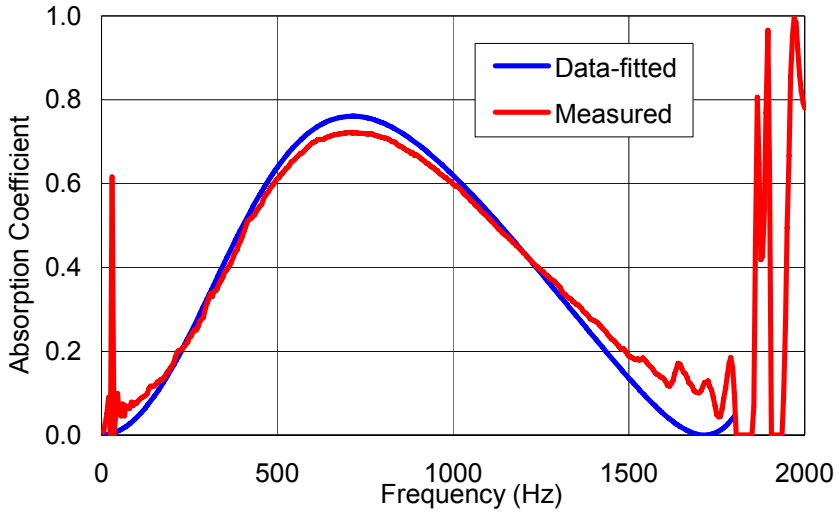

Figure 3.5 The fitted and measured absorption of a selected MPP with a backing cavity depth of 51 mm.

3.3 Substrate Backing to Improve MPP Absorbers

3.3.1 Plane Wave Model for Parallel Substrate MPP Absorbers

Using the electrical analogy, the MPP can be modeled as being in series with the impedance of the backing cavity. The MPP is both resistive and reactive whereas the backing air cavity is purely reactive. Figure 3.6(a) illustrates the analogous electrical circuit.

In a similar manner, consider the case where the cavity is partitioned into a series of channels with varying depths as shown in Figure 3.6(b). It can be assumed that the sound pressure is constant on the front surface of the MPP. In that case, the combined transfer impedance and reactance for each channel may be considered in parallel with its neighbor as shown in Figure 3.6(b).

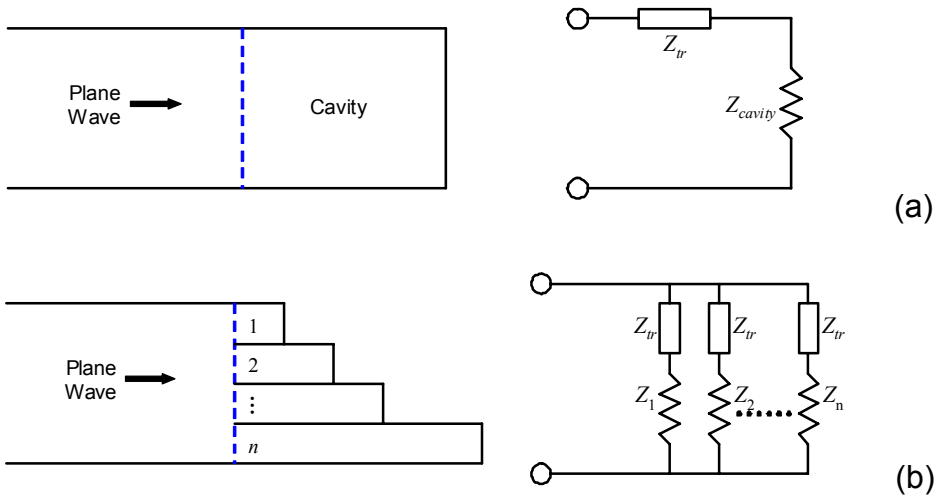

Figure 3.6 Electrical analogy of traditional MPP absorber (a) and multi-channel MPP absorber (b).

The total volume velocity at the surface of the MPP is equal to the sum of the volume velocities in the individual channels. Thus,

$$uS = \sum_{i=1}^{n} u_i S_i \tag{3.7}$$

where u is the particle velocity at the surface of the MPP and u_i for the individual channels. By assuming the sound pressure P is constant across the surface of the MPP, the particle velocities can be written in terms of specific acoustic impedances and sound pressure. Thus,

$$\frac{PS}{Z} = \sum_{i=1}^{n} \frac{PS_i}{Z_i} \tag{3.8}$$

where Z_i and S_i are the acoustic impedance (Equation (3.6)) and cross-sectional area of the ith air channel respectively. Therefore, the impedance of the multi-channel MPP absorber can be expressed as

$$Z = \frac{1}{\sum_{i=1}^{n} \frac{s_i}{Z_i}} \tag{3.9}$$

where s_i is the cross-sectional area ratio between the ith channel and the total area. The normal incident absorption coefficient of the multi-channel MPP absorber can be calculated using the equation

$$\alpha = \frac{4R\rho_0 c}{\left(R + \rho_0 c\right)^2 + X^2} \tag{3.10}$$

where R and X are the real and imaginary part of Z respectively.

The simplest case is a two-channel MPP absorber. In that case, the impedance can be expressed as

$$Z = \frac{1}{\frac{s_1}{Z_1} + \frac{s_2}{Z_2}} \tag{3.11}$$

In a similar manner, a three-channel absorber can be expressed as

$$Z = \frac{3Z_1 Z_2 Z_3}{Z_1 Z_2 + Z_2 Z_3 + Z_3 Z_1} \tag{3.12}$$

If it is assumed that each channel shares the same area. In that case, the lengths of the channels govern the impedances for each channel.

3.3.2 Optimization of J-Shape Three-Channel MPP Absorber

In order to inherent the folded three channel concept but to utilize the backing volume sufficiently, a J-shape three-channel model is proposed and investigated as shown in Figure 3.7. The maximal thickness D of the absorber is pre-determined. The first and second channels behavior maintains the same as the three-channel model. The third channel, the folded channel, is not modeled simply as a straight duct but as two straight ducts connected by a simple expansion chamber.

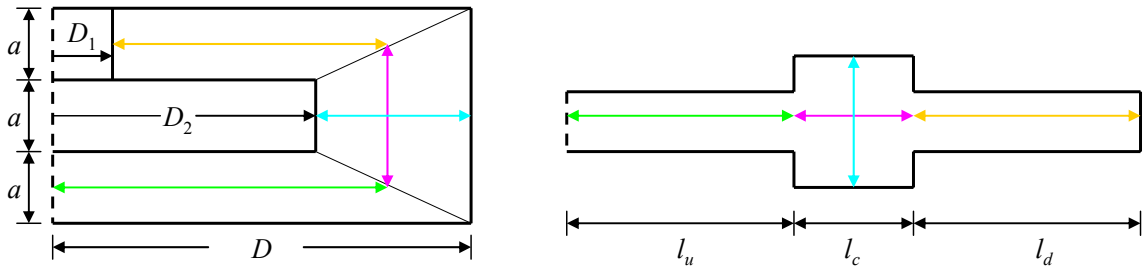

Figure 3.7 J-shape three-channel MPP absorber and the simple expansion chamber approximation of the third channel.

The cross-sectional area of each channel is assumed as a square with the dimension a. And then, the length l_u and area s_u of the upstream duct of the third channel is $(D+D_2)/2$ and a^2 respectively. The length l_c and area s_c of the chamber is $2a$ and $a(D-D_2)$ respectively. The length l_d and area s_d of the downstream duct is $(D+D_2)/2-D_1$ and a^2. Using transfer matrix theory, the surface impedance of the third channel with MPP can be expressed as

$$Z_3 = Z_{tr} - \frac{T_{11}}{s_u T_{21}} \tag{3.13}$$

where

$$T_{11} = \cos(kl_u)\cos(kl_c)\cos(kl_d) - \frac{s_c}{s_u}\sin(kl_u)\sin(kl_c)\cos(kl_d)$$
$$- \frac{s_d}{s_c}\cos(kl_u)\sin(kl_c)\sin(kl_d) - \frac{s_d}{s_u}\sin(kl_u)\cos(kl_c)\sin(kl_d) \tag{3.14}$$

$$T_{21} = s_u \sin(kl_u)\cos(kl_c)\cos(kl_d) + s_c \cos(kl_u)\sin(kl_c)\cos(kl_d)$$
$$- \frac{s_u s_d}{s_c}\sin(kl_u)\sin(kl_c)\sin(kl_d) + s_d \cos(kl_u)\cos(kl_c)\sin(kl_d) \tag{3.15}$$

3.4 Numerical and Experimental Validation of Multi-Channel MPP Absorbers

3.4.1 Boundary Element Model Validation

In order to validate the plane wave models described before, the folded two- and three-channel backings were simulated using the boundary element method (BEM). For the two-channel case, the length ratio of the shorter channel to the total cavity depth is 15%. For the three-channel case, the ratio of the shortest channel D_1 to the total cavity depth D is 10%. The length ratio of the middle channel to the total cavity depth is approximately 40%. The BEM mesh is shown in Figure 3.8. A 95 mm × 95 mm square duct was created with an MPP spaced 100 mm away from the end. The MPP is modeled as a transfer relationship that relates the respective particle velocities (v_{n1} and v_{n2}) to sound pressures (p_1 and p_2) on either side of the MPP. In matrix form, this can be expressed as

$$\begin{Bmatrix} v_{n1} \\ v_{n2} \end{Bmatrix} = \begin{bmatrix} \frac{1}{Z_{tr}\rho_0 c_0} & -\frac{1}{Z_{tr}\rho_0 c_0} \\ -\frac{1}{Z_{tr}\rho_0 c_0} & \frac{1}{Z_{tr}\rho_0 c_0} \end{bmatrix} \begin{Bmatrix} P_1 \\ P_2 \end{Bmatrix} \tag{3.16}$$

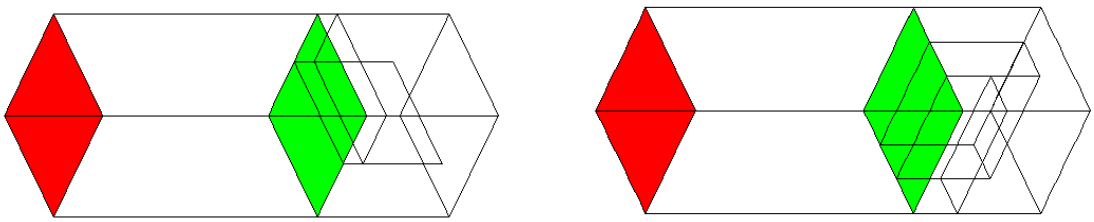

Figure 3.8 Boundary element models of two-channel (left) and J-shape three-channel (right) MPP absorbers. Unit velocity boundary condition is on red and MPP transfer relation is on green.

The walls of the cavity behind the MPP are assumed to be rigid. A unit velocity boundary condition is applied to the surfaces at the left as shown in Figure 3.8. The sound pressure at field points positioned in front of the MPP is determined and then both the impedance and normal incidence absorption are calculated.

3.4.2 Experimental Validation in Square Impedance Tube

Both the folded two and three channel designs were measured experimentally using a square impedance tube as shown in Figure 3.9. The tube is made of aluminum with the cross-sectional area 95 mm × 95 mm. The plane wave cutoff frequency is approximately 1800 Hz. A two-microphone method with random noise excitation was applied to measure the absorption coefficient based on ASTM E1050 (ASTM, 1998)

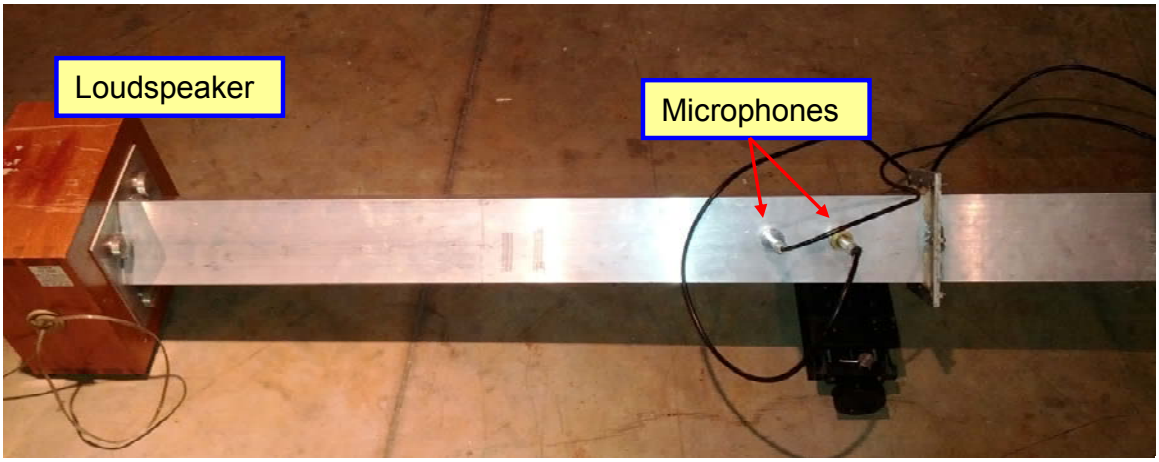

Figure 3.9 Square impedance tube.

Before the MPP absorber measurement, the absorption of the empty impedance tube was measured with a rigid piston at the termination. The average absorption coefficient is as low as around 0.04 as shown in Figure 3.10, which indicate that the square impedance tube is qualified.

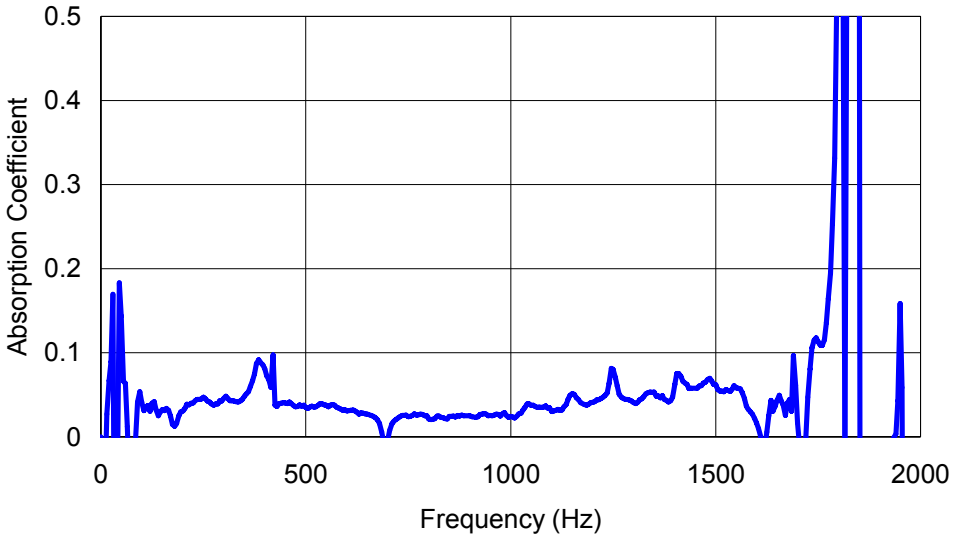

Figure 3.10 Absorption of the empty square impedance tube.

The two different backing cavities were constructed and tested, and are shown in Figure 3.11. The partition sheets were made from 1.1 mm thick steel. All potential gaps were sealed with plumber's putty.

Figure 3.11 Photos of two-channel (left) and J-shape three-channel (right) backing design inside square impedance tube.

Figure 3.12 shows the normal incidence absorption comparison of the MPP with the folded two-channel backing. The total cavity depth is 100 mm. The plane wave and BEM simulations compare well to measured results below 1200 Hz. The absorption behavior at low frequency is greatly improved compared to the MPP absorber with an empty cavity. It is suggested that suitable broadband absorption in an enclosure could be obtained by combining the folded two-channel with an empty cavity backing.

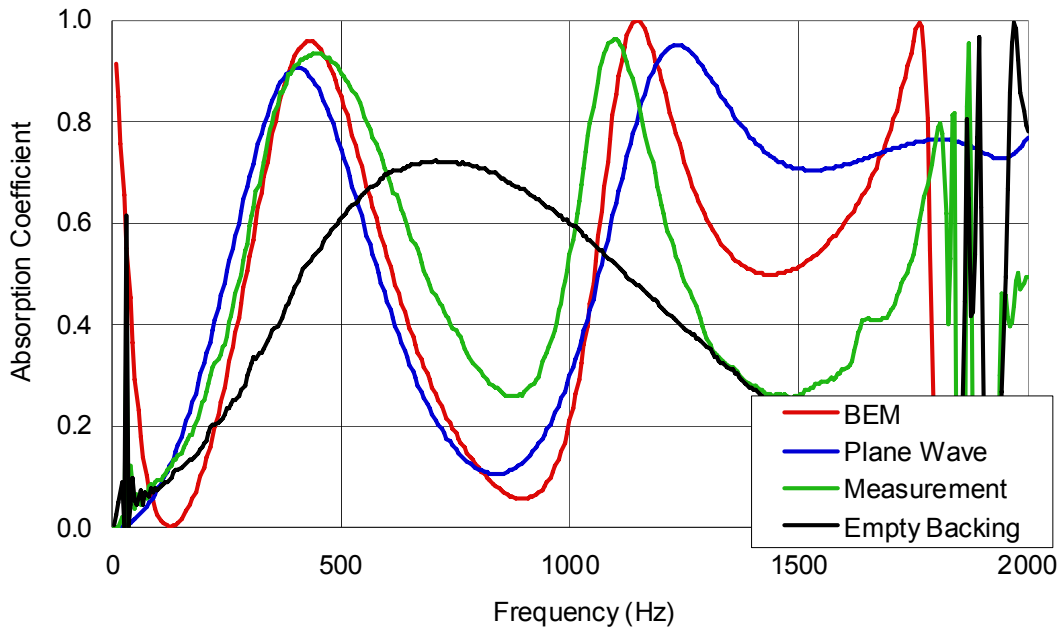

Figure 3.12 Measured absorption for the folded two-channel MPP absorber compared to plane wave and BEM simulation. Measurement with empty cavity is also shown.

The normal incidence absorption comparison for an MPP with the folded three-channel backing is shown in Figure 3.13. Again, plane wave and BEM simulation agree generally well with measurement. Moreover, the absorption performance is improved significantly when compared to an empty backing.

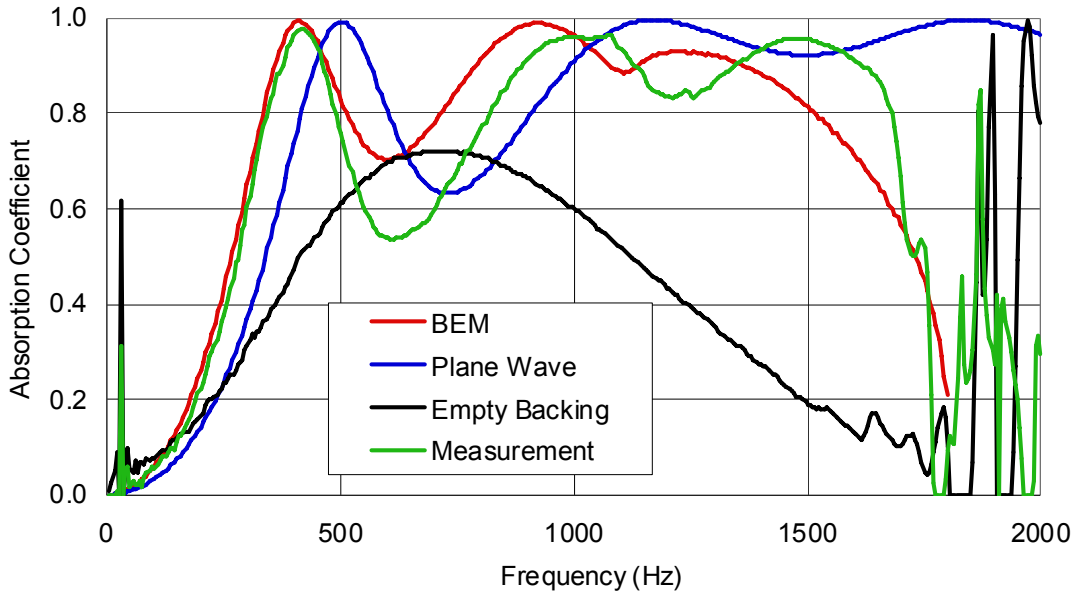

Figure 3.13 Measured absorption for the J-shape three-channel MPP absorber compared to plane wave and BEM simulation. Measurement with empty cavity is also shown.

3.4.3 Experiment in Reverberation Room

A small reverberation chamber, similar to an alpha cabin but larger, (Jackson, 2003) was used to measure the absorption of different panel constructions. The chamber is 10.87 m³ with no parallel walls and the noise source was a distributed mode loudspeaker, which produces a roughly diffuse sound field. More information about the reverberation chamber used can be found in the reference (Jackson, 2003).

The test procedure was to clamp the MPP absorber to the top of a frame utilizing 1-inch wide steel strips held in place by rare earth magnets. The cavity could then be filled with the backing substrate as required and the absorption coefficients of 100 mm deep systems were measured and compared. The absorption coefficient was measured in a manner analogous to ASTM C423 (ASTM, 2009) (except in a smaller room). A sample backing is shown in Figure 3.14.

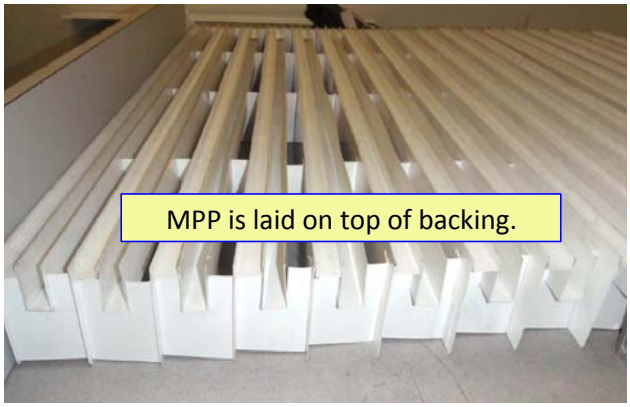

Figure 3.14 Backing constructed for testing in small reverberation room.

Figure 3.15 compares the diffuse field absorption factor for the J-shape three-channel and empty 100 mm cavity backings. Notice that the folded three-channel backing greatly enhances the absorption over the entire frequency range.

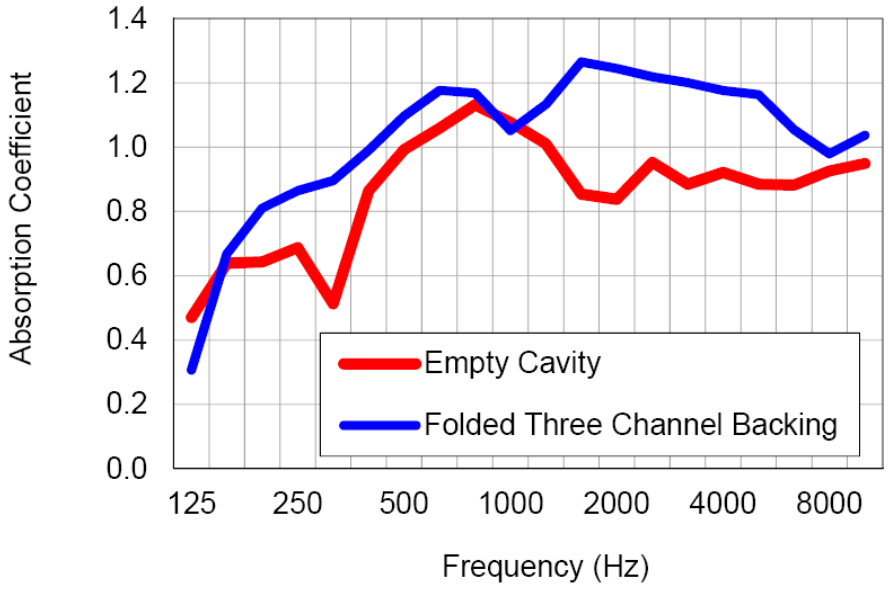

Figure 3.15 Measured diffuse field absorption for the J-shape three-channel MPP absorber and empty backing designs.

3.5 Schizophonium Backing to Improve MPP Absorbers

L. S. Wirt suggested another backing design named *schizophonium* (Wirt, 1975), which consists of an acoustical horn coupled to a closed cavity as shown in Figure 3.16. A small gap is between the mouth of the horn and the end of the cavity that is created by the horn exterior and the cylinder.

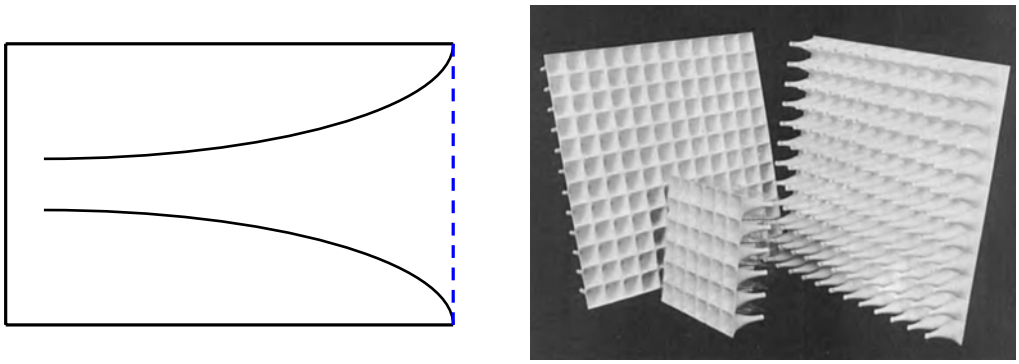

Figure 3.16 Schizophonium backing (Wirt, 1975).

An approximated plane wave model for the *Schizophonium* backing is a series of short straight ducts with different diameters. The MPP at the *Schizophonium* opening is still modeled as transfer impedance and the other end is modeled as the rigid termination. The cutoff frequency of this model is controlled by the cross-sectional area of the absorber. The key parameters of the *Schizophonium* backing MPP absorber are the length of the absorber, l, the cross-sectional area of the horn mouth, S_1, the cross-sectional area of the absorber, S_2, and the porosity of the MPP, σ.

The effects of varying the area ratio S_1:S_2 are investigated as shown in Figure 3.17 and Figure 3.18. Compared with the behavior of traditional MPP absorber (the blue curve in Figure 3.18 that the area ratio is 100%), the first lobe is narrowed and shifted to the lower frequency and the second lobe is broadened

with the decrease of the area ratio. In other words, the *Schizophonium* backing MPP absorber is tunable without changing the total volume of the absorber. Moreover, the mid-frequency sound absorption is significantly enhanced due to the second lobe.

The effects of varying MPP porosity, σ, are also investigated as shown in Figure 3.19 and Figure 3.20. The porosity is mainly controlling the absorption level so that a most desirable absorption behavior can be achieved.

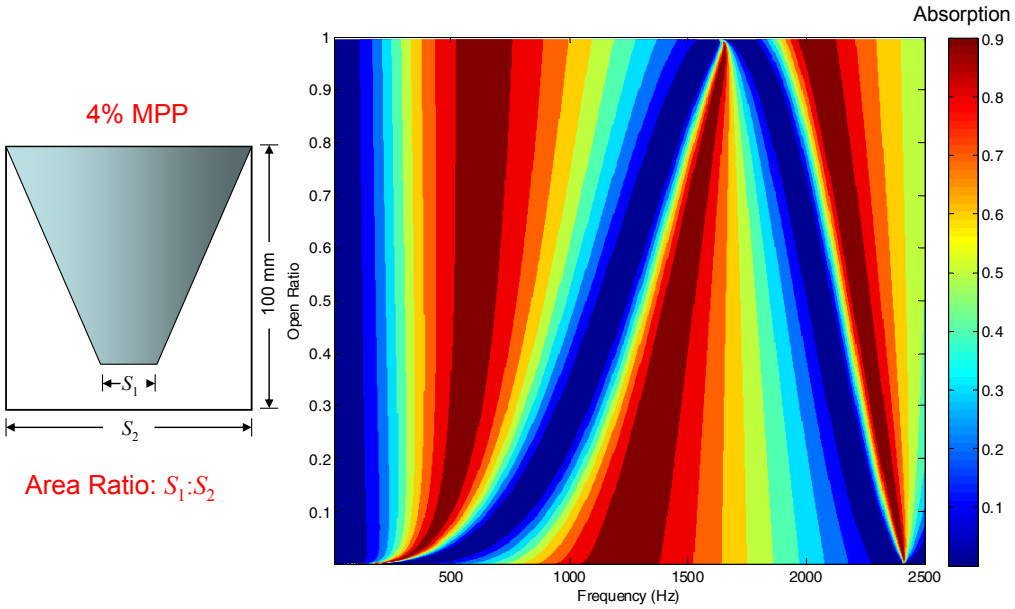

Figure 3.17 Area ratio effect on Schizophonium backing MPP absorber.

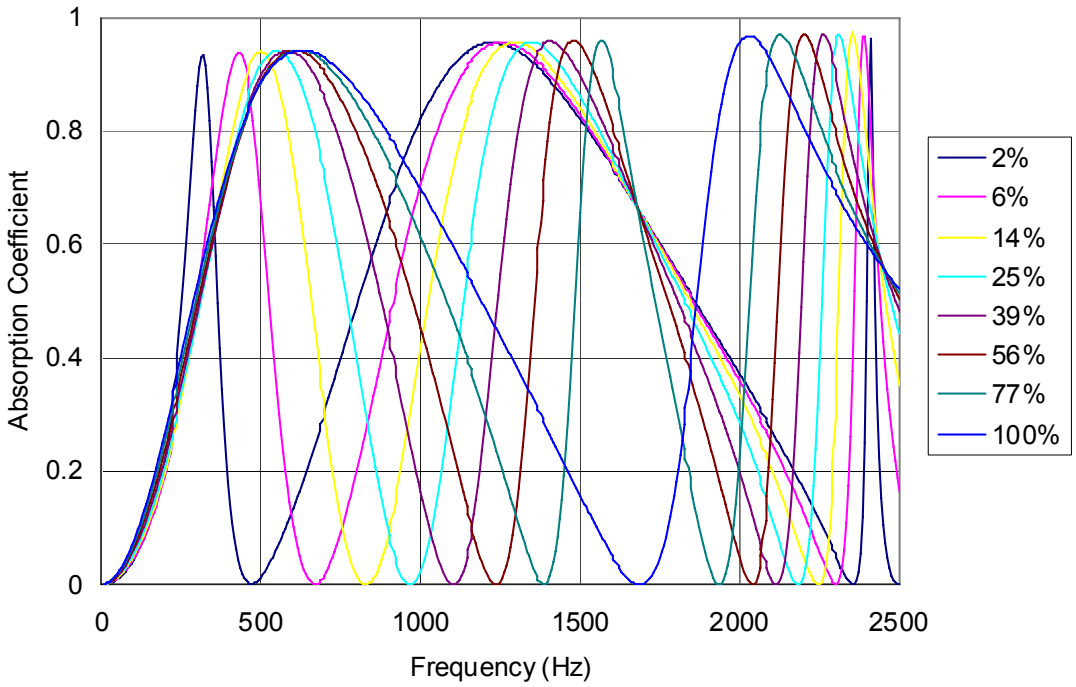

Figure 3.18 Absorption coefficient of Schizophonium backing MPP absorber with different area ratio.

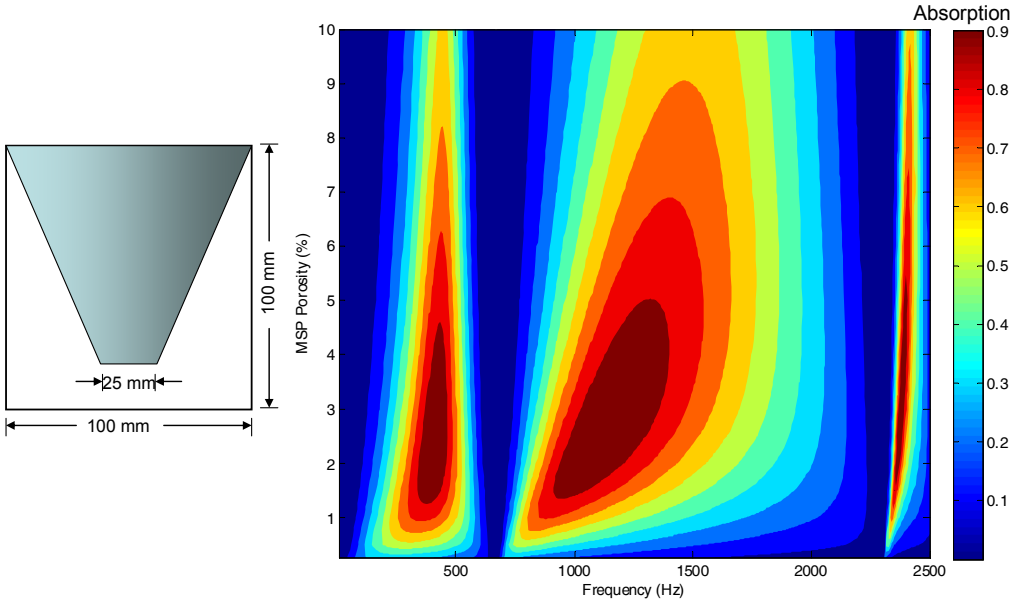

Figure 3.19 MPP porosity effect on Schizophonium backing MPP absorber.

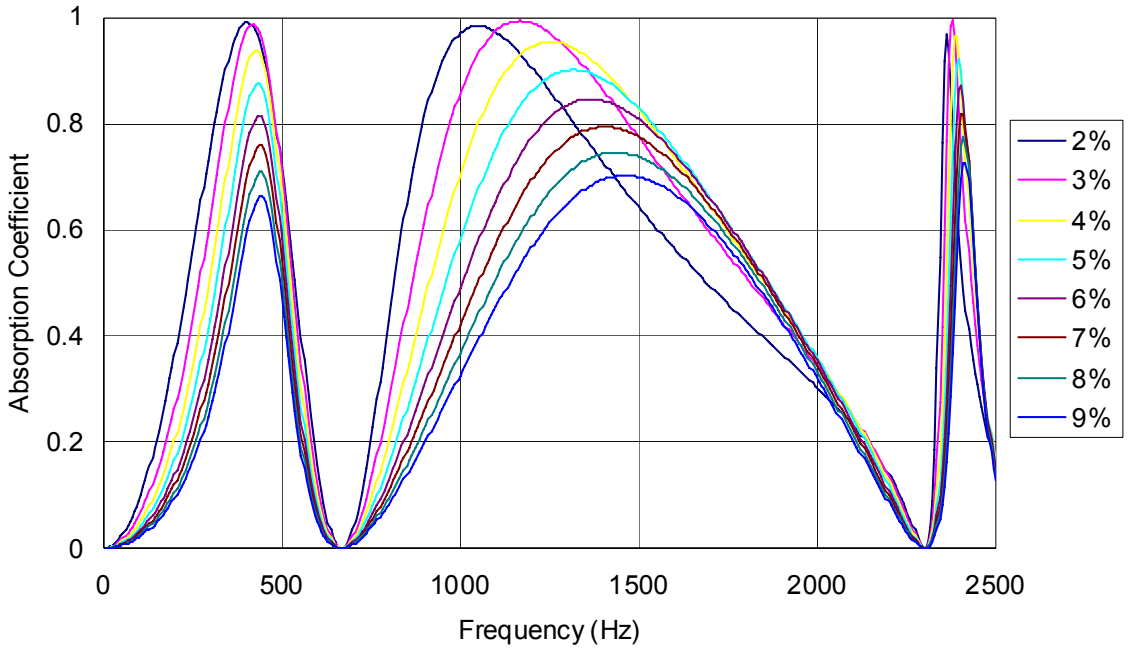

Figure 3.20 Absorption coefficient of Schizophonium backing MPP absorber with different MPP porosity.

The *Schizophonium* backing MPP absorber inherits the disadvantage of traditional MPP absorber that they are both banded absorbers. And thus, single *Schizophonium* backing MPP absorber cannot achieve a broadband sound absorption. However *Schizophonium* backing MPP absorber is an ideal complement to traditional MPP absorbers. Figure 3.21 indicates that traditional MPP absorber performs poorly at low frequency sound absorption below 300 Hz, while the *Schizophonium* backing MPP absorber performs very well between 200 and 400 Hz. Moreover, the traditional MPP absorber has drawback between 1200 Hz and 1800 Hz, however, *Schizophonium* backing MPP absorber performs well at that frequency range. Therefore, by arranging a traditional MPP absorber and a *Schizophonium* backing MPP absorber in parallel, a broadband sound absorbing behavior can be achieved.

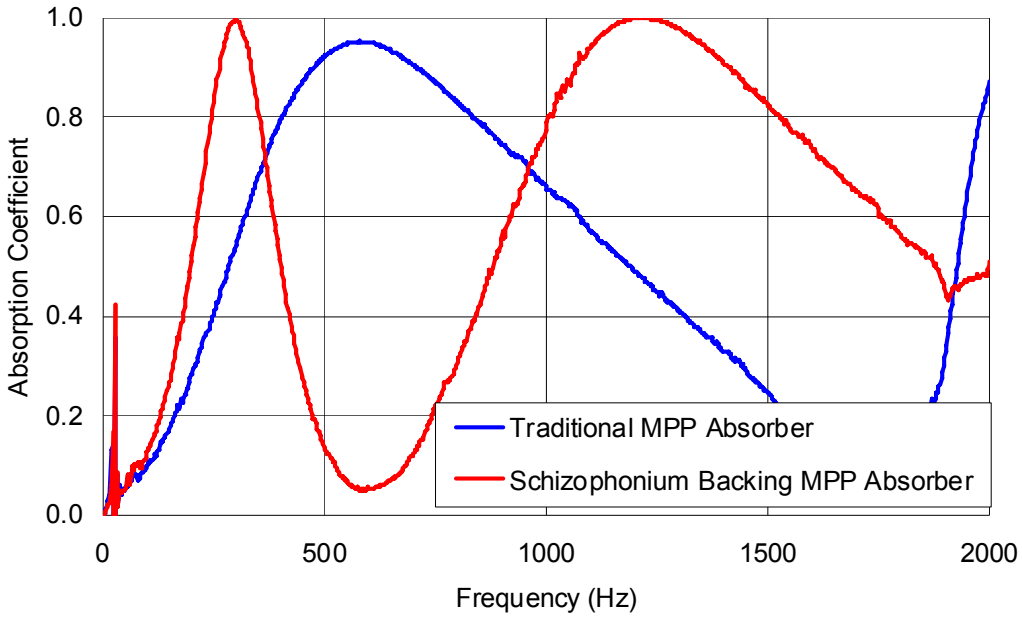

Figure 3.21 Measured absorption coefficient of Schizophonium backing MPP absorber and traditional MPP absorber with 100 mm backing cavity.

3.6 Triangular Prism Backing to Improve MPP Absorbers

Another possible backing design is the so-called triangular prism backing. The bottom portion of the triangular prism in the backing cavity is large porous, which is acoustically transparent. It allows the sound wave to travel into the two parallel cavities that are created by the triangular prism exterior and the outer box as shown in Figure 3.22.

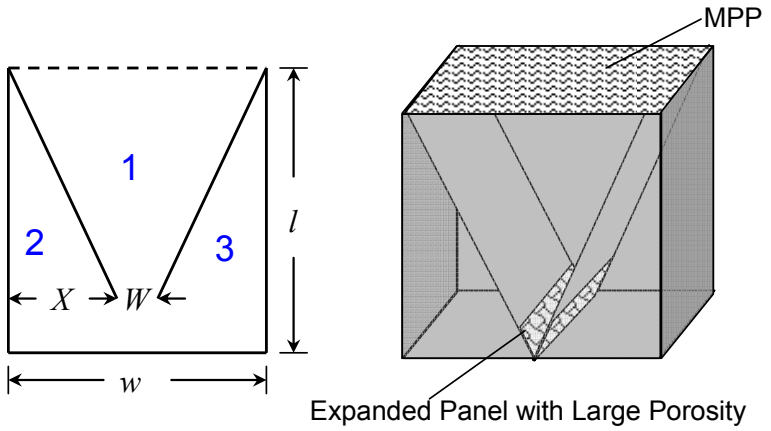

Figure 3.22 Schematics of triangular prism backing MPP absorbers.

An approximated plane wave model is a series of short straight ducts with different diameters (labeled as 1 in Figure 3.22) connected with two series of short straight ducts with different diameters (labeled as 2 and 3 in Figure 3.22) in parallel. The cutoff frequency for this model is controlled by the cross-sectional area of the cavity. The essential parameters are the porosity of the MPP σ, the depth of the backing cavity, l, the width of the open mouth, W, and the width of the cavity, w. The parameter effects are investigated by assuming the cavity depth and width are both 100 mm.

The effects of varying MPP porosity, σ, are investigated as shown in Figure 3.23. The main effect of varying the MPP porosity is on the magnitude of the sound absorption coefficient. And the porosity range between 2% and 4% is the optimal. The low absorption bands around 800 Hz and 1900 Hz do not shift by varying the porosity.

The effects of varying the prism opening width, W, are investigated as shown in Figure 3.24. The main role for the width is to shift the low absorption frequency bands. Similarly to the *Schizophonium* backing, triangular prism backing MPP absorber is also likely to be an important complement to traditional MPP absorber.

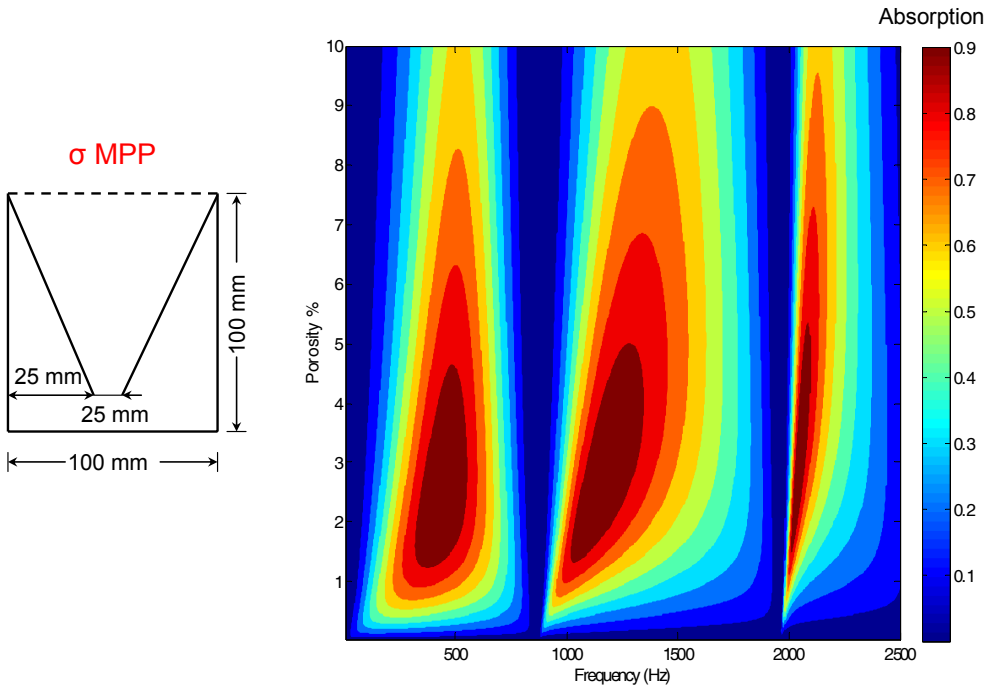

Figure 3.23 MPP porosity effect on triangular prism backing MPP absorber.

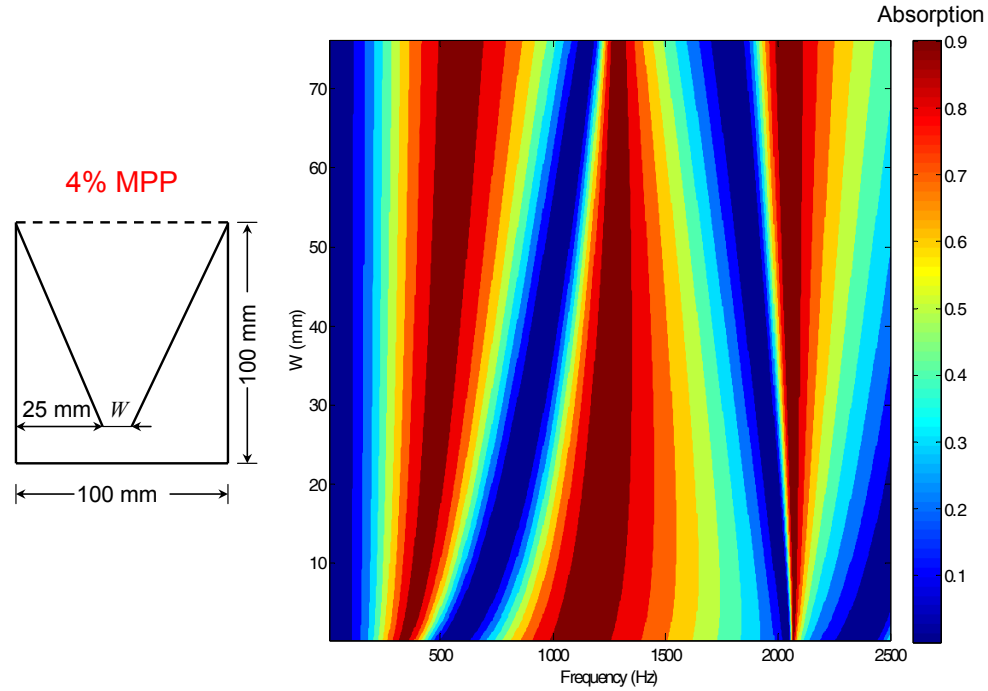

Figure 3.24 Open width effect on triangular prism backing MPP absorber.

3.7 Summary

By partitioning the backing cavity to create multiple channels in parallel, the performance of an MPP absorber can be improved without increasing the cavity volume. Maa's model was utilized to characterize irregularly shaped slits by nonlinear data fitting. Using the fitted hole diameter and porosity, plane wave theory was then used to simulate and help select the backing channel depths.

The two-channel design improves the absorption at low frequencies. However, a low absorption band in the higher frequency range is inevitable. A three-channel design is able to enhance low frequency performance as well as providing broadband absorption. By folding the longest channel, the material space can be utilized much more effectively. The absorption for both the folded two-channel and three-channel absorbers was measured. The normal incidence absorption was found using a square impedance tube, and the diffuse field absorption was found using a small reverberation room. The results show that the performance can be improved substantially by adding a multi-channel backing.

Two additional backing concepts have been proposed: a) a *schizophonium* and b) triangular prism backing based on work by Wirt (1975). The performance using these backings complements the performance for a MPP absorber with no backing. Broadband absorption can be achieved by using the specially designed backings in portions of the backing cavity while leaving other parts of the cavity empty.

Chapter 4 DIESEL PARTICULATE FILTERS

4.1 Introduction

A diesel particulate filter or DPF is an after treatment device used to trap and capture soot from diesel engines. DPF units are devices which remove from 50 to over 90 percent of diesel particulate matter from exhaust gases. Though similar to catalytic converters, they differ by introducing a less direct path through the filter. Instead of a straight-through path, exhaust gases must penetrate through a porous cell wall before exiting the filter (Figure 4.1). A number of different filter materials have been used including ceramic and silicon carbide materials, fiber wound cartridges, knitted silica fiber coils, ceramic foam, wire mesh, and sintered metal structures. Though their primary purpose is to reduce exhaust pollutants, diesel particulate filters are also effective sound attenuation devices in exhaust systems. Indeed, traditional mufflers and silencers are sometimes no longer needed because the filter is so effective. Since 2007, nearly all diesel powered trucks and buses in the United States have used DPF systems and will continue to use them for the foreseeable future. Since 2011, the off-highway equipment industry has begun using DPF systems.

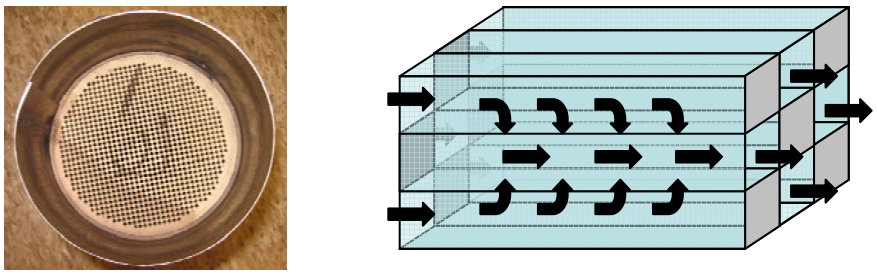

Figure 4.1 Photograph (left) and schematic view (right) of a diesel particulate filter.

Allam and Åbom completed much of the foundational work by perfecting a transfer matrix model for a DPF unit. Inputs to their model included the overall

dimensions of the unit, cell density, and wall permeability and thickness (Allam and Åbom, 2005 and Allam and Åbom, 2006). Plane wave propagation was assumed through the DPF unit and the exhaust system as a whole.

The work detailed in this chapter is a natural progression of their research. Since duct dimensions are frequently large for diesel engines like those used in trucks, off-highway equipment, and maritime applications; there is a need to consider three-dimensional wave behavior in the airspace upstream and downstream. For such cases, numerical simulation will be necessary.

The developed method addresses these concerns by integrating the model developed by Allam and Åbom (Allam and Åbom, 2005 and Allam and Åbom, 2006) into both acoustic boundary element and finite element models so that higher frequencies can be dealt with. Plane wave propagation is assumed through the DPF unit itself. Accordingly, a transfer matrix is specified across the DPF from an element (or FEM element face) on the upstream side to a corresponding element (or FEM element face) on the downstream side. This so called "element-to-element" connection permits a non-uniform sound pressure distribution on both upstream and downstream sides of the DPF unit. However, the sound is assumed to propagate one-dimensionally through the DPF unit itself.

Assuming plane wave propagation through a filter element seems reasonable for straight through flow catalysts like catalytic converters. However, DPF units are more complicated to model due to their wall-flow nature. Accordingly, the plane wave assumption was investigated both experimentally and using analysis.

4.2 Transfer Matrix Theory on DPF

Allam and Åbom (Allam and Åbom, 2005 and Allam and Åbom, 2006) assumed plane wave propagation in the DPF channels utilizing sound pressure and volume velocity as state variables. Accordingly, the transfer matrix for the DPF ($\mathrm{T_{DPF}}$) unit relates the sound pressures p_{in} and p_{out} at the inlet and outlet to the respective particle velocities (v_{in} and v_{out}) and cross-sectional areas (S_{in} and S_{out}) via

$$\begin{Bmatrix} p_{in} \\ S_{in}v_{in} \end{Bmatrix} = [\mathbf{T_{DPF}}] \begin{Bmatrix} p_{out} \\ S_{out}v_{out} \end{Bmatrix} \tag{4.1}$$

Allam and Åbom (Allam and Åbom, 2005 and Allam and Åbom, 2006) combined five transfer matrices (T_{IN}, T_I, T_{II}, T_{III} and T_{OUT}) together as shown in Figure 4.2 to develop the transfer matrix (T_{DPF}) for the DPF unit.

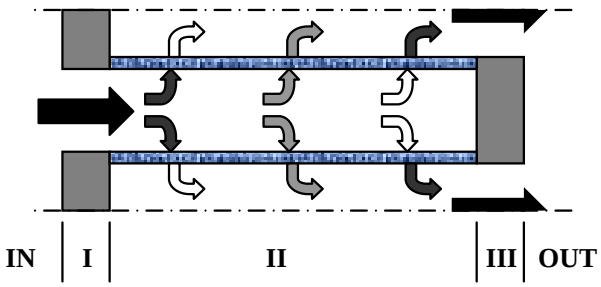

Figure 4.2 Schematic illustrating transfer matrices in a DPF.

Thus,

$$\mathbf{T_{DPF}} = \begin{bmatrix} T_{11}^{DPF} & T_{12}^{DPF} \\ T_{21}^{DPF} & T_{22}^{DPF} \end{bmatrix} = \mathbf{T_{IN}}\mathbf{T_I}\ \mathbf{T_{II}}\ \mathbf{T_{III}}\mathbf{T_{OUT}} \tag{4.2}$$

where T_{IN} and T_{OUT} are simply identity matrices modeling the area contraction and expansion at the inlet and outlet respectively. T_I and T_{III} simulate the short ducts at the inlet and outlet to the channels with lengths corresponding to the plug length. Assuming that the plug length (l) is very small compared to an acoustic wavelength, the quantity kl where k is the wavenumber will likewise be small and the small angle assumption is appropriate. In that case, T_I and T_{III} are expressed as

$$\mathbf{T_I} = \mathbf{T_{III}} = \begin{bmatrix} 1 & j\rho_0\omega l/S \\ 0 & 1 \end{bmatrix} \tag{4.3}$$

where ρ_0 is air density, ω is angular frequency, and S is cross-sectional area of a channel (Allam and Åbom, 2005 and Allam and Åbom, 2006).

If low Mach number flow is included (Allam and Åbom, 2005, Munjal, 1987, Renneberger, 1967 and Davies, 1988) and Bernoulli's equation is applied at the inlet, $\mathrm{T_{IN}}$ can be expressed as

$$\mathbf{T_{IN}} = \begin{bmatrix} 1 & 1.5\dfrac{\rho_0 c_0 M}{S_{\mathrm{IN}}}\left(\dfrac{1}{m^2}-1\right)+j\dfrac{\rho_0 \omega l}{S_{\mathrm{IN}}} \\ 0 & 1 \end{bmatrix} \tag{4.4}$$

where M is the Mach number, c_0 is the speed of sound, m is the open area ratio (smaller than 1), and S_{IN} is the cross-sectional area of the inlet to the DPF (See Figure 4.2).In a similar manner, the transfer matrix at the outlet ($\mathrm{T_{OUT}}$) can be written as

$$\mathbf{T_{OUT}} = \begin{bmatrix} 1 & 2\dfrac{\rho_0 c_0 M}{S_{\mathrm{OUT}}}\left(1-\dfrac{1}{m}\right)+j\dfrac{\rho_0 \omega l}{S_{\mathrm{OUT}}} \\ 0 & 1 \end{bmatrix} \tag{4.5}$$

where S_{OUT} is the cross-sectional area of the outlet to the DPF.

Allam and Åbom (Allam and Åbom, 2005 and Allam and Åbom, 2006) determined $\mathrm{T_{II}}$ using a mode-matching scheme. The permeable walls were modeled using a transfer impedance relationship. The acoustic transfer impedance was approximated as the static flow resistance via Darcy's Law (Pierce, 1991) and the transfer reactance was assumed to be negligible. This assumption is expedient since the transfer impedance for an actual filter can then be determined by simply measuring the pressure drop.

Mechel et al. (Mechel, 1965) demonstrated over 30 years ago that the real part of the transfer impedance (the acoustic resistance) could be approximated at low frequencies by the static flow resistance. Consequently, the transfer impedance for a permeable wall of a DPF can be expressed as

$$Z_{tr} = R_w = \frac{4R_1 d_{h1} LN}{A} \tag{4.6}$$

where d_{h1} is the cell dimension, L is the cell length, N is the number of open channels, and A is the cross-sectional area of the DPF.

Since dimensions of channels are small, attenuation due to thermo-viscous friction inside the channels should be included. According to Keefe (Keefe, 1984) in cylindrical ducts, the complex air density (ρ) and speed of sound (c) can be obtained by

$$\rho = \frac{\rho_0}{1 - F(s)} \tag{4.7}$$

and

$$c = c_0 \frac{(1 - F(s))^{1/2}}{\left[1 + (\gamma - 1)F\left(\sqrt{\nu} s\right)\right]^{1/2}} \tag{4.8}$$

where γ is specific heat ratio and ν is Prandtl number. s is a dimensionless parameter, which represents the ratio of hydraulic channel radius (a) to the viscous boundary-layer thickness,

$$s = \frac{a}{\sqrt{\eta / \rho_0 \omega}} \tag{4.9}$$

where η is the shear viscosity coefficient and $F(s)$ is defined in terms of Bessel functions ($J_0(x)$ and $J_1(x)$) as

$$F(s) = \frac{2}{\sqrt{-j}s} \frac{J_1\left(\sqrt{-j}s\right)}{J_0\left(\sqrt{-j}s\right)} \tag{4.10}$$

Equations (4.7) to (4.10) are used to determine straight duct transfer matrices.

It should be noted that a simplified model for the channel is being used. Allam and Åbom (Allam and Åbom, 2006) used a full mode matching model to explore transverse effects in a square channel, and determined that the aforementioned simplified solution for visco-thermal waves in straight pipes is a good approximation.

4.3 Validation of One-Dimensional Assumption

The authors implemented the Allam and Åbom model (Allam and Åbom, 2005 and Allam and Åbom, 2006) using the acoustic finite element method (FEM) to determine T_{II}. This is an approach that might be preferred in industry because commercial software is readily available to implement the model. By taking advantage of symmetry, a section of the filter can be modeled rather than using the mode-matching scheme.

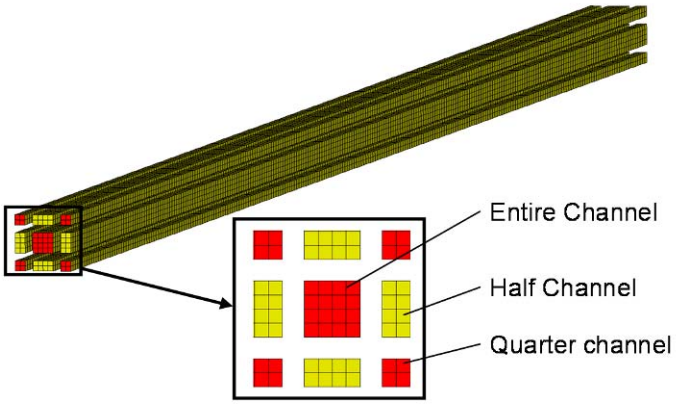

Figure 4.3 FEM model of a DPF channel and neighboring channels.

A single channel and parts of eight adjoining channels are modeled as shown in Figure 4.3. The permeable membrane between channels can be modeled using a transfer relationship that relates the respective particle velocities (v_{n1} and v_{n2}) and sound pressures (P_1 and P_2) on either side of the permeable membrane via

$$\begin{Bmatrix} v_{n1} \\ v_{n2} \end{Bmatrix} = \begin{bmatrix} \frac{1}{Z_{tr}} & -\frac{1}{Z_{tr}} \\ -\frac{1}{Z_{tr}} & \frac{1}{Z_{tr}} \end{bmatrix} \begin{Bmatrix} P_1 \\ P_2 \end{Bmatrix}. \tag{4.11}$$

To determine the transfer matrix $\mathrm{T_{II}}$, a unit velocity v is applied to the element faces indicated in Figure 4.3.

The transfer matrix can most easily be determined by using the modified four-pole parameters defined by Wu et al. (Wu, 1998). Parameters A*, B*, C* and D* can be obtained by

$$\begin{aligned} A^* = D^* &= p_1\big|_{v_1=1} \\ C^* = B^* &= p_2\big|_{v_1=1} \end{aligned} \tag{4.12}$$

where $p_1$and p_2 are acoustic pressures at inlet and outlet respectively for a unit velocity at the inlet. $\mathrm{T_{II}}$ can be expressed as

$$\mathbf{T_{II}} = \begin{bmatrix} A^*/C^* & \left(B^* - A^*D^*/C^*\right)/S \\ \left(1/C^*\right)S & \left(-D^*/C^*\right) \end{bmatrix} \tag{4.13}$$

where S is the cross-sectional area (S_{IN} = S_{OUT}). The transmission loss (TL) of the DPF unit itself can be written in terms of overall transfer matrix ($\mathrm{T_{DPF}}$) as

$$TL = 20\log\left|\frac{1}{2}\left(T_{11}^{DPF} + \frac{T_{12}^{DPF}S}{\rho_0 c_0} + \frac{\rho_0 c_0 T_{21}^{DPF}}{S} + T_{22}^{DPF}\right)\right| \tag{4.14}$$

The results using the acoustic FEM model were compared against those using mode-matching with good agreement for both of the filters indicated in Table 4-1. SIDLAB, which implements the theory developed by Allam and Åbom, was used for the one-dimensional analyses (Elnady, 2006). Results are shown in Figure 4.4 for Filter 1.

Table 4-1 Diesel Particulate Filter Properties

Filter name	Filter 1	Filter 2
Diameter/length (mm)	150/250	270/304
Channels/m^2	3.1×10^5	3.1×10^5
Channel width (mm)	1.44	1.5
Wall thickness (mm)	0.355	0.3
R_1 (Ns/m^3)	184.1	42
Temperature (°C)	20	32
Mach Number	0.02	0.0

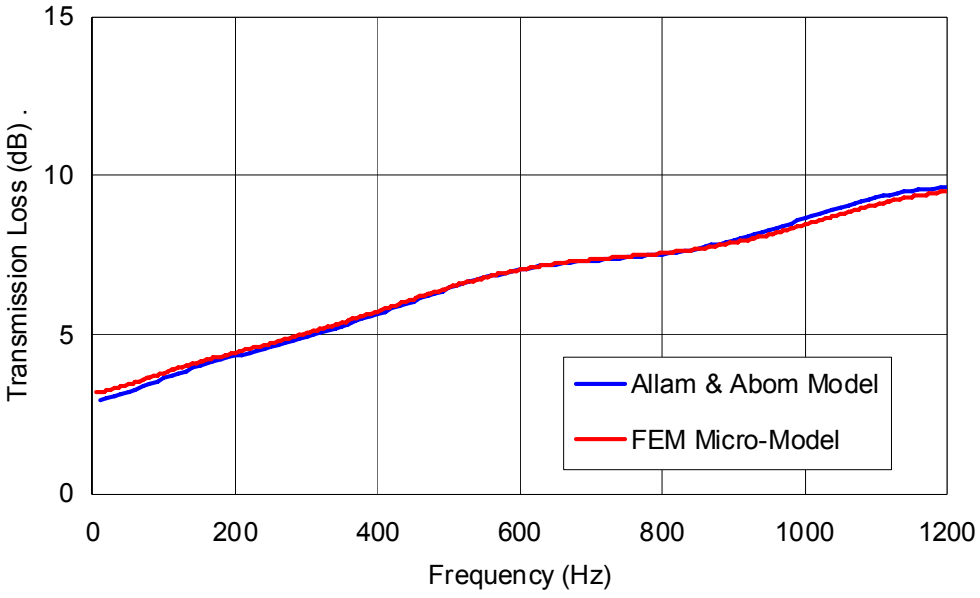

Figure 4.4 Transmission loss results for Filter 1 (M = 0.02).

After validating the acoustic FEM methodology, an analysis for an 81-channel model was performed to assess if a DPF lends itself to the one-dimensional assumption. A quarter-symmetry model was used and is shown in Figure 4.5. A velocity of 1 m/s was applied to the center cell and the sound pressure at the termination of the neighboring cells was reported. Figure 4.6 shows the resulting sound pressure for neighboring cells. The results justify the one-dimensional premise since the sound pressure two channels away from the excited channel is 20 dB less. Accordingly, the results substantiate that a one-dimensional model of the DPF unit itself is proper.

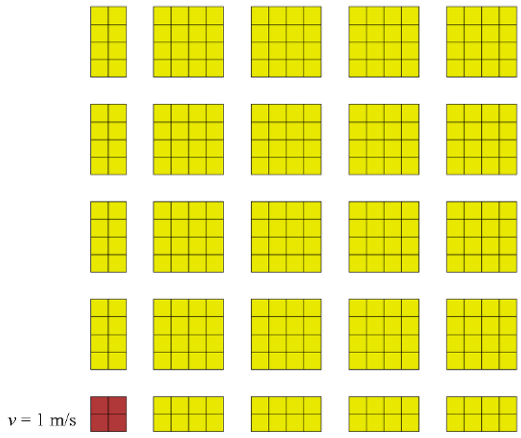

Figure 4.5 81-channel FEM model assuming quarter symmetry.

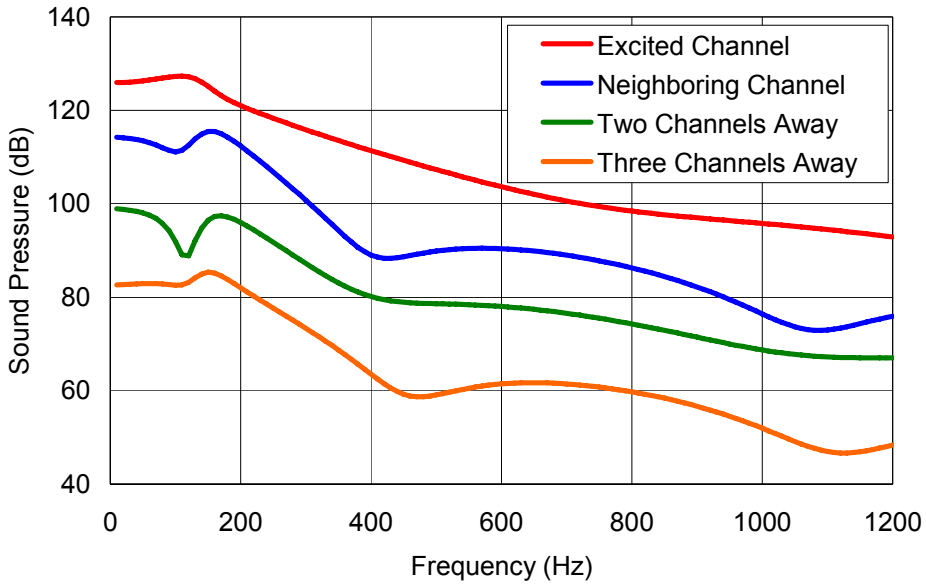

Figure 4.6 Sound pressure levels of the 81-channel FEM model. Sound pressure levels shown are at the channel terminations.

4.4 Numerical Simulation of Exhaust System with DPF

4.4.1 Boundary Element Simulation

The BEM macro model is based on a so-called “element-to-element” four-pole connection between two BEM substructures (Lou, 2003 and Jiang, 2010). The four-pole transfer matrix of the DPF connects a surface element on the upstream side to a corresponding surface element on the downstream side. Therefore, even though the four-pole transfer matrix is one-dimensional, the “element-to-element” connection permits a non-uniform sound pressure distribution on both the upstream and downstream sides of the DPF unit. This “element-to-element” connection, an assumption imposed to the system, seamlessly integrates the one-dimensional four-pole transfer matrix into a three-dimensional boundary element model.

A summary of the BEM substructuring technique is provided. To begin with, it is assumed that a muffler is divided into two substructures as shown in Figure 4.7, and that the two substructures are connected to each other by a DPF.

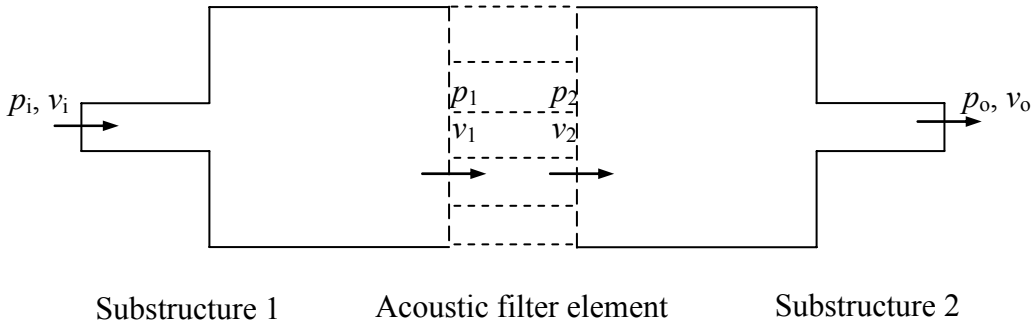

Figure 4.7 Two boundary element substructure connected by an acoustic filter element.

Although Figure 4.7 only shows two empty expansion chambers, the inside of these two substructures can still contain complex internal components, such as extended inlet/outlet tubes, thin baffles, perforated tubes, and sound absorbing materials. Let p_i and v_i denote the sound pressure and the particle velocity in the longitudinal direction, respectively, at the inlet of the first substructure, and p_o and v_o denote the corresponding variables at the outlet of the second substructure. Also, p_1 and v_1 are the variables at the outlet of the first substructure, and p_2 and v_2 are at the inlet of the second substructure. The sound pressure and particle velocity need not be uniform at any cross-section. Therefore, each p or v variable used in this section actually represents a vector and the length of each vector depends on the number of boundary elements used at each cross-section. For substructure 1, the sound pressures at the inlet and the outlet are related to the corresponding particle velocities by an impedance matrix.

$$\begin{Bmatrix} \mathbf{p_i} \\ \mathbf{p_1} \end{Bmatrix} = \begin{bmatrix} \mathbf{Z_{11}} & \mathbf{Z_{12}} \\ \mathbf{Z_{21}} & \mathbf{Z_{22}} \end{bmatrix} \begin{Bmatrix} \mathbf{v_i} \\ \mathbf{v_1} \end{Bmatrix} \tag{4.15}$$

To obtain the impedance matrix, BEM analyses are conducted on substructure 1 for a number of different velocity boundary conditions. For example, to obtain the first column of the impedance matrix, v=1 is applied to the first element at the inlet of substructure 1, and v=0 is applied elsewhere. The sound pressure solutions at the inlet and outlet will become the first column of the impedance matrix. Similarly, by setting v=1 on each element at the inlet and outlet sequentially, the entire impedance matrix can be obtained. The approach is computationally efficient because only one BEM matrix needs to be formed and decomposed at each frequency. The solution corresponding to each velocity boundary condition is obtained by a trivial back substitution.

Similarly, one can create the impedance matrix for substructure 2. The impedance matrix relationship is

$$\begin{Bmatrix} \mathbf{p_2} \\ \mathbf{p_o} \end{Bmatrix} = \begin{bmatrix} \mathbf{Z_{31}} & \mathbf{Z_{32}} \\ \mathbf{Z_{41}} & \mathbf{Z_{42}} \end{bmatrix} \begin{Bmatrix} \mathbf{v_2} \\ \mathbf{v_o} \end{Bmatrix} \tag{4.16}$$

For the acoustic filter element (DPF) that connects the two substructures, a four-pole transfer matrix is used to describe the filter. That is

$$\begin{Bmatrix} \mathbf{p_1} \\ \mathbf{v_1} \end{Bmatrix} = \begin{bmatrix} \mathbf{A} & \mathbf{B} \\ \mathbf{D} & \mathbf{D} \end{bmatrix} \begin{Bmatrix} \mathbf{p_2} \\ \mathbf{v_2} \end{Bmatrix} \tag{4.17}$$

According to the “element-to-element” four-pole connection assumption, the transfer matrix coefficients A, B, C, and D are each diagonal matrices and can be expressed as

$$\mathbf{A} = \begin{bmatrix} T_{11}^{DPF} & & \\ & T_{11}^{DPF} & \\ & & \ddots \\ & & T_{11}^{DPF} \end{bmatrix} \quad \mathbf{B} = \begin{bmatrix} ST_{12}^{DPF} & & \\ & ST_{12}^{DPF} & \\ & & \ddots \\ & & ST_{12}^{DPF} \end{bmatrix}$$

$$\mathbf{C} = \begin{bmatrix} \frac{T_{21}^{DPF}}{S} & & \\ & \frac{T_{21}^{DPF}}{S} & \\ & & \ddots \\ & & \frac{T_{21}^{DPF}}{S} \end{bmatrix} \quad \mathbf{D} = \begin{bmatrix} T_{22}^{DPF} & & \\ & T_{22}^{DPF} & \\ & & \ddots \\ & & T_{22}^{DPF} \end{bmatrix} \tag{4.18}$$

The interface variables (p_1, v_1, p_2, and v_2) from Equations (4.15), (4.16), (4.17), and (4.18) can be eliminated so that p_i and v_i can be directly related to p_o and v_o by

$$\begin{Bmatrix} \mathbf{p_i} \\ \mathbf{p_o} \end{Bmatrix} = \begin{bmatrix} \mathbf{Z_{51}} & \mathbf{Z_{52}} \\ \mathbf{Z_{61}} & \mathbf{Z_{62}} \end{bmatrix} \begin{Bmatrix} \mathbf{v_i} \\ \mathbf{v_o} \end{Bmatrix} \tag{4.19}$$

The result is (Lou, 2003)

$$\mathbf{Z_{51}} = \mathbf{Z_{11}} + \mathbf{Z_{12}} \left[\mathbf{C}\left(\mathbf{Z_{31}}\mathbf{K}^{-1}\mathbf{Z_{21}}\right) + \mathbf{D}\mathbf{K}^{-1}\mathbf{Z_{21}} \right] \tag{4.20}$$

$$\mathbf{Z_{52}} = \mathbf{Z_{12}}\mathbf{C}\left[\mathbf{Z_{32}} - \mathbf{Z_{31}}\mathbf{K}^{-1}\left(\mathbf{A} - \mathbf{Z_{22}}\mathbf{C}\right)\mathbf{Z_{32}}\right] - \mathbf{Z_{12}}\mathbf{D}\left[\mathbf{K}^{-1}\left(\mathbf{A} - \mathbf{Z_{22}}\mathbf{C}\right)\mathbf{Z_{32}}\right] \tag{4.21}$$

$$\mathbf{Z_{61}} = \mathbf{Z_{41}}\mathbf{K}^{-1}\mathbf{Z_{21}} \tag{4.22}$$

$$\mathbf{Z_{62}} = \mathbf{Z_{42}} - \mathbf{Z_{41}}\mathbf{K}^{-1}\left(\mathbf{A} - \mathbf{Z_{22}}\mathbf{C}\right)\mathbf{Z_{32}} \tag{4.23}$$

where

$$\mathbf{K} = \left[\left(\mathbf{A} - \mathbf{Z}_{22}\mathbf{C}\right)\mathbf{Z}_{31} + \left(\mathbf{B} - \mathbf{Z}_{22}\mathbf{D}\right)\right] \tag{4.24}$$

The cross-sectional area at the inlet and outlet to the system is normally small. Accordingly, plane wave propagation can be assumed at these locations since the sound pressure should be uniform along the cross-section. Thus, each of the vectors p_i, v_i, p_o, and v_o can be lumped into one single variable, and the impedance matrix in Equation (4.19) can be further reduced to a 2×2 impedance matrix. The lumped 2×2 impedance matrix can be converted into a four-pole transfer matrix and the transmission loss of the muffler can be evaluated.

4.4.2 Finite Element Simulation

A similar approach using finite element simulation can also be applied as an alternative to using BEM. The primary difference in between the two approaches is that an element-to-element relationship is used to define the DPF using BEM whereas an element face-to-face relationship is adopted using FEM. The FEM model is shown in Figure 4.8. The model simulates the exhaust system including the DPF unit. However, it is not necessary to mesh the DPF itself. Instead, a transfer relationship is defined in between the two sides of the DPF. The transfer relationship used in FEM is defined as

$$\begin{Bmatrix} v_{n1} \\ v_{n2} \end{Bmatrix} = \begin{bmatrix} \dfrac{T_{22}^{DPF}}{T_{12}^{DPF} S_{IN}} & \dfrac{T_{21}^{DPF}}{S_{IN}} - \dfrac{T_{11}^{DPF} T_{22}^{DPF}}{T_{12}^{DPF} S_{IN}} \\ -\dfrac{1}{T_{12}^{DPF} S_{IN}} & \dfrac{T_{11}^{DPF}}{T_{12}^{DPF} S_{IN}} \end{bmatrix} \begin{Bmatrix} P_1 \\ P_2 \end{Bmatrix} \tag{4.25}$$

The four-pole parameters for the DPF can be determined using the aforementioned Allam and Åbom (Allam, 2005 and Allam, 2006) model. Once again, plane wave behavior is assumed in the DPF itself while three-dimensional wave behavior is fully simulated in the inlet and outlet ducts.

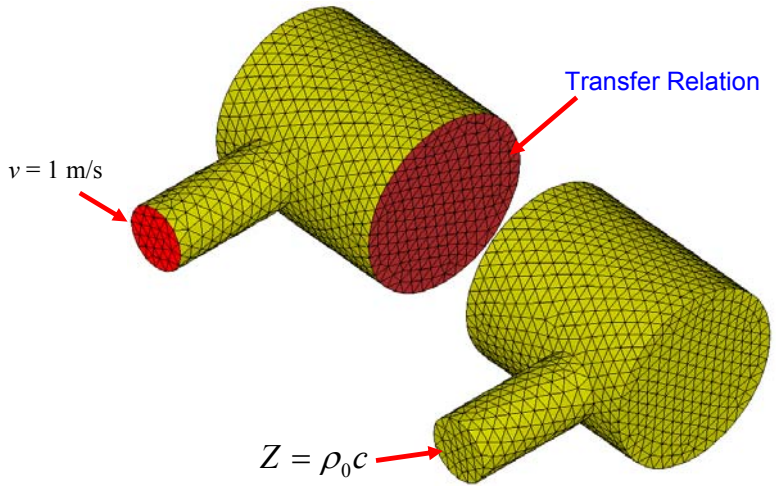

Figure 4.8 FEM model for an exhaust system with a DPF.

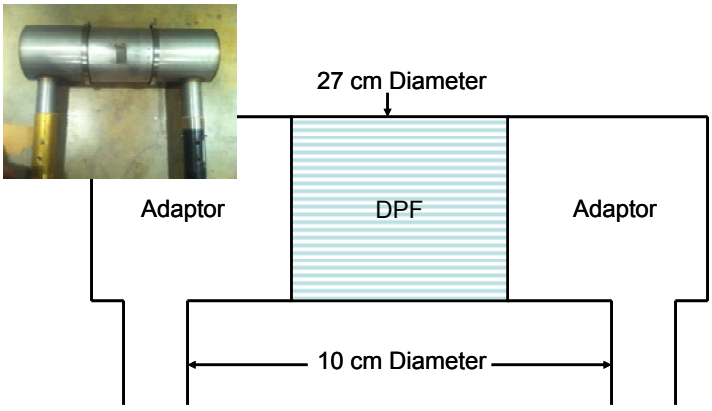

Figure 4.9 Photograph and schematic of experiment.

4.5 Validation on a DPF System

The system shown in Figure 4.9 was modeled using both FEM and BEM. The DPF unit used is identified as Filter 2 in Table 4-1. The inlet and outlet tubes were each 10 cm in diameter and the DPF and adapters were 28 cm in diameter. The plane wave cut-off frequency in the adaptor sections was approximately 660 Hz whereas it is 1840 Hz in the inlet and outlet tubes.

The transmission loss of the system is measured using the two-load method with random-excitation based on ASTM E2611-09 (Lung, 1983, ASTM, 2009 and Tao,

2003). The impedance tubes used are 0.1 m in diameter so there is no area change with respect to the inlet and outlet to the system. The length of the upstream and downstream tubes is 1.0 m and 0.3 m respectively. A two-channel data acquisition system was used and the sound pressure at the microphone closest to the source was used as a reference. The loudspeaker used was capable of producing sufficient acoustic power above 50 Hz. The two loads selected were an open termination and a closed tube with 5.1 cm absorptive material (sound absorbing foam) inserted at the end of the tube. The transmission loss was measured in hemi-anechoic chamber to mitigate any environmental noise contamination for the open termination.

Three different system configurations were considered as follows

Case 1 - The inlet and outlet pipes were oriented at 0° with respect to one another as shown in Figure 4.9.

Case 2 - The inlet and outlet pipes were oriented at 180° with respect to one another.

Case 3 - The inlet and outlet pipes were oriented at 90° with respect to one another.

Figure 4.10, Figure 4.11 and Figure 4.12 compare FEM and BEM simulation to measurement for all three cases. Additionally, the results using plane wave theory (SIDLAB) are shown. Both plane wave theory and the simulation compare well with measurement up to the plane wave cut-off frequency. The results indicate that plane wave theory can be used successfully even when pipes intersect at 90-degree angles. However, plane wave theory differs significantly from the measurement above 660 Hz.

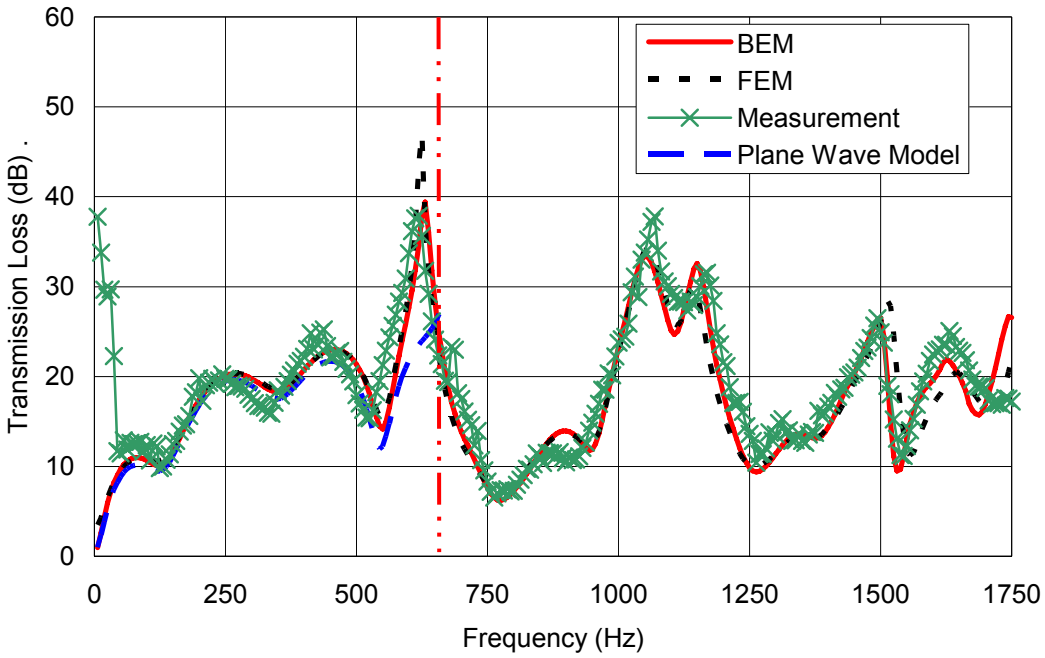

Figure 4.10 Transmission loss comparison between BEM, FEM, plane wave model, and measurement for system shown in Figure 4.9. The angle between inlet and outlet pipes is 0°.

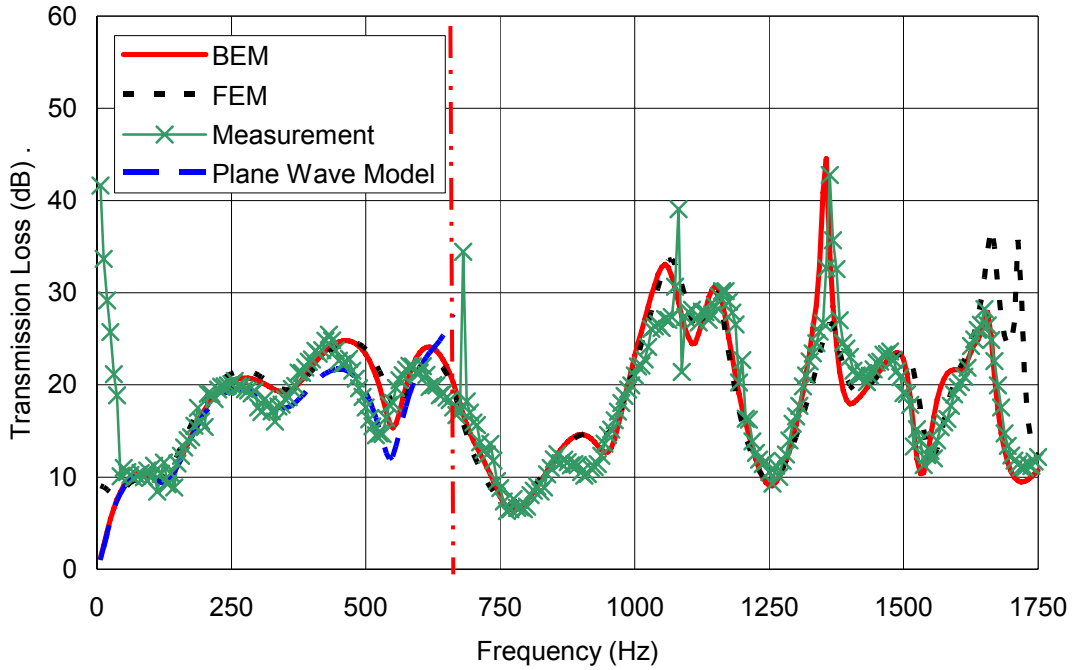

Figure 4.11 Transmission loss comparison between BEM, FEM, plane wave model, and measurement for system shown in Figure 4.9. The angle between inlet and outlet pipes is 180°.

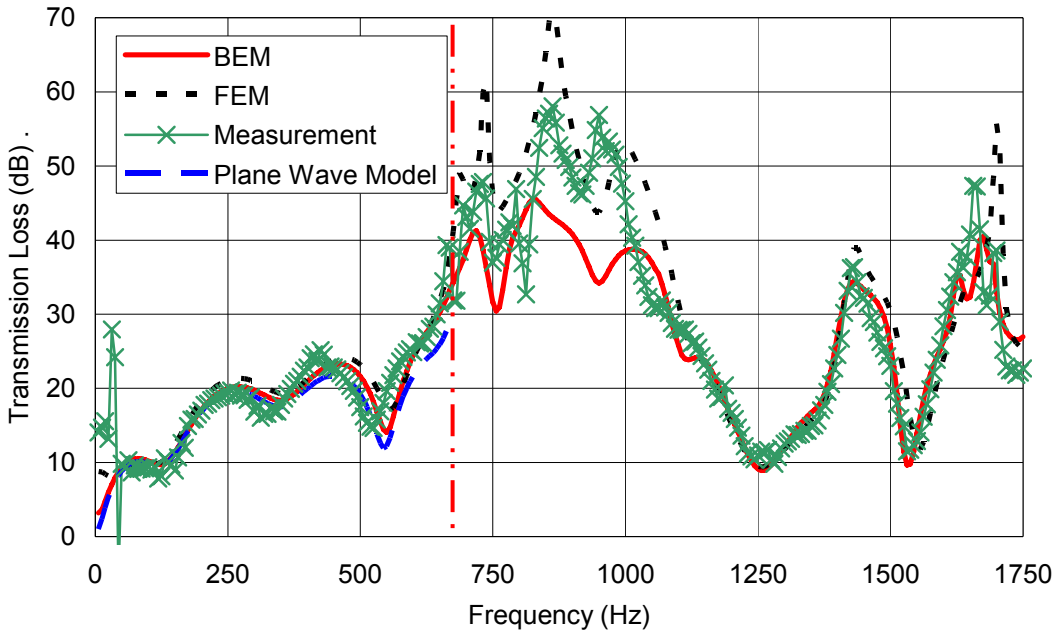

Figure 4.12 Transmission loss comparison between BEM, FEM, plane wave model, and measurement for system shown in Figure 4.9. The angle between inlet and outlet pipes is 90°.

Figure 4.13 and Figure 4.14 show contour plots of the sound pressure at frequencies above the plane wave cut-off frequency. The contour plots clearly indicate three-dimensional behavior in both the inlet and outlet duct systems.

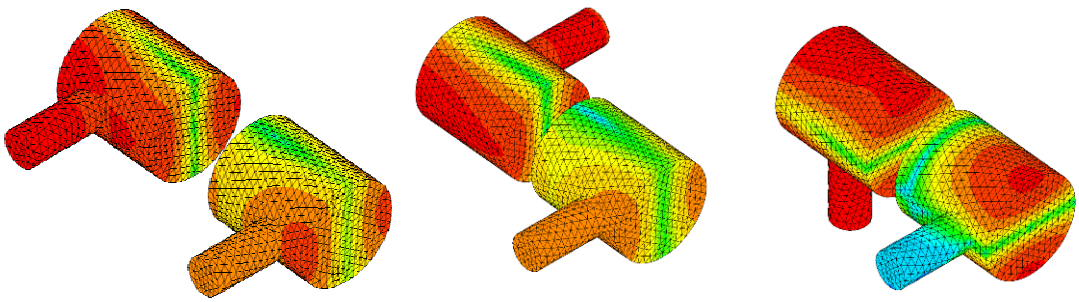

Figure 4.13 Contour plots showing FEM sound pressure contours above plane wave cut-off frequency (800 Hz).

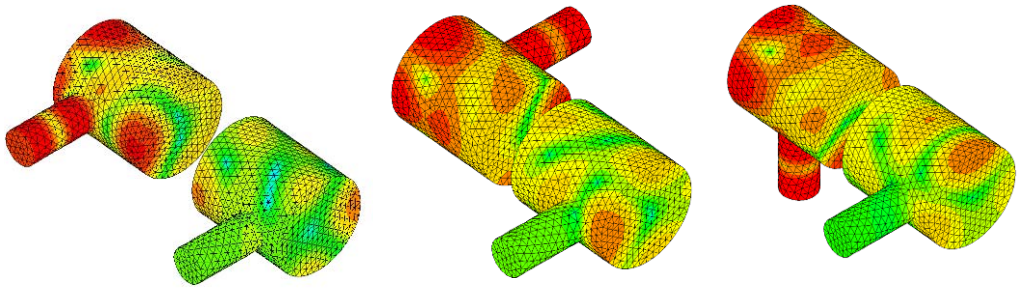

Figure 4.14 Contour plots showing FEM sound pressure contours above plane wave cut-off frequency (1400 Hz).

FEM and BEM simulation compare favorably with measurement beyond the cutoff frequency demonstrating the viability of the suggested approach. Notice that differences between both analysis approaches and measurement is small for transmission losses below 30 dB. Discrepancies for high transmission loss are not surprising considering that the difference between incident and transmitted powers is in excess of three orders of magnitude.

Figure 4.10, Figure 4.11 and Figure 4.12 show that the orientation of the outlet duct with respect to the inlet can greatly influence the transmission loss above the plane wave cutoff frequency. The results suggest that this may be an important design consideration.

4.6 Simulation of DPF using Bulk-Reacting Property

Another method to simulate a DPF system is to model the entire DPF as a bulk material. In other words, the DPF is treated as a sound absorptive material with effective complex density (ρ') and speed of sound (c'). The complex air density and the speed of sound can be calculated from the simulated transfer matrix of the DPF (T_{DPF}) using the equations,

$$c' = \frac{k'}{2\pi f} \tag{4.26}$$

$$\rho' = \frac{Z_c'}{c'} \tag{4.27}$$

where k' is the complex wave number, Z_c' is the characteristic impedance of the DPF bulk, which can be obtained using (Song, 2000)

$$k' = \frac{1}{L}\sin^{-1}\left(\sqrt{-T_{12}^{DPF}T_{21}^{DPF}}\right) \tag{4.28}$$

$$Z_c' = S\sqrt{\frac{T_{12}^{DPF}}{T_{21}^{DPF}}} \tag{4.29}$$

where L and S are the length and the cross-sectional area of the DPF respectively.

Two-cavity measurement (Utsuno, 1989) can also provide the complex air density and the speed of sound. The disadvantage is that the measured results are only valid below the frequency cut-off, which is determined by the diameter of the DPF.

The calculated normalized characteristic impedance and complex wave number of the DPF Filter 2 are shown in Figure 4.15 and Figure 4.16, respectively. The complex air density and speed of sound are shown in Figure 4.17 and Figure 4.18, respectively.

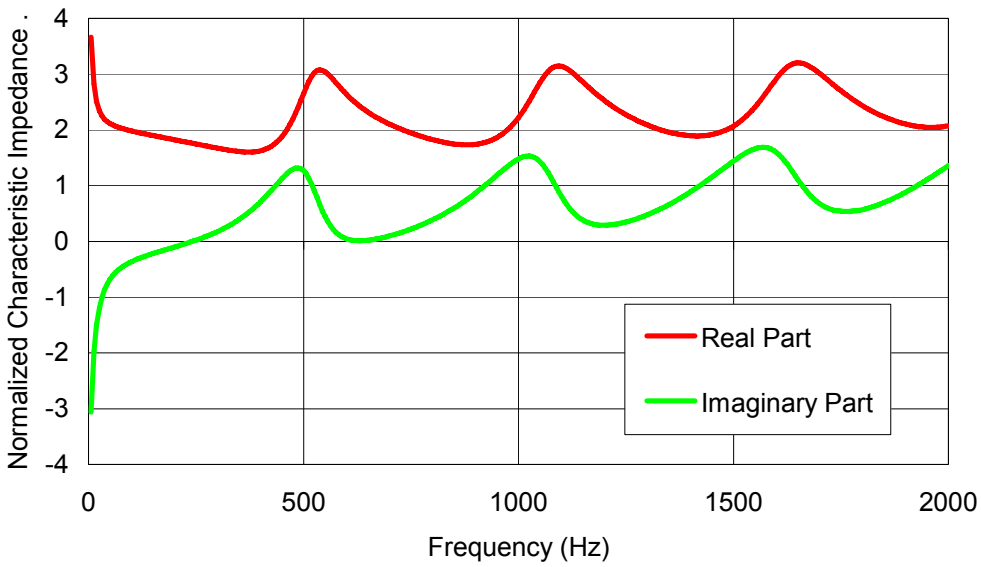

Figure 4.15 Normalized characteristic impedance of DPF.

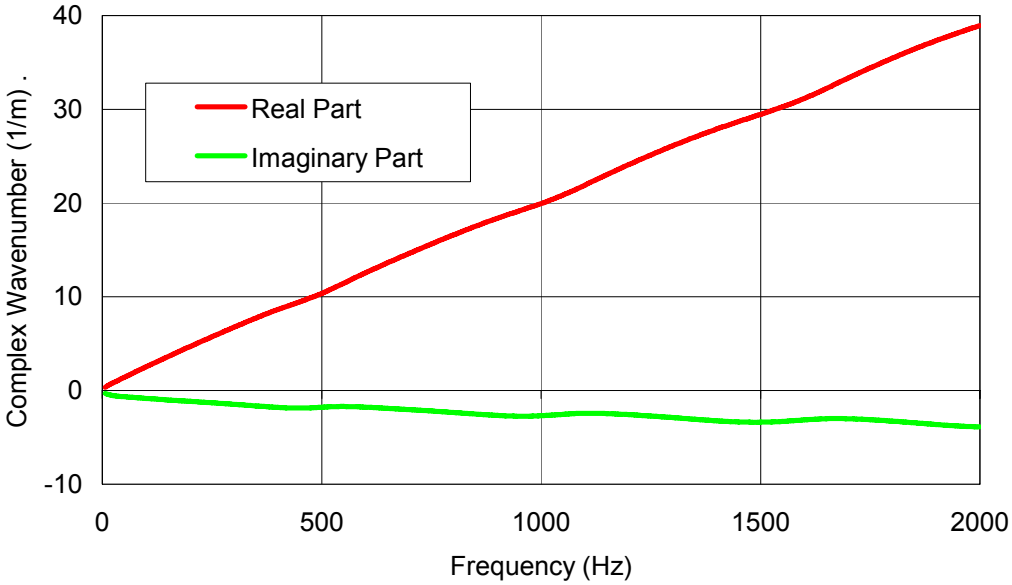

Figure 4.16 Complex wavenumber of DPF.

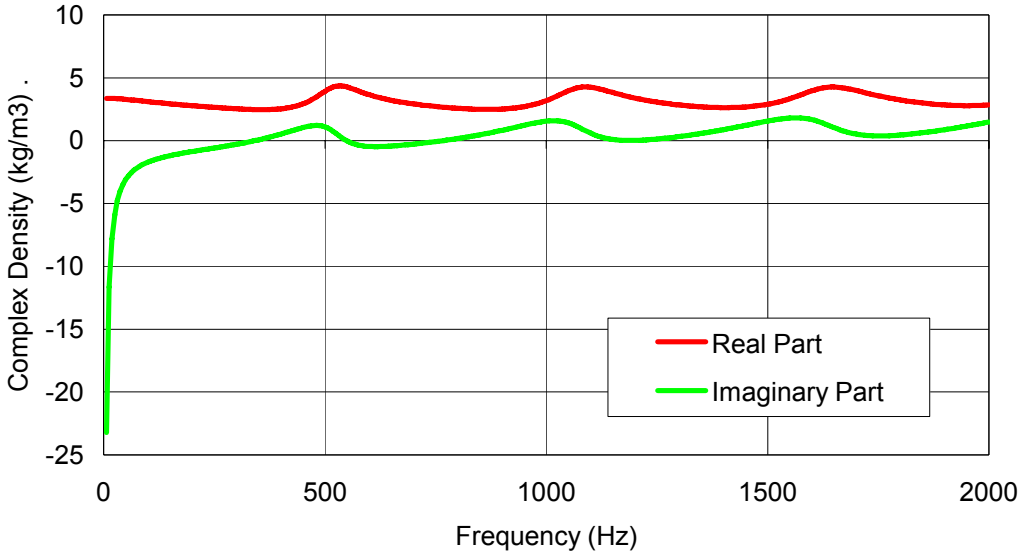

Figure 4.17 Complex density of DPF.

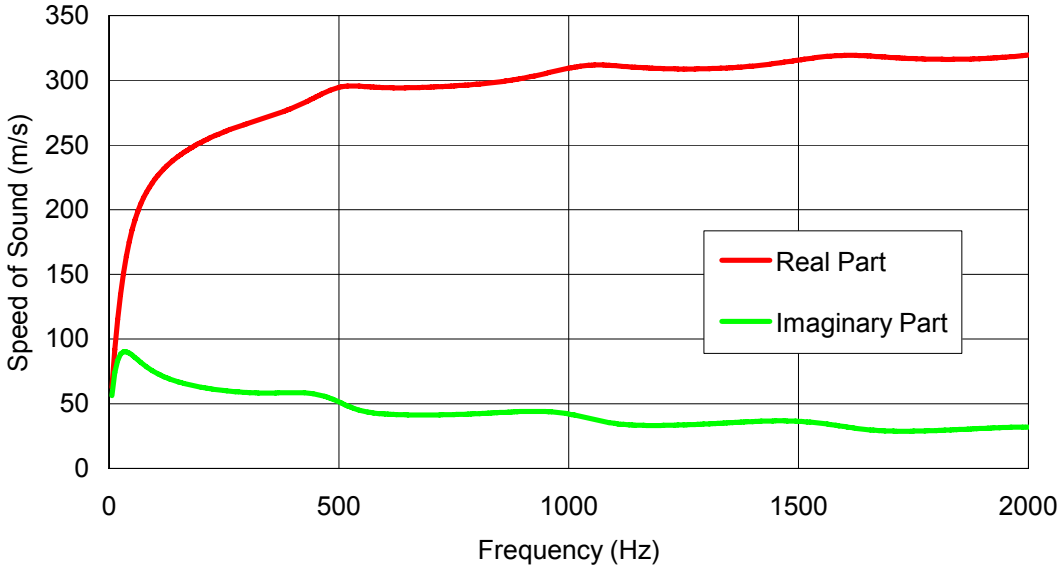

Figure 4.18 Complex speed of sound of DPF.

By using the bulk property to model the DPF system, the adapters as well as the DPF are discretized. The fluid properties applied in the adapters are the air

properties. However, the fluid properties in the DPF should be the calculated complex speed of sound and complex air density.

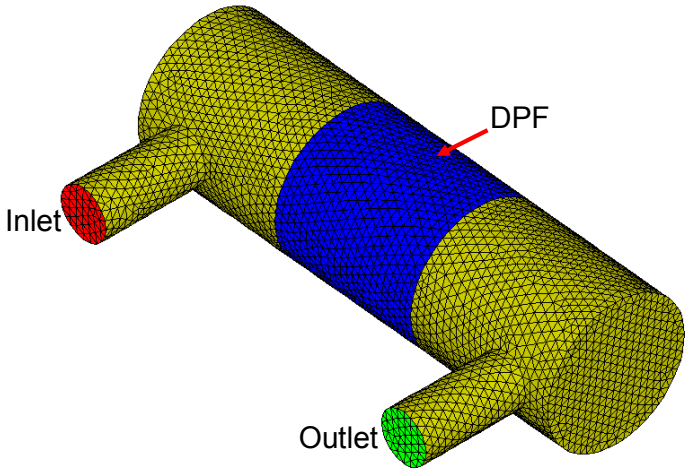

Figure 4.19 BEM model for DPF bulk.

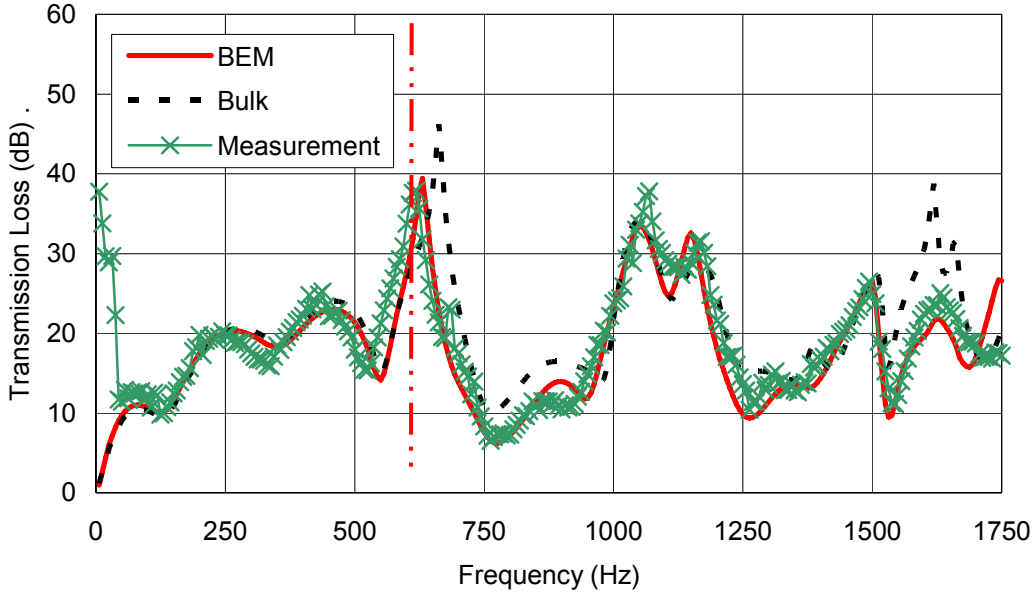

Figure 4.20 Transmission loss comparison between BEM, Bulk, and measurement. The angle between inlet and outlet pipes is 0°.

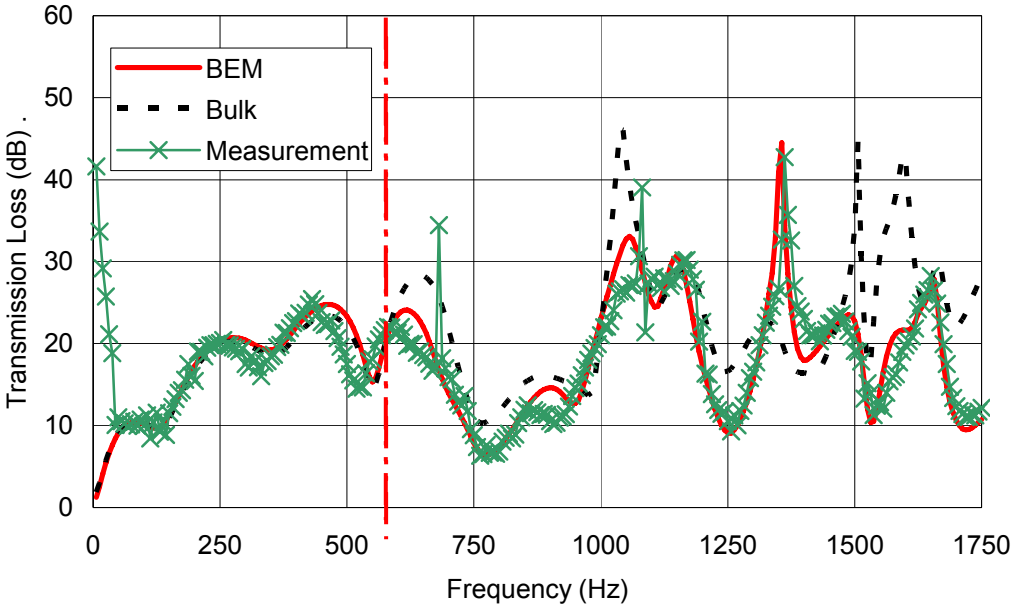

Figure 4.21 Transmission loss comparison between BEM, Bulk, and measurement. The angle between inlet and outlet pipes is 180°.

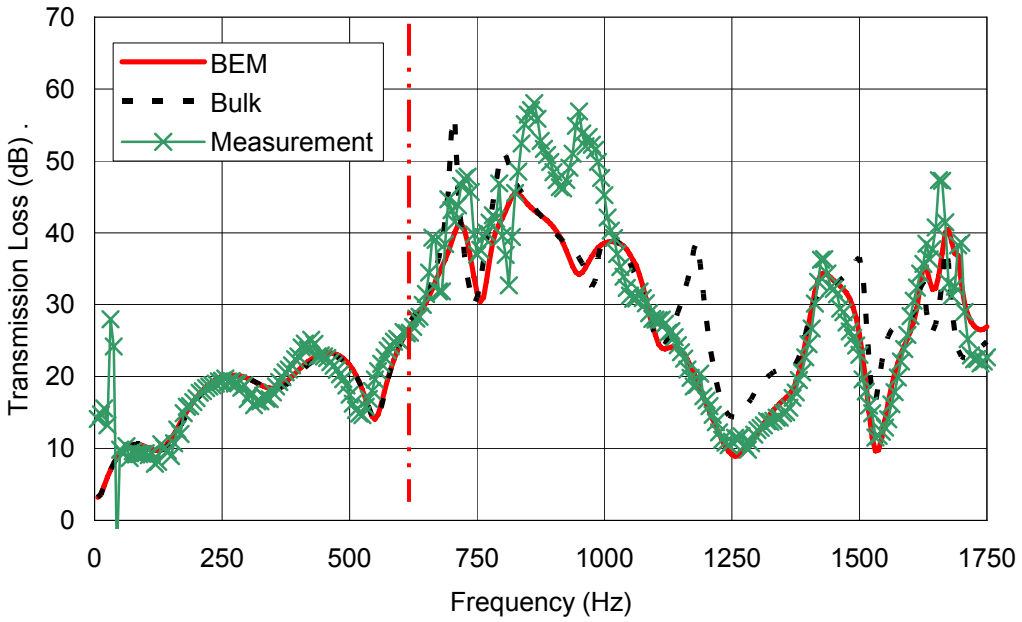

Figure 4.22 Transmission loss comparison between BEM, Bulk, and measurement. The angle between inlet and outlet pipes is 90°.

Figure 4.20, Figure 4.21, and Figure 4.22 compare the bulk material model with the original BEM model and measured results for the three cases. The bulk model results agree well with other two results at low frequencies (below the cutoff). At high frequencies, the discrepancies between the bulk material model results and the measured results are more apparent. This is likely due to the fact that a bulk material model assumes that the DPF is isotropic when it is, in fact, transverse isotropic. However, results are still reasonable, even at high frequencies, using the bulk material assumption and this modeling strategy may be preferred because of modeling ease.

4.7 Summary

It was validated that plane wave propagation can be assumed in a DPF unit. However, three-dimensional effects may be important on both sides of the DPF unit. A process has been documented for determining the transmission loss of DPF filters in exhaust systems above the plane wave cut-off frequency. The model developed by Allam and Åbom is used to determine the transfer matrix for the DPF channels.

This transfer matrix is then used in a BEM or FEM model to determine the transmission loss at frequencies above the plane wave cutoff. The developed models were experimentally validated and the results demonstrate that the approach can be used to analyze complicated multi-component muffler systems consisting of DPF filters.

Furthermore, the results indicated that the orientation of the inlet and outlet ducts can have a significant effect on the transmission loss. This fact was validated both in the model and also experimentally. This suggests that the orientation and shape of the inlet and outlet ducts could be an important design consideration above the plane wave cutoff frequency.

Chapter 5 SIMULATION OF SOURCE IMPEDANCE

5.1 The Relation between Acoustical Source Impedance and Electrical Source Impedance

Acoustical source impedance is essential to determining the insertion loss of muffler and piping systems (Prasad, 1981). The concept of acoustical source impedance, as well as the acoustical source strength, originated from the electrical analogy. Sound pressure and particle velocity are analogous to voltage and current in electrical systems respectively. If the sound source is an ideal pressure source (p_s), which is akin to a voltage source in electrical systems, the source impedance (z_s) is a series impedance as shown in Figure 5.1. The relation between the source and the load can be expressed as

$$\frac{p_s}{z_s + z_L} = \frac{p_L}{z_L} \tag{5.1}$$

where p_L and z_L are the load pressure and impedance respectively. It follows that, the source impedance can be written as

$$z_s = \frac{p_s - p_L}{u_L} \tag{5.2}$$

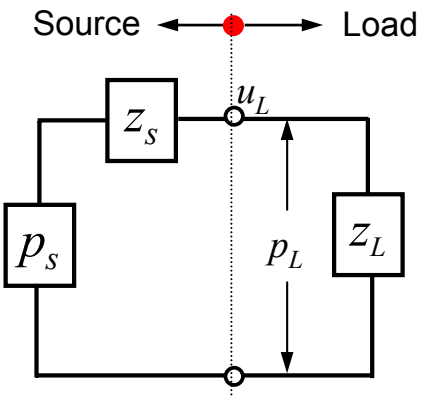

Figure 5.1 Schematic of series source impedance.

If the sound source is an ideal particle velocity source (u_s), (which is akin to an ideal current source in an electrical system), the source impedance is a parallel impedance as shown in Figure 5.2. In a parallel acoustical system, the relation between the source and the load can be expressed as

$$u_L z_L = u_s \frac{z_s z_L}{z_s + z_L} \tag{5.3}$$

and the source impedance can be written as

$$z_s = \frac{p_L}{u_s - u_L} \tag{5.4}$$

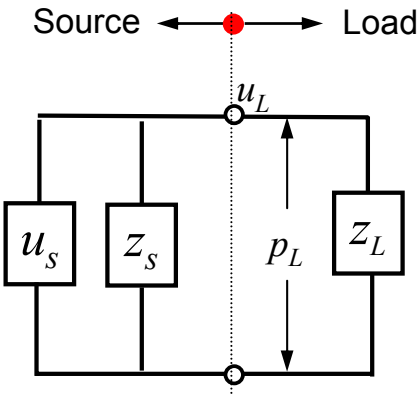

Figure 5.2 Schematic of parallel source impedance.

5.2 Review of Source Impedance Measurement and Modeling

5.2.1 Direct Method

Several approaches to determine source impedance experimentally are based on the circuit analogy. These approaches can be characterized as direct and indirect methods. By applying a secondary source, which is at least 20 dB louder,

the tested source is able to be measured as a passive acoustical element. Both the standing wave (Galaitsis and Bender 1975, Ross and Crocker, 1983) and two-microphone method (Seybert and Ross, 1977, Prasad and Crocker, 1983) are applicable, which are shown in Figure 5.3. The primary inconvenience of direct methods is that a more powerful external source is difficult, if not impossible to acquire, especially when measuring sources like engines with powerful source strength at low frequencies.

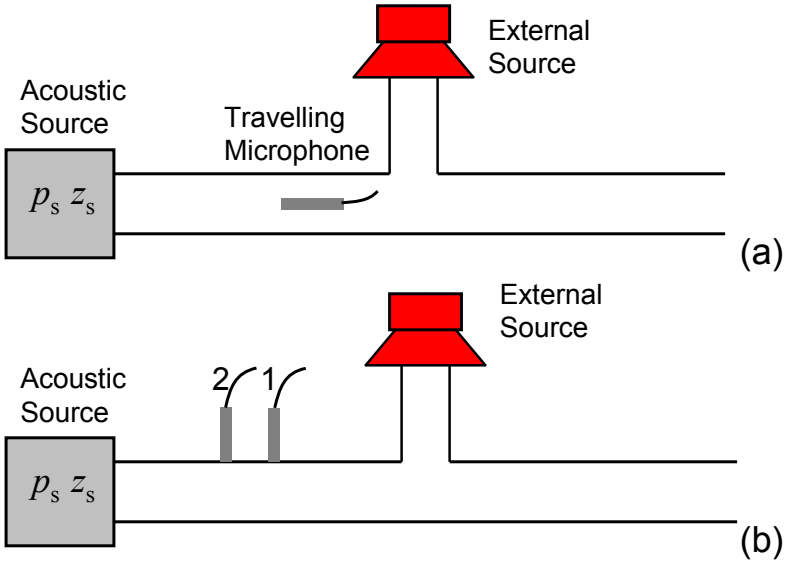

Figure 5.3 Direct methods to measure source impedance: (a) standing wave method, (b) two-microphone method.

5.2.2 Indirect Method

Indirect methods are usually preferred because a powerful external source is not required and the source impedance as well as source strength is able to be measured simultaneously. The most commonly used indirect method is the two-load method (Kathuriya and Munjal, 1979, Egolf and Leonard, 1977). A schematic showing the process is shown in Figure 5.4. The measured source strength and source impedance can be obtained using

$$z_s = \frac{z_{L1} z_{L2} \left(p_{L1} - p_{L2} \right)}{z_{L1} p_{L2} - z_{L2} p_{L1}} \tag{5.5}$$

$$p_s = \frac{p_{L1} p_{L2} \left(z_{L1} - z_{L2} \right)}{z_{L1} p_{L2} - z_{L2} p_{L1}} \tag{5.6}$$

where p_{L1} and p_{L2} are the measured load pressures. z_{L1} and z_{L2} are the measured load impedances. For measuring an exhaust or intake system with flow, two different loads are produced by varying the length of the pipe or adding a side branch. The errors due to the linear dependency of the two loads were investigated (Bodén, 1988). In order to minimize the errors due to the load selections, additional loads are sometimes measured. Then, least squares methods can be used to solve the over-determined problem (Bodén, 1991 and Bodén, 1992).

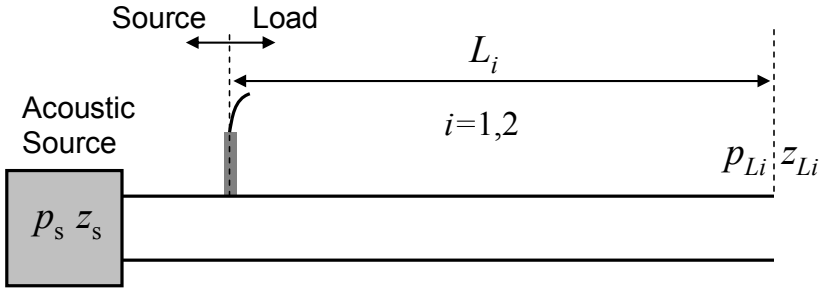

Figure 5.4 Two-load method to measure source impedance.

The methods discussed above all require a consistent phase reference which should not vary as the acoustic load is varied. Normally, an accelerometer is placed on the engine and used as a reference. Alternative methods such as the three-load (Alves, 1986, Alves, 1987) and four-load (Prasad, 1987, Desmons, 1994) methods have been proposed. Both methods are based on absolute quantities and avoid the need to select a reference. The errors for four-load method have been investigated by several researchers (Sridhara and Croker,

1992, Bodén, 1995). The measured source resistance is sometimes negative at some frequencies using an indirect method. At some frequencies, the source impedance can be negative since the method used is an indirect method and assumes a time-invariant linear source which is not always the case (Ih and Peat, 2002).

In lieu of using the circuit analogy, a wave decomposition method can also be applied to measure source impedance (Bodén and Åbom, 1995, Liu and Herrin, 2009). The outgoing wave from the source (p_{s+}) is determined instead of the source strength (p_s) as shown in Figure 5.5.

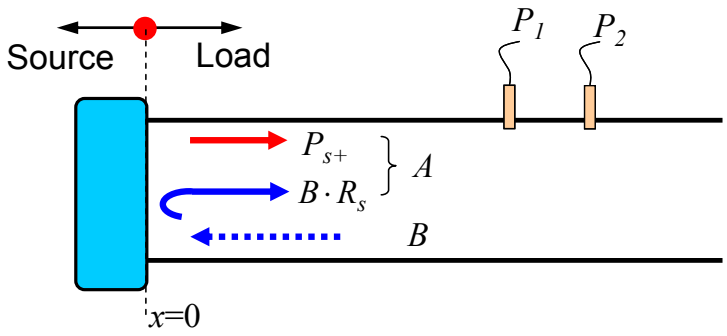

Figure 5.5 Schematic of the wave decomposition method to measure source impedance (Liu and Herrin, 2009).

In order to solve the two unknowns, p_{s+} and R_s, at least two loads are required. By measuring the sound pressures at two different locations and applying wave decomposition for each load, the incident and reflected wave strengths (A and B) are obtained. Liu and Herrin (2009) then noted that

$$R_s = \frac{A_1 - A_2}{B_1 - B_2} \tag{5.7}$$

and

$$p_{s+} = \frac{B_1 A_2 - B_2 A_1}{B_1 - B_2} \tag{5.8}$$

The source impedance and source strength can be obtained respectively by

$$z_s = \frac{1 + R_s}{1 - R_s} \tag{5.9}$$

and

$$p_s = (1 + z_s) p_{s+} \tag{5.10}$$

5.2.3 Source Impedance Modeling

In the engine intake and exhaust industries, it is very helpful to investigate the source properties of the engine in the design stage. A great deal of research has focused on determining the source impedance via modeling. One-dimensional CFD codes such as AVL-BOOST, Ricardo-WAVE and GT-Power are used for investigating IC engine thermodynamics. These solvers provide unsteady pressures and flow velocities, which are utilized to examine the source properties. Knutsson and Bodén (Knutsson, 2012) extracted the source strength and impedance using Ricardo-WAVE, a commercial 1-D CFD simulation code. They solved the 1-D compressible gas dynamics equations for mass, energy and momentum by using the finite volume approach. Bodén and Fairbrother (Bodén, 2004 and Fairbrother, 2005) extracted the source strength and impedance from non-linear finite volume CFD simulation using the two-load method. Then, Munjal and Hota (2010) used the finite volume CFD code AVL-BOOST to simulate the pressure-time history. The source strength and impedance were determined using the two-load method.

Though the source properties determined from 1-D CFD are suspect, the approach is valuable because measurement of source impedance is difficult and expensive. The source impedance determined in this manner can then be used in plane wave or deterministic models.

5.3 Applied Source Impedance to Finite Element Simulation

5.3.1 Basic Modeling Concepts

Transmission loss and insertion loss are the two most important metrics used to evaluate the performance of muffler (or silencer) systems. Transmission loss is defined as the difference between the power incident on the muffler and transmitted from the muffler. It is a property of the muffler itself and can be determined by knowing the transfer or four-pole matrix of the muffler.

Insertion loss is defined as the difference between the sound pressure levels at the tailpipe with and without the muffler. It is representative of the sound attenuation performance of the entire system. Besides the transfer matrix of the muffler, source and termination impedance are also required to determine the insertion loss. Moreover, if the sound pressure at the outlet of the tailpipe is of concern, the source strength is also required.

For finite or boundary element modeling, source impedance has not ordinarily been simulated in the past. In order to apply appropriate boundary conditions, the modeling technique shown in Figure 5.6 can be applied. The basic concept is that a pseudo extended duct is modeled having a short length compared to an acoustic wavelength. The source strength is modeled as a pressure boundary condition at the left end of the pseudo duct. By doing that, it is assumed that the sound pressure at the two ends of the pseudo ducts are close enough so that the pressure condition applied is constant across the length. At lower frequencies, this assumption should be appropriate. The boundary condition is modeled as a transfer relationship between the pseudo duct and the real end of the system, indicated as the "1st Face" and "2nd Face" in Figure 5.6. The technique to model source impedance is the same as modeling transfer impedance for micro-

perforated panels and diesel particulate filter membranes. The commercial software LMS SYSNOISE was used for all analyses.

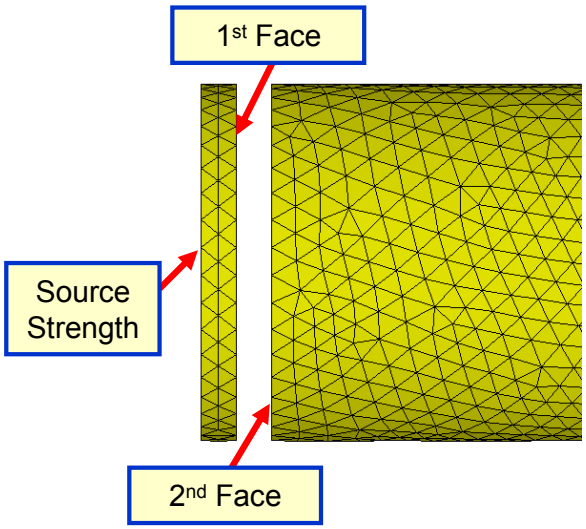

Figure 5.6 Finite element model for source strength and source impedance.

The transfer relationship can be calculated by

$$\begin{bmatrix} v_{n1} \\ v_{n2} \end{bmatrix} = \begin{bmatrix} \beta & -\beta \\ -\beta & \beta \end{bmatrix} \begin{bmatrix} P_1 \\ P_2 \end{bmatrix} + \begin{bmatrix} \alpha_3 \\ \alpha_6 \end{bmatrix} \tag{5.11}$$

where v_{n1}, v_{n2} and P_1, P_2 are the particle velocities and sound pressures at the faces. β is the transfer admittance, which is the reciprocal of the source impedance. Thus,

$$\beta = \frac{1}{z_s} \tag{5.12}$$

α_3 and α_6 are both zero.

5.3.2 Validation of the Numerical Model

In order to validate the finite element model, a straight pipe is modeled as shown in Figure 5.7. The lengths of the duct and pseudo duct are 1.2 m and 0.005 m respectively.

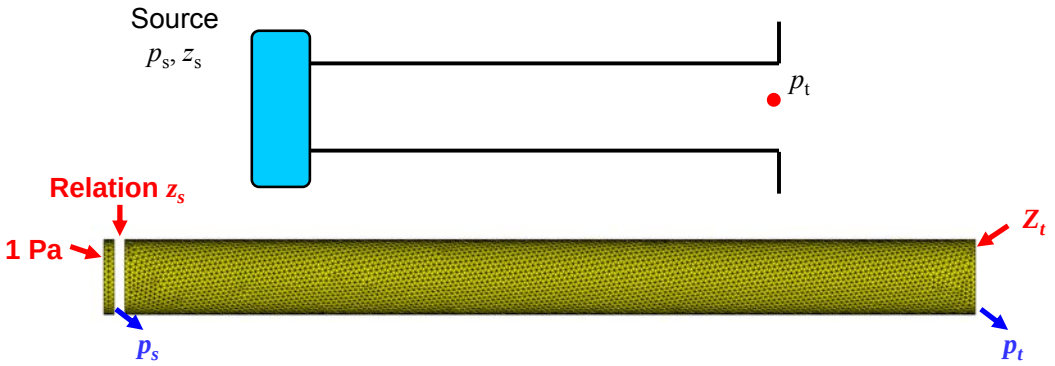

Figure 5.7 Finite element model for a straight duct with source strength, source impedance and termination impedance.

The pressure boundary condition applied to the model is a unit sound pressure. The source impedance applied is that measured for an engine intake system, which is shown in Figure 5.8 (Tao, 2007). Two different termination impedances were applied separately. One is that for an unflanged duct and can be expressed as (Levine and Schwinger, 1948)

$$R_{free} = 1 + 0.01336ka - 0.59079(ka)^2 + 0.33576(ka)^3 - 0.06432(ka)^4 \quad (5.13)$$

when ka<1.5, where k is the wavelength and a is the radius of the downstream tube. The free space termination impedance then can be obtained by

$$z_{free} = \frac{\rho c(1+R)}{1-R} \quad (5.14)$$

The other termination applied is a baffle termination (flanged opening). The baffle termination impedance can be expressed as (Pierce, 1981)

$$z_{baffle} = \rho c\left[R_1(2ka) - iX_1(2ka)\right] \tag{5.15}$$

where

$$R_1 = 1 - \frac{J_1(2ka)}{ka} \tag{5.16}$$

$$X_1 = \frac{H_1(2ka)}{ka} \tag{5.17}$$

where J_1 and H_1 are the Bessel function and the Struve function of first order respectively.

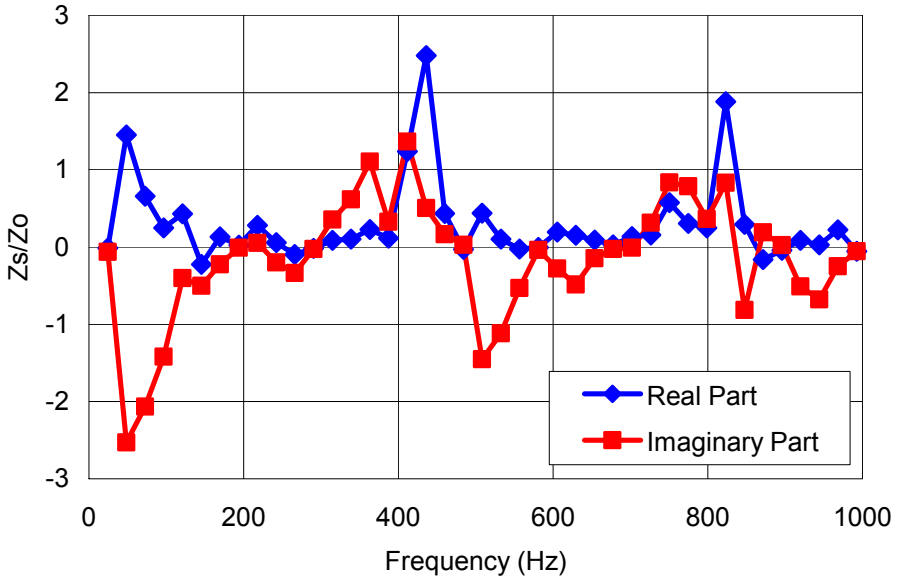

Figure 5.8 Measured source impedance for a real engine intake (Tao, 2007).

The straight duct is also solved using the analytical model. Knowing the source characteristics, length of the tube and the termination impedance, the sound pressure level at the end of the tube can be expressed as (Munjal, 1987)

$$Lp_t = 20\log_{10}\left|\frac{p_s \cdot z_t}{\left(T_{11}\cdot z_t + T_{12} + T_{21}\cdot z_s z_t + T_{22}\cdot z_s\right)\cdot 2\times 10^{-5}}\right| \tag{5.18}$$

where T is the four-pole matrix of the straight tube, which is determined by the tube length. The sound pressure at the opening of the tube is extracted from the finite element model described before and compared with the analytical solution. The results with the free space and baffle termination are shown in Figure 5.9 and Figure 5.10 respectively. Both cases show good agreement between the finite element simulation and the analytical solution.

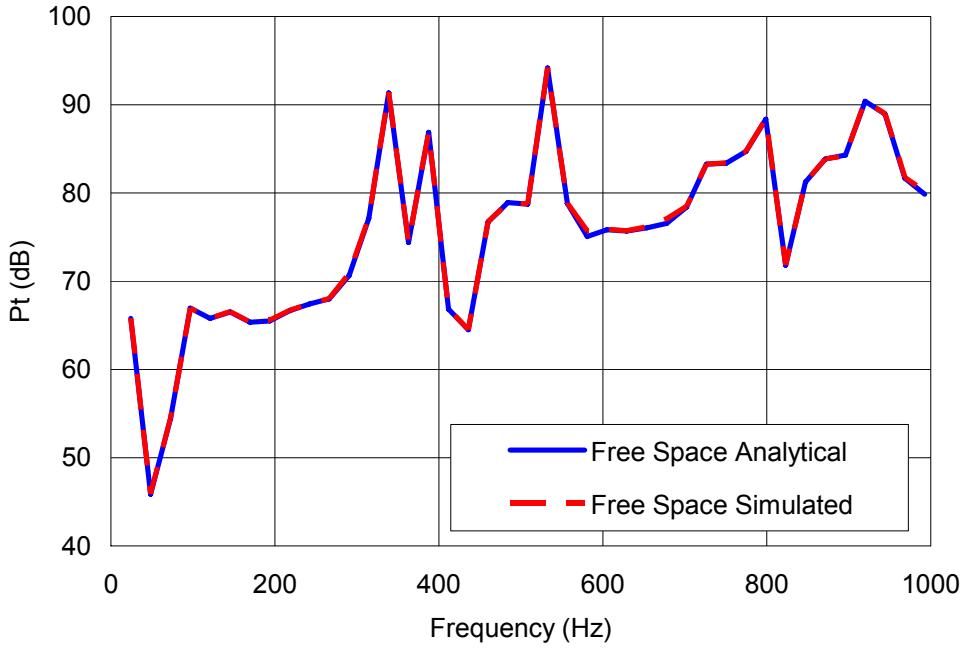

Figure 5.9 Sound pressure level comparison with free space termination between analytical solution and simulated result.

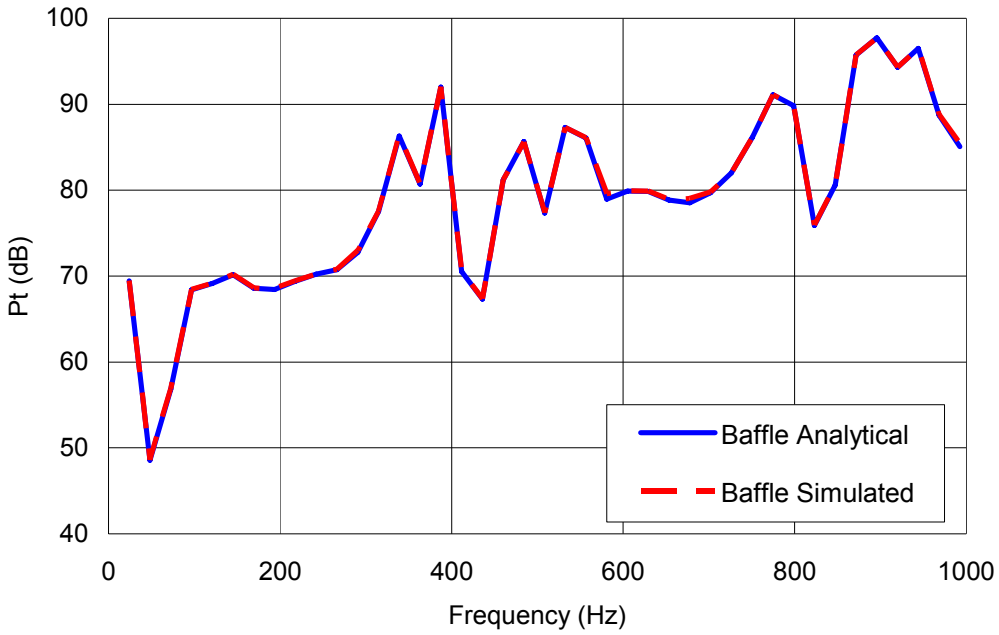

Figure 5.10 Sound pressure level comparison with baffle termination between analytical solution and simulated result.

An alternative method to model the source using the finite element approach takes advantage of using the active term in the transfer relationship. Instead of modeling the source strength as a boundary condition, it can be modeled as an active source in the transfer relationship. Equation (5.11) can be modified as

$$\begin{bmatrix} v_{n1} \\ v_{n2} \end{bmatrix} = \begin{bmatrix} \beta & -\beta \\ -\beta & \beta \end{bmatrix} \begin{bmatrix} P_1 \\ P_2 \end{bmatrix} + \begin{bmatrix} p_s \\ 0 \end{bmatrix} \tag{5.19}$$

An anechoic boundary condition is assumed for the left end surface of the model in Figure 5.6.

5.4 Insertion Loss Modeling using Finite Element Approach

By modeling the acoustic source using the finite element method, the insertion loss of mufflers and silencers is able to be determined numerically. In order to model insertion loss, two complete models are required to be built. One is the

entire system with the muffler, including the source characteristics, inlet duct, muffler, tailpipe, and termination impedance. The other one is a similar model where the muffler is replaced with a straight duct having the same length.

A simple expansion chamber is modeled as a test case as shown in Figure 5.11. The length and diameter of the chamber are 12 inch and 6 inch respectively. The upstream and downstream tube is 24 inch and 12 inch respectively with 2 inch diameter. The source impedance is pre-determined as 0.7-0.7i, which is a recommended constant for engine exhaust systems if the real source impedance is unknown (Munjal and Hota, 2010). A free space termination impedance is applied in this case.

Figure 5.12 illustrates the finite element model. The unit pressure (pseudo source strength) boundary condition and free space termination impedance are applied at the corresponding ends. The transfer relation determined by Equation (5.11) is applied to model the source impedance. After solving the model, the sound pressure level at the end of the downstream tube is extracted. Similarly, a straight duct model having the same boundary conditions was solved. Insertion loss is the difference between the sound pressure level (in dB) at the termination without and with the muffler.

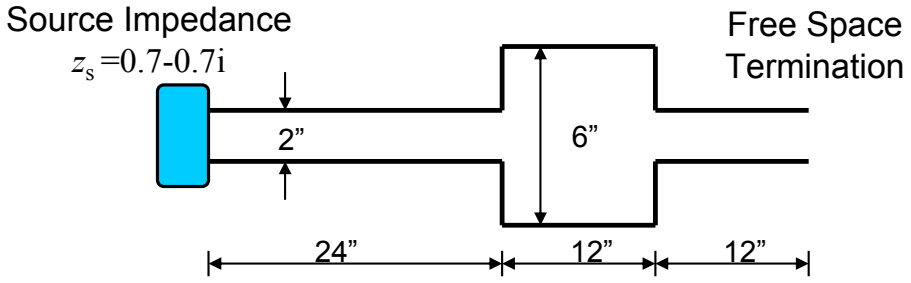

Figure 5.11 Test case for insertion loss modeling.

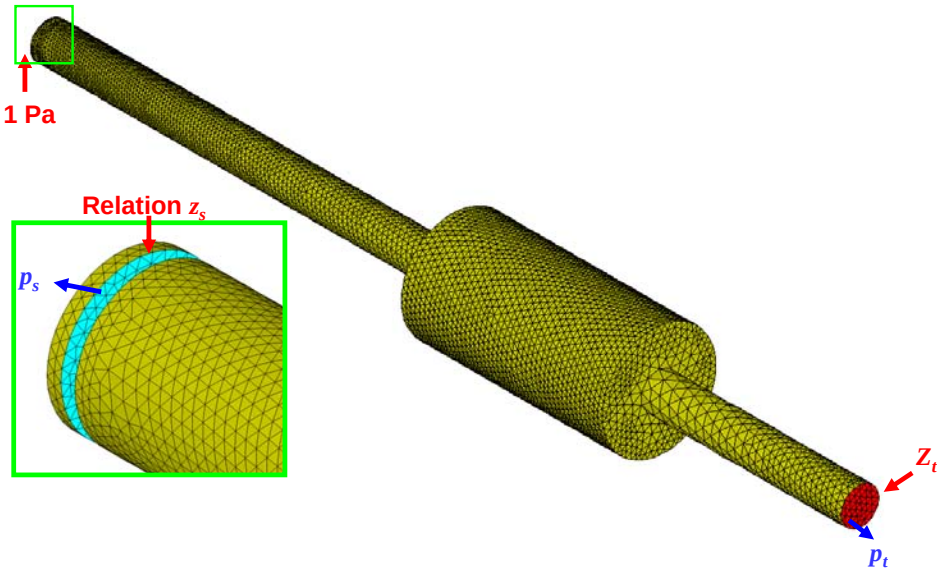

Figure 5.12 Finite element model of the simple expansion chamber.

The insertion loss from the FEM is compared against the analytical model since the transfer matrices for a simple expansion chamber are well known and the insertion loss is easily calculated. The commercial plane wave software SIDLAB was used. The results are compared in Figure 5.13 with a good agreement. The alternative approach to model the source using the active term in the transfer relation is also validated. The results are shown in Figure 5.14.

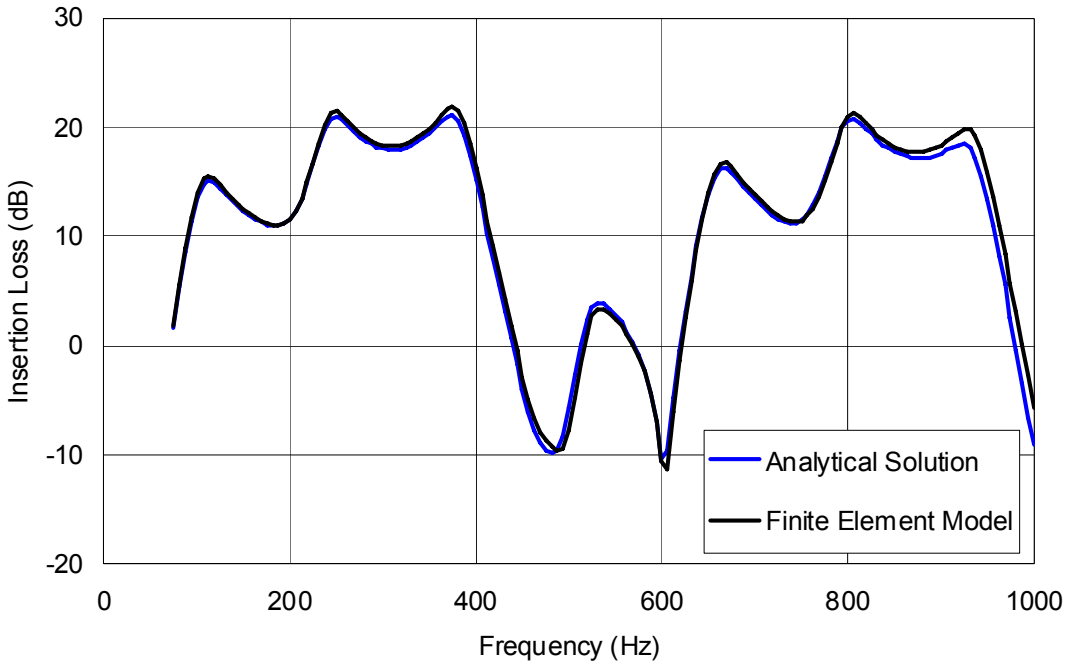

Figure 5.13 Insertion loss comparison between FEM and analytical models.

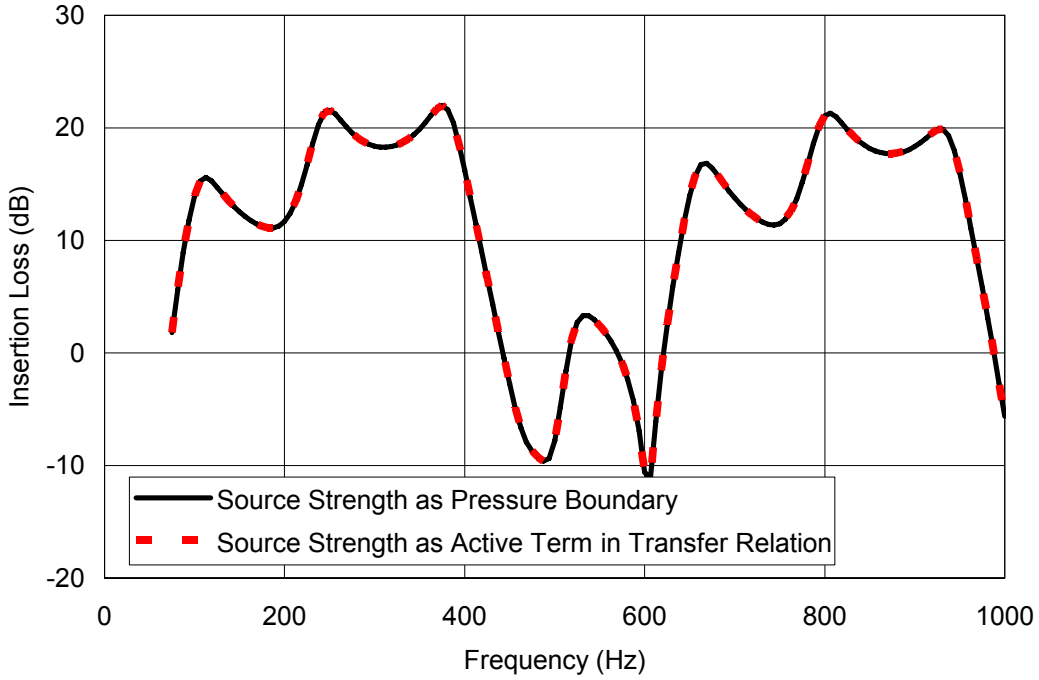

Figure 5.14 Insertion loss comparison between two different source modeling techniques.

Insertion loss can be negative since it takes into account the performance of the muffler installed in the exhaust system (Wallin et al., 2012). Strong resonances can form in the pipes upstream and downstream to the muffler. As indicated in Figure 5.13 and Figure 5.14, the modeled system has two negative insertion loss troughs at frequencies of 464 Hz and 606 Hz. The sound pressure and particle velocity contour plots of the entire system at the two frequencies are shown in Figure 5.15 and Figure 5.16 respectively. As shown in the figures, the reason for the negative insertion loss is that the impedance mismatch of the chamber introduces a strong resonance at the tailpipe for both frequencies.

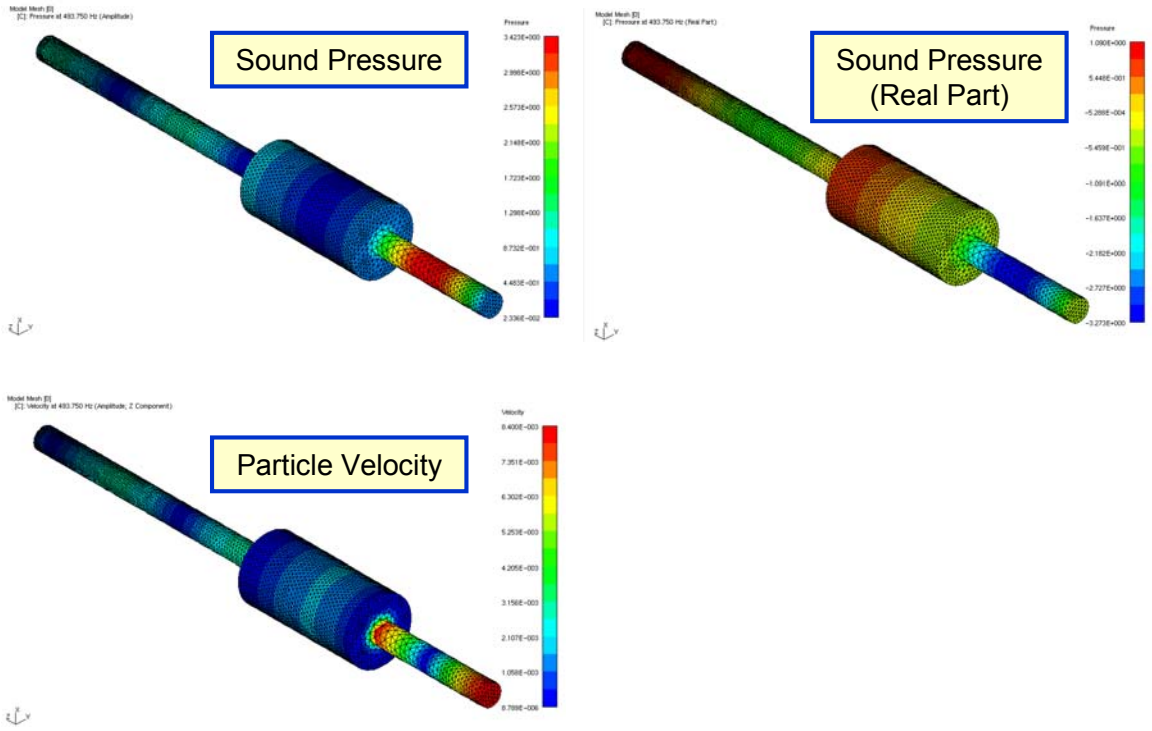

Figure 5.15 Contour plots for the simple expansion system at 464 Hz.

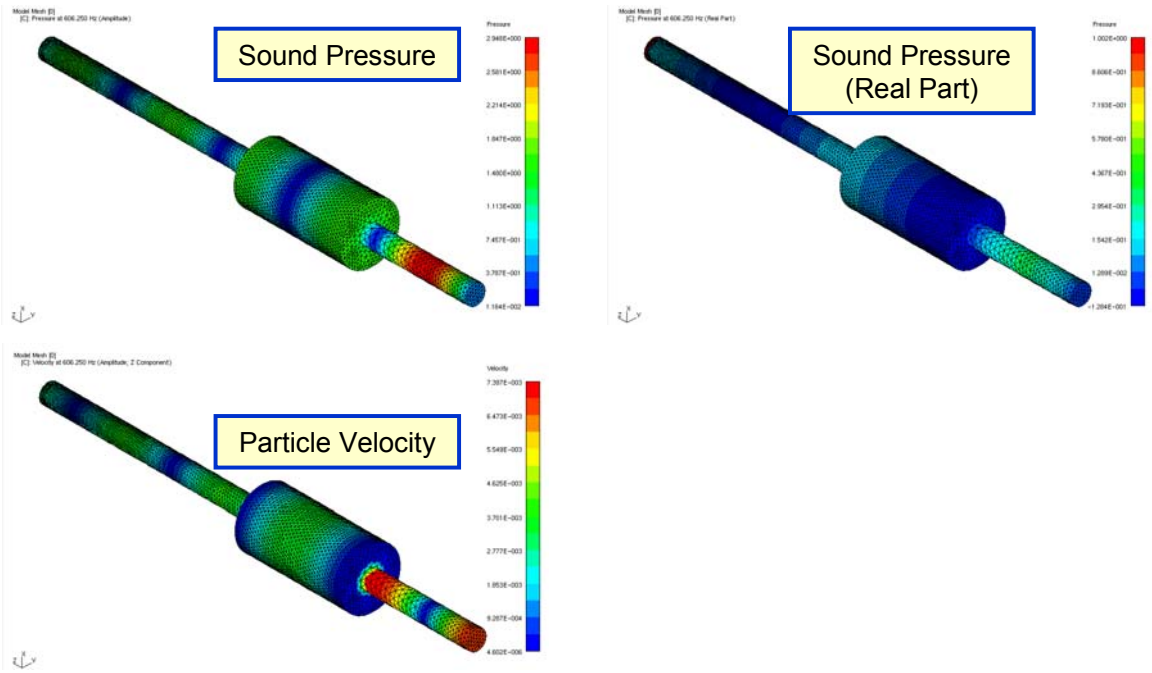

Figure 5.16 Contour plots for the simple expansion system at 606 Hz.

5.5 Summary

In this chapter, the analogy between acoustic and electrical source impedance is reviewed. The acoustic source can be treated as an ideal constant pressure source connected to the source impedance in series. The source impedance is a series impedance and can thus be modeled as a transfer impedance. Based upon that, several popular direct and indirect experimental approaches to measure acoustic source impedance are reviewed. Afterward, a finite element modeling technique is introduced to simulate acoustic sources which takes into account the source impedance. A very short pseudo duct mesh should be built ahead of the duct system. A constant sound pressure boundary condition is applied to the end of the pseudo duct as the source strength. A transfer relation is applied between the pseudo duct and the real system to simulate the series source impedance. The model is validated against analytical results at low frequencies where plane wave behavior is assumed. Alternatively, the source strength can also be modeled as an active term in the transfer relation instead of

as a pressure boundary condition. The entire exhaust system with source and load characteristics is simulated.

Chapter 6 PRACTICAL ASPECTS ON SOUND TRANSMISSION LOSS MEASUREMENT

6.1 Introduction

Insertion loss is the metric typically used to assess muffler performance in the field. It is defined as the difference in sound pressure at a point near the termination with and without a muffler installed. Though insertion loss is easy to measure, it is a property of the source and termination impedances as well as the lengths of the inlet and outlet ducts and the muffler. Hence, insertion loss is a measure of the muffler attenuation installed in a particular exhaust system.

Transmission loss eliminates the effect of the inlet and outlet ducts. Indeed, insertion loss is equal to the transmission loss if the source and termination impedances are both anechoic. Transmission loss is simpler to determine using analysis since an anechoic termination is easily applied as a boundary condition below the plane wave cutoff.

Measurement of transmission loss is trickier. Certainly, transmission loss is often roughly measured using either a very long downstream duct or a makeshift anechoic termination. However, it is difficult to create an anechoic termination that will be accurate over the full frequency range. For precise determination of transmission loss, the muffler must be measured at two different conditions. The two commonly used techniques are the two-load (To, 1979 and Lung, 1983) and two-source (Munjal, 1990) methods. In this work, the two-load method is examined exclusively though many of the conclusions made in this chapter should be transferable to the two-source method.

The two-load method has been standardized in ASTM E2611-09 (ASTM, 2009). Although this standard is geared towards determining the transmission loss through a sound absorbing material, the algorithm and methodology can be applied to measuring muffler transmission loss. As noted in the standard, two different loads are selected.

Both Munjal (Munjal, 1990) and Åbom (Åbom, 1992) pointed out that a potential challenge is to find two different loads at all frequencies of interest. If the two loads are too close, the determined transmission loss is prone to error. The standard recommends using one absorptive load, which allows minimal reflection. The other preferred load is an open or closed termination where significant reflection of sound is anticipated.

Four microphones are mounted along the impedance tube with two upstream and two downstream of the muffler. A reference signal is selected prior to the test, which can be one of the four microphones, the source signal for driving the loudspeaker or a fifth microphone. Based on the reference selected, three or four transfer functions for each load are measured. From these transfer functions; the so-called four-pole parameters for the muffler can be determined along with the transmission loss.

Practically, the cross-sectional area of the impedance tube is fixed and cannot be easily adjusted to fit the dimensions for different mufflers. A pair of conical adapters is sometimes used to transition between impedance tubes and the muffler. An approach to remove the conical adapter transmission loss is proposed in this chapter. And then, the effect of using adapters is discussed.

Secondly, the selection of the reference is investigated by comparing measured results for selecting upstream and downstream references. And then, errors with different references are analyzed numerically. Reference signal selection is unaddressed in the ASTM standard.

6.2 Review of Transmission Loss Measurement

Figure 6.1 shows the transmission loss measurement setup schematically. A speaker is placed at the end of the impedance tube. Two microphones are mounted upstream and the other two microphones are mounted downstream. Two different termination loads are applied and four transfer functions are measured for each load, noted as $H_{1,ref}$, $H_{2,ref}$, $H_{3,ref}$, and $H_{4,ref}$.

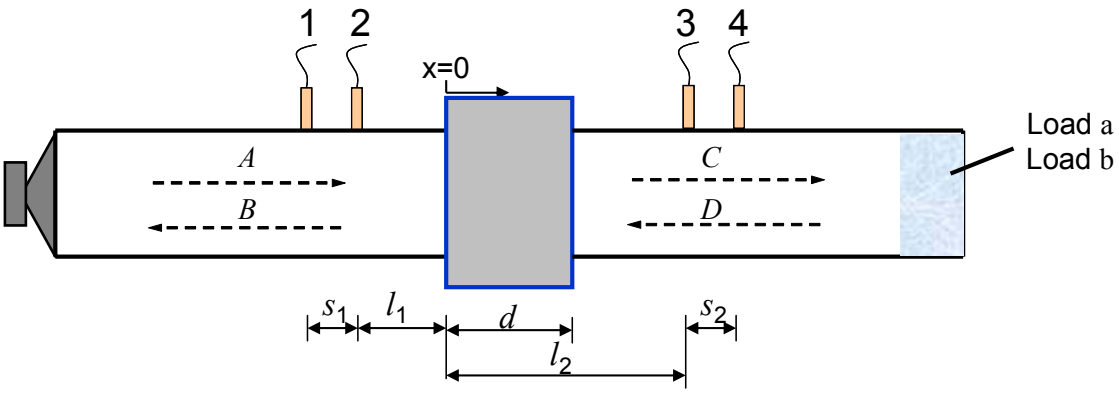

Figure 6.1 Schematic of transmission loss measurement setup.

6.2.1 Wave Decomposition Data Processing

There are two methods to process the measured transfer functions to obtain transmission loss. The first method, which has been standardized in ASTM E2611-09, is based on wave decomposition. By applying wave decomposition at both the upstream and downstream tubes, the wave strength A, B, C, and D can be determined as

$$A = j\frac{H_{1,ref}e^{-jkl_1} - H_{2,ref}e^{-jk(l_1+s_1)}}{2\sin ks_1} \tag{6.1}$$

$$B = j\frac{H_{2.ref}e^{jk(l_1+s_1)} - H_{1,ref}e^{jkl_1}}{2\sin ks_1} \tag{6.2}$$

$$C = j\frac{H_{3,ref}e^{jk(l_2+s_2)} - H_{4,ref}e^{jkl_2}}{2\sin ks_2} \tag{6.3}$$

$$D = j\frac{H_{4,ref}e^{-jkl_2} - H_{3,ref}e^{-jk(l_2+s_2)}}{2\sin ks_2} \tag{6.4}$$

For each load (a or b), pressure and particle velocity at two ends of the sample or muffler are expressed as

$$p_0 = A + B \tag{6.5}$$

$$u_0 = \left(A - B\right)/\,\rho c \tag{6.6}$$

$$p_d = Ce^{-jkd} + De^{jkd} \tag{6.7}$$

$$u_d = \left(Ce^{-jkd} - De^{jkd}\right)/\,\rho c \tag{6.8}$$

The four-pole matrix based on pressure and particle velocity can be written as

$$T = \begin{bmatrix} \dfrac{p_{0a}u_{db} - p_{0b}u_{da}}{p_{da}u_{db} - p_{db}u_{da}} & \dfrac{p_{0b}p_{da} - p_{0a}p_{db}}{p_{da}u_{db} - p_{db}u_{da}} \\ \dfrac{u_{0a}u_{db} - u_{0b}u_{da}}{p_{da}u_{db} - p_{db}u_{da}} & \dfrac{p_{da}u_{0b} - p_{db}u_{0a}}{p_{da}u_{db} - p_{db}u_{da}} \end{bmatrix} \tag{6.9}$$

where the subscripts a and b denote the two different loads. Then, the transmission loss is expressed as

$$TL = 20\log_{10}\left|\frac{1}{2}\left(T_{11} + \frac{T_{12}}{\rho c} + \rho c T_{21} + T_{22}\right)\right| \tag{6.10}$$

The algorithm used is identical to that for the two-source method.

6.2.2 Four-pole Matrix Data Processing

The other well-known method for processing the data follows Munjal (Munjal, 1990) and Tao (Tao, 2003) and was originally used for the two-source method. Instead of the four-pole matrix for the sample, the four-pole matrix between microphones 2 and 3 is calculated. The four-pole parameters can be written as

$$A_{23} = \frac{\Delta_{34}\left(H_{32a}H_{34b} - H_{32b}H_{34a}\right)}{\Delta_{34}\left(H_{34b} - H_{34a}\right)} + \frac{D_{34}\left(H_{32b} - H_{32a}\right)}{\Delta_{34}\left(H_{34b} - H_{34a}\right)} \tag{6.11}$$

$$B_{23} = \frac{B_{34}\left(H_{32a} - H_{32b}\right)}{\Delta_{34}\left(H_{34b} - H_{34a}\right)} \tag{6.12}$$

$$\begin{aligned} C_{23} = & \frac{\left(H_{31a} - A_{12}H_{32a}\right)\left(\Delta_{34}H_{34b} - D_{34}\right)}{B_{12}\Delta_{34}\left(H_{34b} - H_{34a}\right)} \\ & - \frac{\left(H_{31b} - A_{12}H_{32b}\right)\left(\Delta_{34}H_{34a} - D_{34}\right)}{B_{12}\Delta_{34}\left(H_{34b} - H_{34a}\right)} \end{aligned} \tag{6.13}$$

$$D_{23} = \frac{\left(H_{31a} - H_{31b}\right) + A_{12}\left(H_{32b} - H_{32a}\right)}{B_{12}\Delta_{34}\left(H_{34b} - H_{34a}\right)} B_{34} \tag{6.14}$$

where $H_{ij} = p_j/p_i$. A_{ij}, B_{ij}, C_{ij}, and D_{ij} are the corresponding four-pole parameters between microphone i and j, and $\Delta_{ij}=A_{ij}D_{ij}-B_{ij}C_{ij}$. Since additional tube extensions at the inlet and outlet do not modify the transmission loss, the transmission loss can be expressed as

$$TL = 20\log_{10}\left|\frac{1}{2}\left(A_{23} + \frac{B_{23}}{\rho c} + \rho c C_{23} + D_{23}\right)\right| \tag{6.15}$$

In the author's opinion, the wave decomposition method is simpler to use and program. Moreover, it can be used to directly determine the four-pole parameters for the muffler.

6.3 Conical Adapter Effect on Transmission Loss Measurement

6.3.1 Plane Wave Theory with Conical Adapters

Assuming a pair of conical adapters is utilized to transition between the impedance tube and the muffler in the measurement, the measured transfer matrix $[T_{\text{total}}]$ below the cutoff frequency includes the pair of adapters and the muffler itself. It is expressed as

$$\left[T_{total}\right] = \left[T_{cone1}\right]\left[T_{muffler}\right]\left[T_{cone2}\right] \tag{6.16}$$

where $[T_{\text{cone1}}]$ and $[T_{\text{cone2}}]$ are the transfer matrices of the upstream and downstream adapters respectively. $[T_{\text{muffler}}]$ is the transfer matrix of the muffler. The transfer matrix of the divergent conical tube with the length l, and radii r_{u} and r_{d} (shown in Figure 6.2) can be written as (Munjal, 1987)

$$\left[T^{d}\right]=\begin{bmatrix} T_{11}^{d} & T_{12}^{d} \\ T_{21}^{d} & T_{22}^{d} \end{bmatrix} \tag{6.17}$$

where

$$T_{11}^{d}=\frac{x_2}{x_1}\cos\left(k_0 l\right)-\frac{\sin\left(k_0 l\right)}{k_0 x_1} \tag{6.18}$$

$$T_{12}^{d}=j\frac{x_2}{x_1}\sin\left(k_0 l\right) \tag{6.19}$$

$$T_{21}^{d}=j\frac{x_1}{x_2}\left(1+\frac{1}{k_0^2 x_1 x_2}\right)\sin\left(k_0 l\right)-j\left(1-\frac{x_1}{x_2}\right)\frac{\cos\left(k_0 l\right)}{k_0 x_2} \tag{6.20}$$

$$T_{22}^{d}=\frac{\sin\left(k_0 l\right)}{k_0 x_2}+\frac{x_1}{x_2}\cos(k_0 l) \tag{6.21}$$

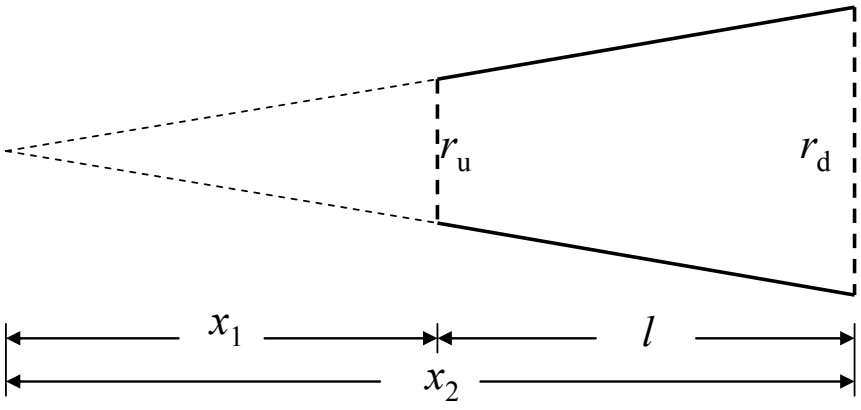

Figure 6.2 The dimensions of a divergent conical adapter.

The transfer matrix of the convergent conical tube is similar and can be written as

$$\left[T^{c}\right]=\begin{bmatrix} T_{22}^{d} & T_{12}^{d} \\ T_{21}^{d} & T_{11}^{d} \end{bmatrix} \tag{6.22}$$

By solving the Equation (6.16), the transfer matrix of the muffler is

$$\left[T_{muffler}\right]=\left[T_{cone1}\right]^{-1}\left[T_{total}\right]\left[T_{cone2}\right]^{-1} \tag{6.23}$$

The transmission loss of the muffler is then calculated using

$$TL=20\log_{10}\left(\frac{1}{2}\left|T_{11}^{muffler}+\frac{T_{12}^{muffler}S_o}{\rho c}+T_{21}^{muffler}\frac{\rho c}{S_i}+T_{22}^{muffler}\frac{S_o}{S_i}\right|\right)+10\log_{10}\left(\frac{S_i}{S_o}\right) \tag{6.24}$$

where S_i and S_o are the cross-sectional area of the inlet and outlet of the muffler, respectively. ρ is the air density and c is the speed of sound.

The measured transmission loss is only valid below the cutoff frequency. If the muffler is smaller than the impedance tube, the cutoff frequency of the muffler is controlled by the cross-sectional size of the inlet and outlet of the impedance tube. If the muffler is larger than the impedance tube, the cutoff of the muffler is determined by the size of the inlet and outlet of the muffler itself.

6.3.2 Cone Effect on Measurements

Although the theory above is straightforward mathematically, it can be problematic in practice. One common concern is that the inlet and outlet diameter to the muffler are not the same diameter as those for the impedance tubes with microphone mountings.

In order to investigate the conical adapter effect on measurement, a barrel was used as an expansion chamber with 152 mm diameter inlet and outlet holes on each side. Since the impedance tube diameter is only 34.8 mm, two pairs of

conical adapters with different lengths were built as shown in Figure 6.3. The dimensions of each part are listed in Table 6-1.

Figure 6.3 Photos of barrel and adapters.

Table 6-1 Dimensions of barrel and adapters

	Expansion Chamber	Long Adapters	Short Adapters
Length	445 mm	632 mm	197 mm
Small Diameter	356 mm	34.8 mm	34.8 mm
Large Diameter		152 mm	152 mm

The transmission losses of the expansion chamber with the different adapter pairs were measured using the wave decomposition algorithm. The transmission losses with long and short adapters are shown in Figure 6.4 and Figure 6.5 respectively. The cutoff frequency of the measurement is around 5650 Hz, which is determined by the size of the ACUPRO impedance tube provided by

Spectronics Inc (ACUPRO, 2013). Sidlab (SIDLAB, 2011) was used to model the duct system using 1-D plane wave theory and 1-D solutions were provided for comparison. The higher order behavior in the chamber is considered (Åbom, 1990) but the sound inside the adapters is assumed to be plane wave. Accordingly, the cutoff frequency for the analytical solutions is governed by the size of the adapters and should be around 1300 Hz.

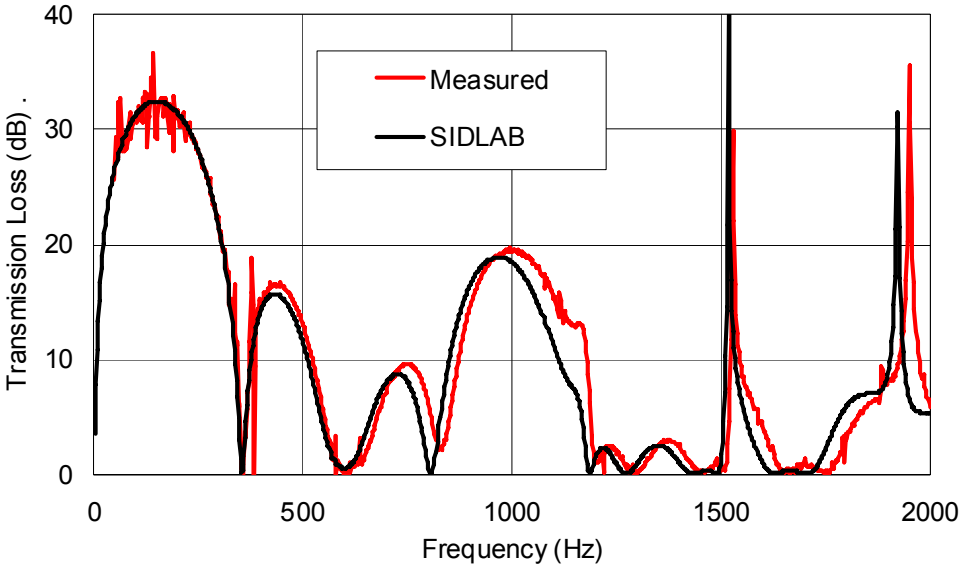

Figure 6.4 Transmission loss of the expansion chamber with short conical adapters.

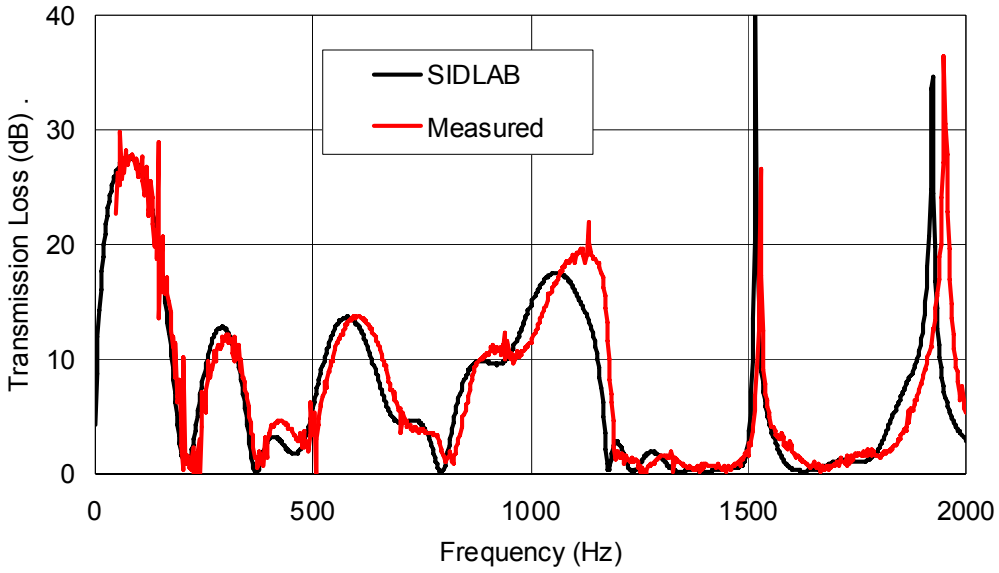

Figure 6.5 Transmission loss of the expansion chamber with long conical adapters.

The measured transmission loss generally agrees well with the analytical solution for both cases. In Figure 6.4, the transmission loss below 200 Hz is noisy, which is understandable because the transmission loss is high and the source power is not sufficient because a compression driver is used. The results agree very well between 200 Hz and 600 Hz. The shift at high frequency is understandable due to the geometry mismatch between the barrel and the simple expansion chamber. In Figure 6.5, the results agree well with a slight shift at high frequencies.

By applying transfer matrix theory (Equation (6.23)), the effect of the cones can be removed, and the transmission loss of the expansion chamber itself is compared in Figure 6.6. It is shown that the results are very noisy and do not agree well with the analytical transmission loss at low frequencies (below 200 Hz) for both cases. However, the transmission loss using long adapters compares well with the analytical solution above 200 Hz, whereas the transmission loss using short adapters compares well only above 700 Hz.

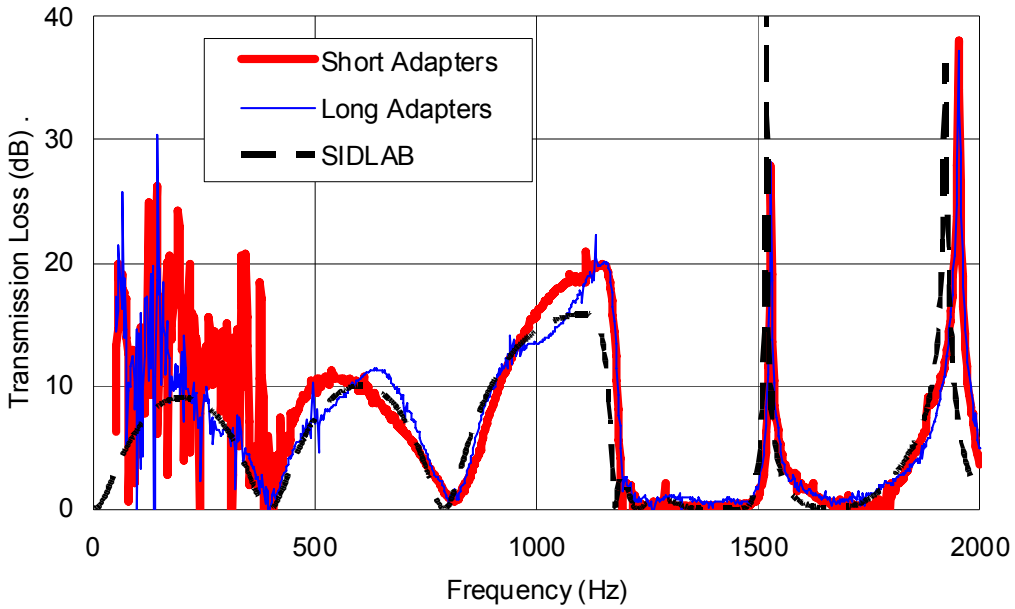

Figure 6.6 Transmission loss of the expansion chamber without conical adapters.

The most likely explanation is that conical adapters introduce additional transmission loss especially at low frequencies. After the effect of the conical pairs is removed, the error from the measurement remains and is significantly amplified due to the inversion process. Figure 6.7 compares the transmission loss of the expansion chamber using short conical adapters and the analytical transmission loss of the short conical adapter couple. The transmission loss of the short adapter couple is much higher than the transmission loss of the chamber below 500 Hz. The corresponding comparison by using long conical adapters is shown in Figure 6.8. The transmission loss of the long adapter couple is much higher than the transmission loss of the chamber below 200 Hz. The transmission loss of the long conical adapter couple is much smaller than the expansion chamber beyond 200 Hz.

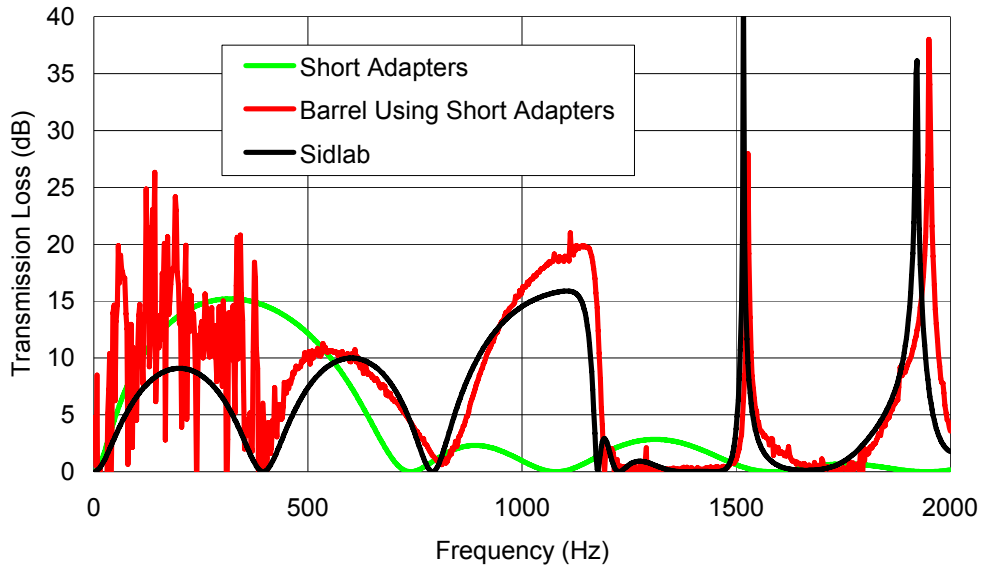

Figure 6.7 Transmission loss of the expansion chamber using short conical adapters and transmission loss of the short adapter couple.

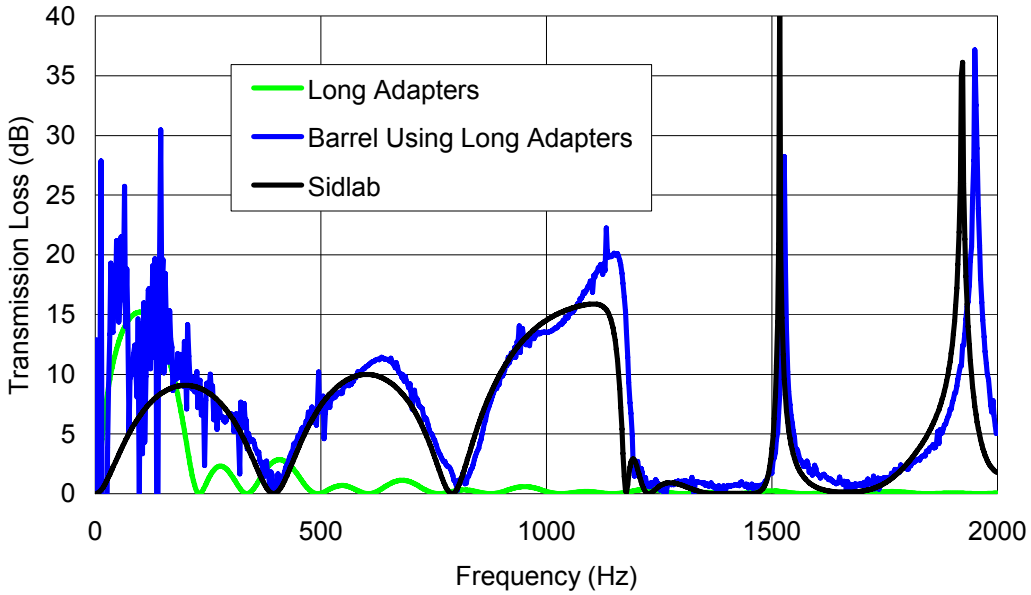

Figure 6.8 Transmission loss of the expansion chamber using long conical adapters and transmission loss of the long adapter couple.

Figure 6.9 shows the transmission loss of conical adapters with different sizes and lengths connected with each other, where l is the length of a single adapter. The first lobe in transmission loss is much higher than the following lobes. The length of the cone determines the width of the first lobe, whereas the height of the lobe is determined by the area ratio of the cone. Since the area ratio for the conical adapters is 19, the peak of the first lobe is approximately 15 dB, which is much higher than the transmission loss of the expansion chamber itself at low frequency. Hence, the conical adapter behavior dominates the transmission loss at low frequencies.

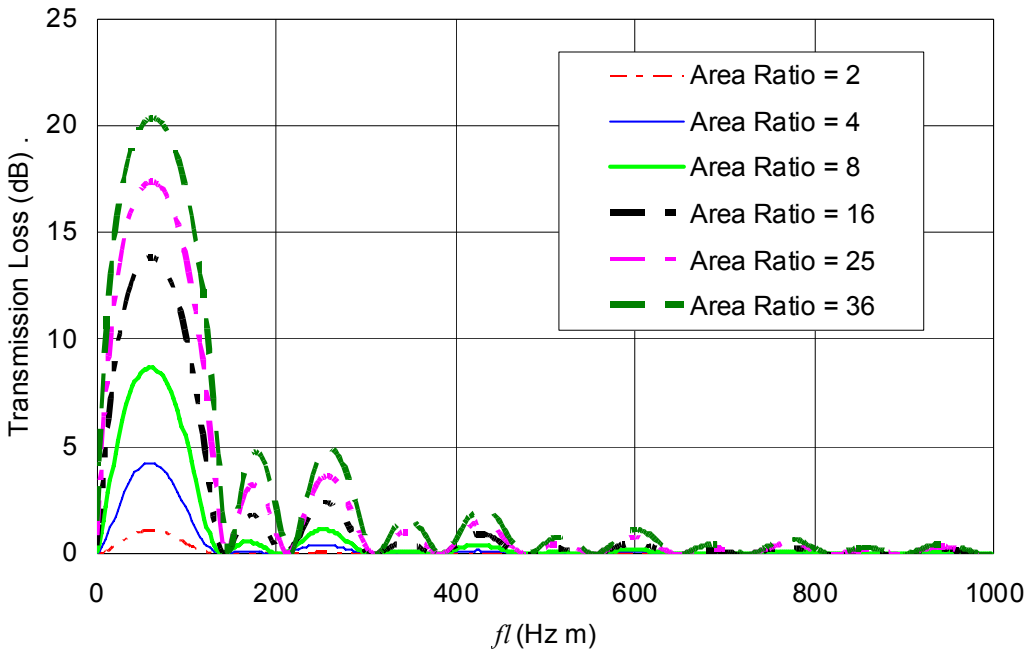

Figure 6.9 Transmission loss of conical pairs with different lengths and area ratios.

When small mufflers are measured, a pair of reversed adapters may be used. The corresponding transmission loss plots with different sizes and lengths are shown in Figure 6.10. The dominant lobe is still the first but with a lower transmission loss.

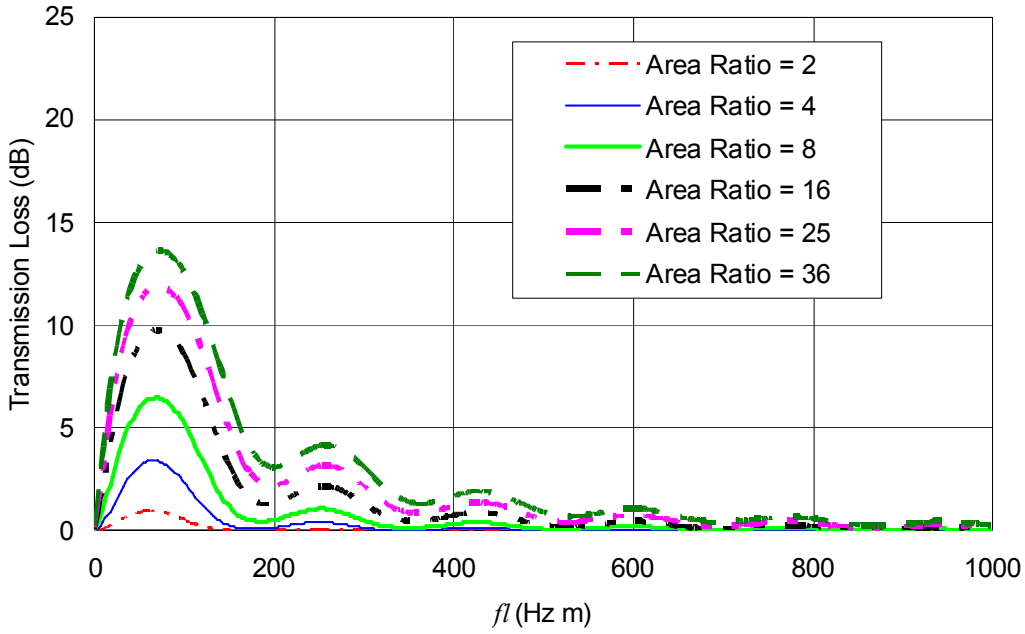

Figure 6.10 Transmission loss of reversed conical pairs with different lengths and area ratios.

By selecting a suitable length for the conical adapters, the measured transmission loss will not be compromised by the cones. Figure 6.11 shows dimensions of such a real muffler. The area ratios on the inlet and outlet sides are approximately 4 and 1 respectively. The length of the conical adapters is .178 m. Figure 6.12 shows the comparison of the measured and the simulated transmission loss sans conical adapters using Equation (6.23). The results compare well even at low frequencies.

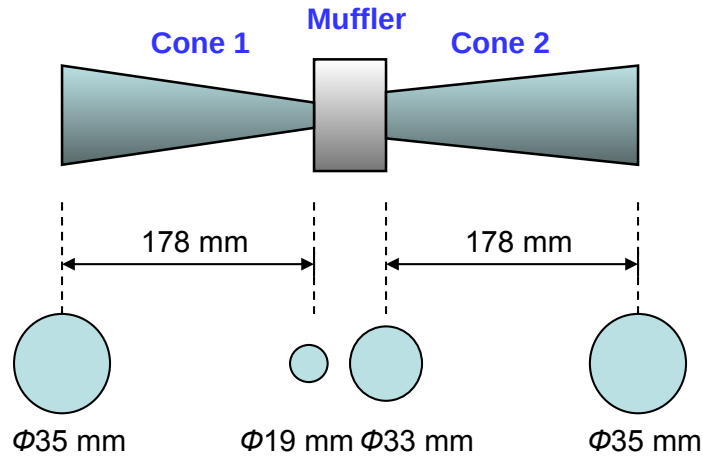

Figure 6.11 Dimensions of a real muffler and its adapters.

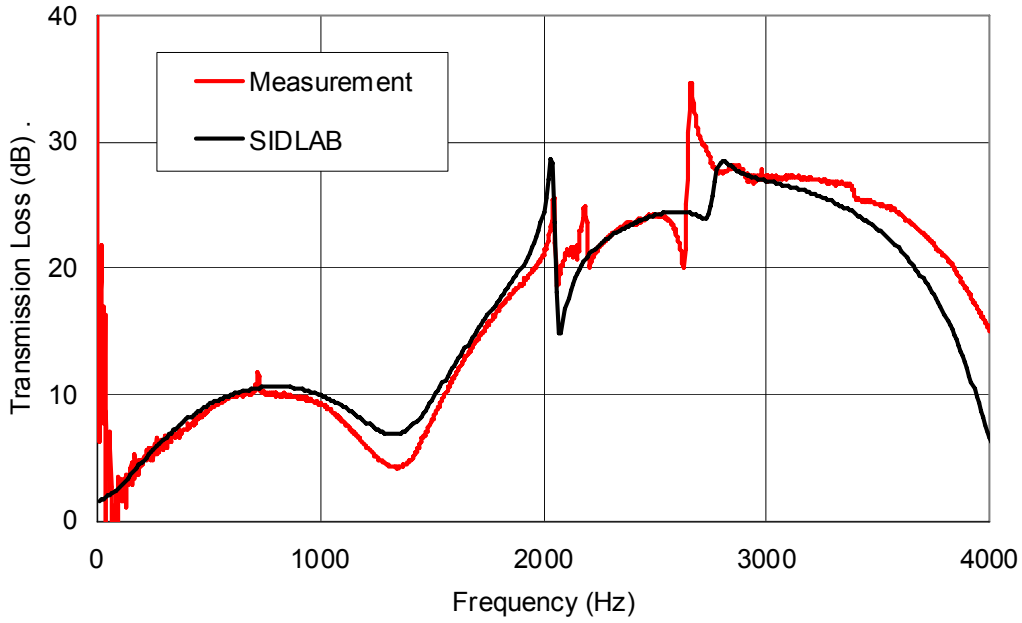

Figure 6.12 Comparison of measured and simulated muffler transmission loss without conical adapters.

For mufflers very close in diameter to the impedance tube, the conical area ratio is very low and the adapter effect is minimal. In those cases, using different lengths of adapters will lead to a similar accuracy in the transmission loss. This

will be the case even for a sudden expansion and/or contraction, which can be thought of as a very short conical adapter.

For mufflers with a large area ratio, a pair of long adapters is recommended for a smooth and accurate transmission loss at low frequencies. With long conical adapters, the high transmission loss of the adapters is pushed to lower frequencies. This suggests that the effect of the cones connected to each other should first be examined before measuring the transmission loss of the muffler itself.

6.4 Two-load Method Error Analysis

6.4.1 Experimental Analysis

Using the wave decomposition algorithm, four transfer functions are measured for each load, which are $H_{1,ref}$, $H_{2,ref}$, $H_{3,ref}$ and $H_{4,ref}$. For convenience, the reference signal is selected as one of the four microphones. And hence the number of the transfer functions measured is reduced to three for each load because one of the four transfer functions is unity. The reference signal selection will affect the measured transmission loss, although they are equivalent theoretically.

In order to investigate the effect of reference signal, a simple expansion chamber was constructed with 11.5 mm thick plastic. The length was 200 mm and the inner diameter was 150 mm. The inlet and outlet diameter was 34.8 mm, which exactly matched the impedance tube. Although this muffler was geometrically symmetric so that only one load was required, the two-load method was applied.

The test setup and microphones positions are shown in Figure 6.1. Both microphone spacings s_1 and s_2 are 29.2 mm. The lengths of the upstream and downstream tubes are 787 mm and 406 mm, respectively. Load a is an open tube. Load b is a 100 mm acoustic foam with a blocked end.

The transmission loss was measured using different references and results are compared in Figure 6.13. The four curves generally have excellent agreement. However, there is significant noise at 100 and 400 Hz if microphone 1 or 2 is

selected as reference whereas the measurement is smooth using reference 3 or 4 for the entire frequency band. Figure 6.14 and Figure 6.15 compare the measured four-pole parameters with reference 1 and 3 respectively. The curves for T_{21} and T_{22} with reference 1 are very noisy at about 400 Hz.

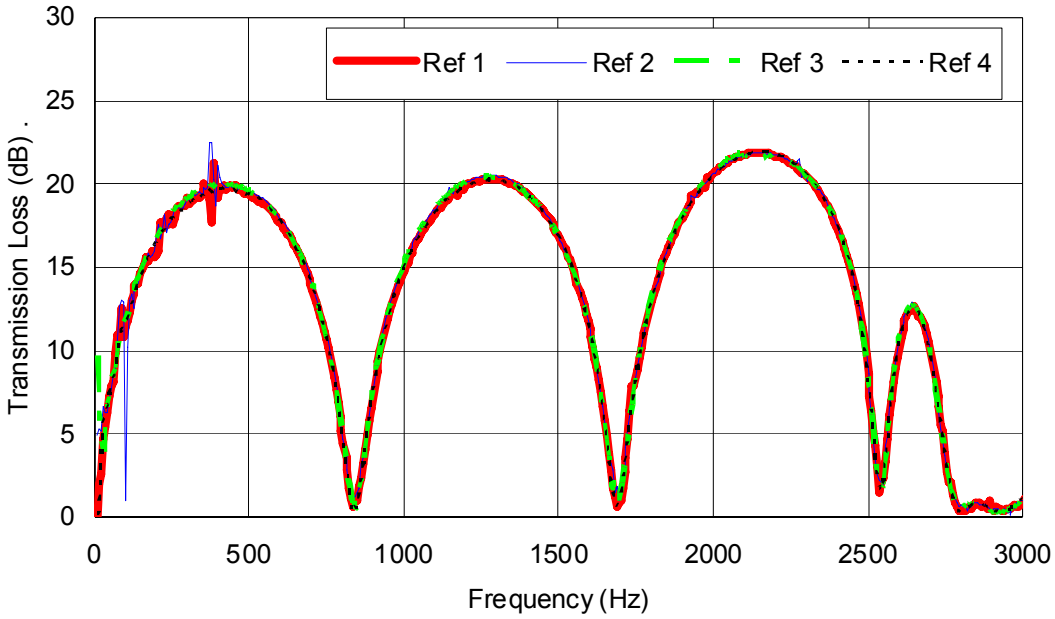

Figure 6.13 Measured transmission loss of the simple expansion chamber with different reference signals.

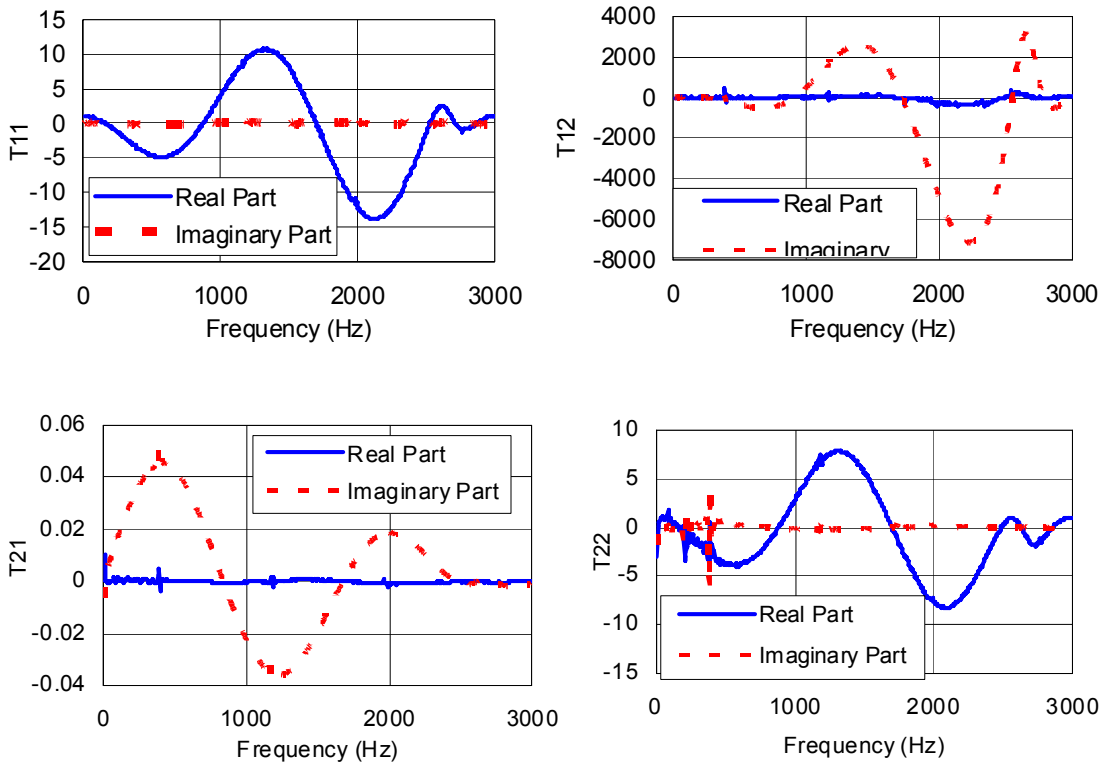

Figure 6.14 Measured four-pole parameters of the simple expansion chamber with reference 1.

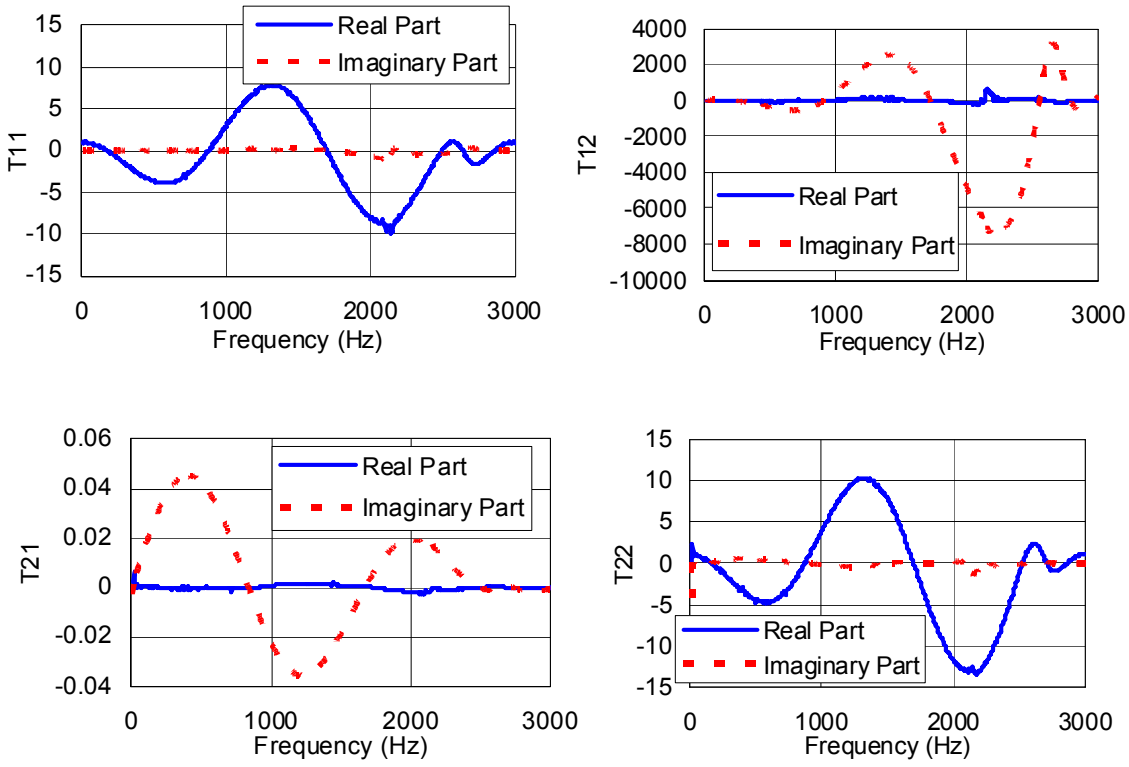

Figure 6.15 Measured four-pole parameters of the simple expansion chamber with reference 3.

This phenomenon is apparent not only for the simple expansion chamber, but is also present for other reactive mufflers. The transmission loss of one such muffler is shown in Figure 6.16. When microphone 1 is selected as reference, the measured transmission loss is noisy at 225 Hz, 330 Hz, 620 Hz and so forth. When reference 3 is selected, the transmission loss is very smooth for the entire frequency band with the only exception being at around 700 Hz.

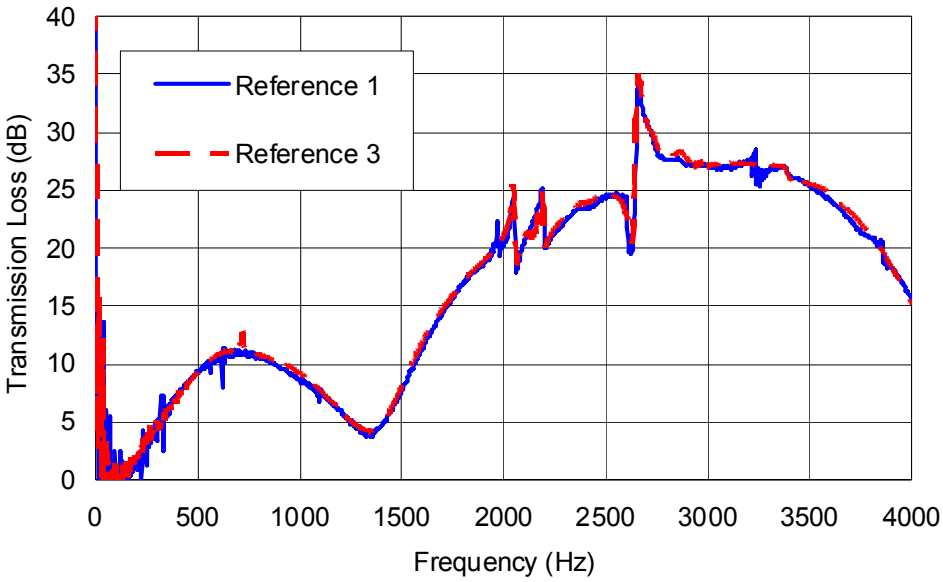

Figure 6.16 Measured transmission loss of a reactive muffler with different reference signals

Note that p_{d} and u_{d} occur in the denominator for each term in the transfer matrix (Equation (6.9)) where errors may be amplified significantly. p_{d} and u_{d} are determined from C and D which depend solely on $H_{3,ref}$ or $H_{4,ref}$.

If an upstream microphone is selected as reference, either $H_{1,ref}$ or $H_{2,ref}$ is reduced to 1 without any measured error. Similarly, the errors for $H_{3,ref}$ or $H_{4,ref}$ are eliminated if a downstream microphone is selected as a reference. Moreover, the coherence will be higher for both $H_{3,ref}$ and $H_{4,ref}$ if a downstream microphone is selected.

6.4.2 Direct Numerical Simulation

In order to validate the effect of selecting reference signal, a direct numerical analysis is demonstrated. Analytical four-poles of the simple expansion chamber are obtained via Sidlab. The termination impedances Z_t of the two different loads are measured and shown in Figure 6.17. And then, the transfer function between the ith microphone and the termination pressure can be calculated using

$$H_{i,t} = \frac{p_i}{p_t} = T_{11}^{it} + \frac{T_{12}^{it}}{Z_t} \tag{6.25}$$

where p_i and p_t are sound pressure at the ith microphone and the termination respectively. ${T_{11}}^{it}$ and ${T_{12}}^{it}$ are corresponding four-pole elements from the microphone i to the termination. The transfer function between any microphone pair is constructed numerically.

Figure 6.18 and Figure 6.19 show the comparison between measured and numerically constructed transfer functions H_{13a} and H_{31a} respectively. A phase jump occurs at both 100 Hz and 400 Hz, where a node coincides with microphone 1. At these frequencies, the coherence is low and significant errors may be apparent into both magnitude and phase (Seybert, 1981 and Åbom, 1988).

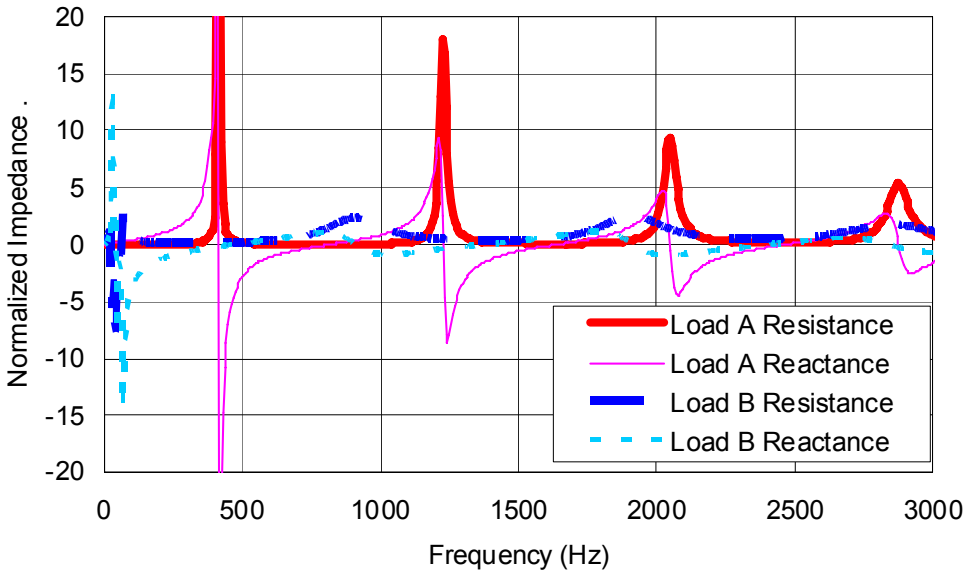

Figure 6.17 Termination impedances of the two different loads. (load a: open; load b: closed with 100 mm foam)

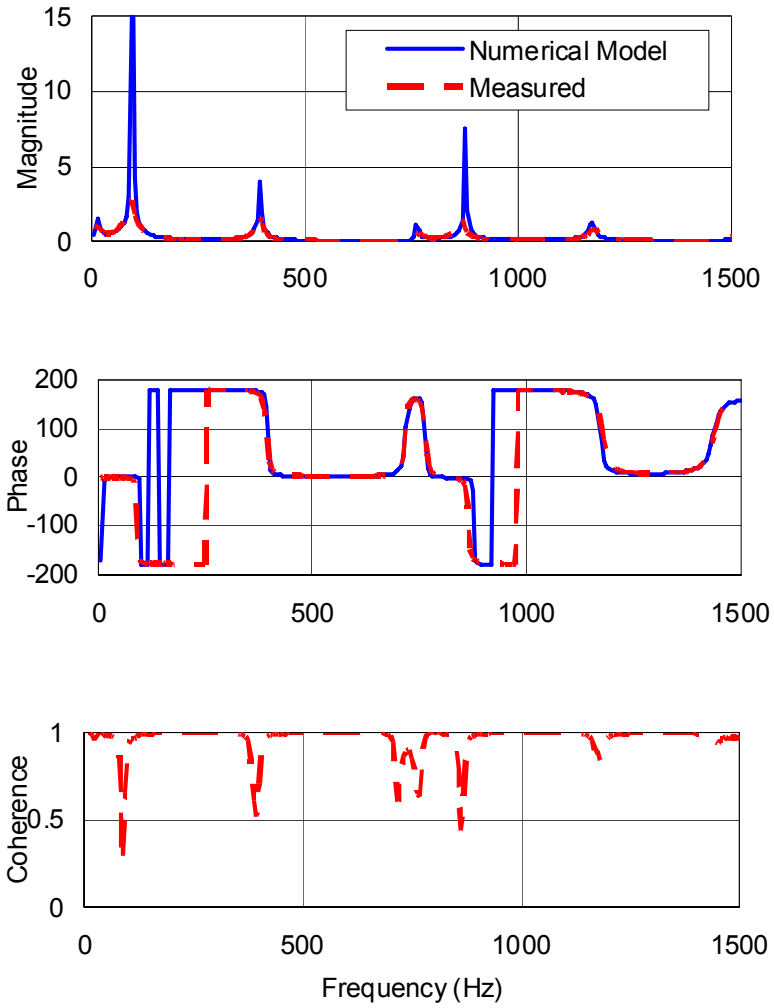

Figure 6.18 Measured and simulated transfer function H_{13a} of the simple expansion chamber

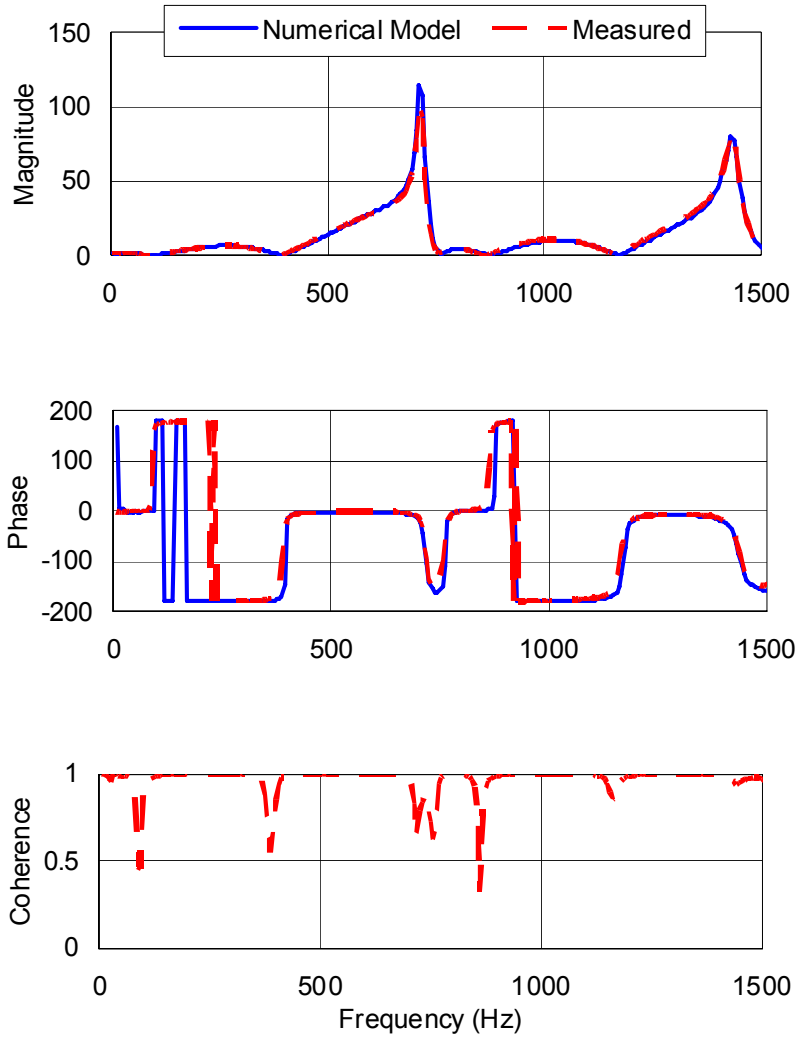

Figure 6.19 Measured and simulated transfer function H_{31a} of the simple expansion chamber.

Note that microphones that are in close proximity to one another on the same side of the muffler normally have good coherence and minimal error. If the microphones are separated by the muffler, the coherence is normally poor at certain frequencies. Accordingly, it is reasonable to assume that H_{12} or H_{34} will have minimal error and hence error is assumed to be negligible. However, higher errors are anticipated for H_{13}, H_{14}, H_{31}, and H_{32}.

By examining Equation 1, it can be seen that errors will accumulate on C and D if an upstream microphone is chosen as a reference and on A and B for a downstream microphone.

In order to compare the errors with reference 1 and 3, some assumptions are made in order to simplify the error analysis. First, errors occur only on the transfer functions H_{13} and H_{31} with the reactive load. Secondly, error levels on H_{13} and H_{31} are the same. Other transfer functions are assumed to have no error. If errors on H_{14} and H_{32} were included, errors in A, B, C, and D will be increased by a factor 2 but the conclusions will remain the same.

A 10% magnitude error and a 10° phase error are artificially applied onto the transfer function H_{13a} and H_{31a} over the entire frequency range. Figure 6.20 shows the error in transmission loss versus frequency. It can be seen that errors will be higher for reference 1 at approximately 60% of the frequencies. Additionally, the error standard deviation is 1.4 dB for reference 1 compared to 0.9 dB for reference 3. Note that the relative errors predicted in Figure 6.20 manifest themselves in the transmission loss measurement shown in Figure 6.13. There are high errors if microphone 1 is chosen at both 100 and 400 Hz. Also, note that the errors are higher for reference 3 at 2175 Hz.

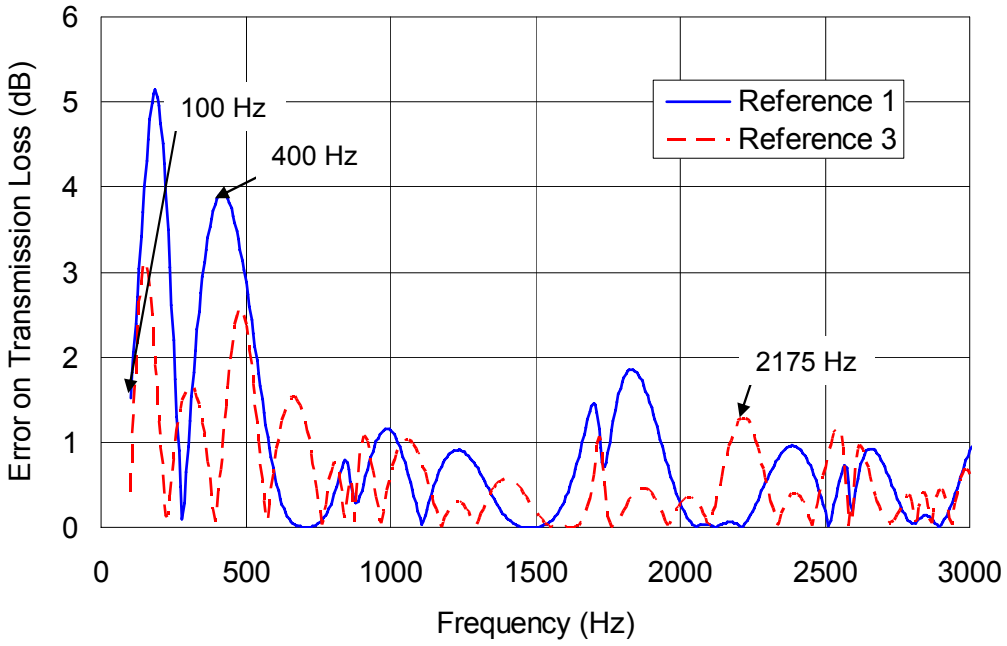

Figure 6.20 Error on transmission loss of the simple expansion chamber with 10% and 10° measured error on transfer functions H_{13a} and H_{31a} respectively.

The numerical error analysis above is for a simple expansion chamber, which is a typical case of reactive mufflers. For dissipative mufflers, the effect of selecting a reference is not as important. Four-pole parameters of a 50 mm acoustic foam with 15000 rayls/m flow resistivity are obtained using Wu's model (Wu, 1988). Using the method discussed above, a node is found at 594 Hz. Figure 6.21 shows the error in transmission loss versus frequency. It is evident that the errors on transmission loss are minimal with 10% and 10° magnitude and phase errors respectively.

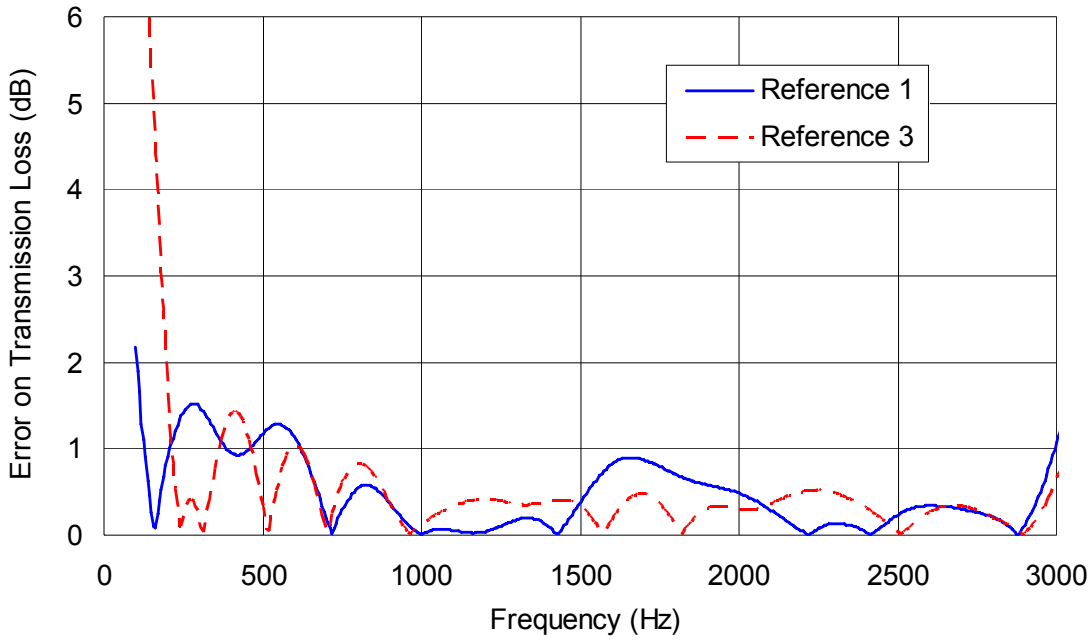

Figure 6.21 Error on transmission loss of the acoustic foam with 10% and 10° measured error on transfer functions H_{13a} and H_{31a} respectively.

6.4.3 Analytical Error Analysis

Although the direct numerical simulation above is straightforward, a sensitivity analysis using a Taylor expansion is more suitable for drawing general conclusions. In this section, the sensitivities of errors on H_{13a} and H_{31a} to each four-pole parameter are determined.

Errors on the measured transfer function will first accumulate on the incident and reflected wave amplitudes (A, B, C, and D) and then propagate to each of the four-pole parameters. If microphone 1 is the reference, the errors of the transfer function between microphone 1 and 3 occur on H_{13a}, then accumulate to C_a and D_a, and finally propagate to each of the four-pole parameters. If microphone 3 is the reference, the errors of the transfer function between microphone 1 and 3 occur on H_{31a}, and then propagate to the four-pole parameters via A_a and B_a.

When microphone 1 is the reference, the sensitivities of C_a and D_a to the H_{13a} error can be calculated from Equations (6.1) to (6.4) using

$$\frac{\partial C_a}{\partial H_{13a}} = \frac{je^{jk(l_2+s_2)}}{2\sin ks_2} \tag{6.26}$$

$$\frac{\partial D_a}{\partial H_{13a}} = \frac{-je^{-jk(l_2+s_2)}}{2\sin ks_2} \tag{6.27}$$

It follows that the sensitivities of the four-pole parameter T_{11}, T_{12}, T_{21}, and T_{22} to C_a and D_a errors can be calculated using

$$\frac{\partial T_{11}}{\partial C_a} = \frac{-p_{0b}/\rho c}{p_{da}u_{db} - p_{db}u_{da}} - \frac{(p_{0a}u_{db} - p_{0b}u_{da})(u_{db} - p_{db}/\rho c)}{(p_{da}u_{db} - p_{db}u_{da})^2} \tag{6.28}$$

$$\frac{\partial T_{11}}{\partial D_a} = \frac{p_{0b}/\rho c}{p_{da}u_{db} - p_{db}u_{da}} - \frac{(p_{0a}u_{db} - p_{0b}u_{da})(u_{db} + p_{db}/\rho c)}{(p_{da}u_{db} - p_{db}u_{da})^2} \tag{6.29}$$

$$\frac{\partial T_{12}}{\partial C_a} = \frac{p_{0b}}{p_{da}u_{db} - p_{db}u_{da}} - \frac{(p_{0b}p_{da} - p_{0a}p_{db})(u_{db} - p_{db}/\rho c)}{(p_{da}u_{db} - p_{db}u_{da})^2} \tag{6.30}$$

$$\frac{\partial T_{12}}{\partial D_a} = \frac{p_{0b}}{p_{da}u_{db} - p_{db}u_{da}} - \frac{(p_{0b}p_{da} - p_{0a}p_{db})(u_{db} + p_{db}/\rho c)}{(p_{da}u_{db} - p_{db}u_{da})^2} \tag{6.31}$$

$$\frac{\partial T_{21}}{\partial C_a} = \frac{-u_{0b}/\rho c}{p_{da}u_{db} - p_{db}u_{da}} - \frac{(u_{0a}u_{db} - u_{0b}u_{da})(u_{db} - p_{db}/\rho c)}{(p_{da}u_{db} - p_{db}u_{da})^2} \tag{6.32}$$

$$\frac{\partial T_{21}}{\partial D_a} = \frac{u_{0b}/\rho c}{p_{da}u_{db} - p_{db}u_{da}} - \frac{(u_{0a}u_{db} - u_{0b}u_{da})(u_{db} + p_{db}/\rho c)}{(p_{da}u_{db} - p_{db}u_{da})^2} \tag{6.33}$$

$$\frac{\partial T_{22}}{\partial C_a} = \frac{u_{0b}/\rho c}{p_{da}u_{db} - p_{db}u_{da}} - \frac{(p_{da}u_{0b} - p_{db}u_{0a})(u_{db} - p_{db}/\rho c)}{(p_{da}u_{db} - p_{db}u_{da})^2} \tag{6.34}$$

$$\frac{\partial T_{22}}{\partial D_a} = \frac{u_{0b}/\rho c}{p_{da}u_{db} - p_{db}u_{da}} - \frac{\left(p_{da}u_{0b} - p_{db}u_{0a}\right)\left(u_{db} + p_{db}/\rho c\right)}{\left(p_{da}u_{db} - p_{db}u_{da}\right)^2} \tag{6.35}$$

Then, the sensitivities of T_{ij} to H_{13a} errors can be calculated using

$$\frac{\partial T_{ij}}{\partial H_{13a}} = \frac{\partial T_{ij}}{\partial C_a}\frac{\partial C_a}{\partial H_{13a}} + \frac{\partial T_{ij}}{\partial D_a}\frac{\partial D_a}{\partial H_{13a}} \tag{6.36}$$

Similarly, when microphone 3 is the reference, the sensitivities of A_a and B_a to H_{31a} error can be calculated using

$$\frac{\partial A_a}{\partial H_{31a}} = \frac{je^{-jkl_1}}{2\sin ks_1} \tag{6.37}$$

$$\frac{\partial B_a}{\partial H_{31a}} = \frac{-je^{jkl_1}}{2\sin ks_1} \tag{6.38}$$

The sensitivities of the four-pole parameter T_{11}, T_{12}, T_{21}, and T_{22} to A_a and B_a errors can be calculated using

$$\frac{\partial T_{11}}{\partial A_a} = \frac{u_{db}}{p_{da}u_{db} - p_{db}u_{da}} \tag{6.39}$$

$$\frac{\partial T_{11}}{\partial B_a} = \frac{u_{db}}{p_{da}u_{db} - p_{db}u_{da}} \tag{6.40}$$

$$\frac{\partial T_{12}}{\partial A_a} = \frac{-p_{db}}{p_{da}u_{db} - p_{db}u_{da}} \tag{6.41}$$

$$\frac{\partial T_{12}}{\partial B_a} = \frac{-p_{db}}{p_{da}u_{db} - p_{db}u_{da}} \tag{6.42}$$

$$\frac{\partial T_{21}}{\partial A_a} = \frac{u_{db}/\rho c}{p_{da}u_{db} - p_{db}u_{da}} \tag{6.43}$$

$$\frac{\partial T_{21}}{\partial B_a} = \frac{-u_{db}/\rho c}{p_{da}u_{db} - p_{db}u_{da}} \tag{6.44}$$

$$\frac{\partial T_{22}}{\partial A_a} = \frac{-p_{db}/\rho c}{p_{da}u_{db} - p_{db}u_{da}} \tag{6.45}$$

$$\frac{\partial T_{22}}{\partial B_a} = \frac{p_{db}/\rho c}{p_{da}u_{db} - p_{db}u_{da}} \tag{6.46}$$

In a similar manner, the sensitivities of T_{ij} to H_{31a} error can be calculated via

$$\frac{\partial T_{ij}}{\partial H_{31a}} = \frac{\partial T_{ij}}{\partial A_a}\frac{\partial A_a}{\partial H_{31a}} + \frac{\partial T_{ij}}{\partial B_a}\frac{\partial B_a}{\partial H_{31a}} \tag{6.47}$$

For the reactive muffler case discussed before, the sensitivities of each four-pole parameter to the H_{13a} and H_{31a} errors are shown in Figure 6.22 and Figure 6.23 respectively. It is apparent that the sensitivities with reference 1 are more significant than with reference 3. Moreover, with reference 1, the sensitivities on T_{21} and T_{22} are more significant than those on T_{11} and T_{12} for most of the frequency range, especially at around 400 Hz, where phase jump occurs. This is consistent to the numerical simulation result and the observed result of the real measurement. For the dissipative muffler case discussed before, the sensitivities of the H_{13a} error and H_{31a} error to each four-pole parameter are shown in Figure 6.24 and Figure 6.25 respectively. It can be observed that the sensitivities are much lower.

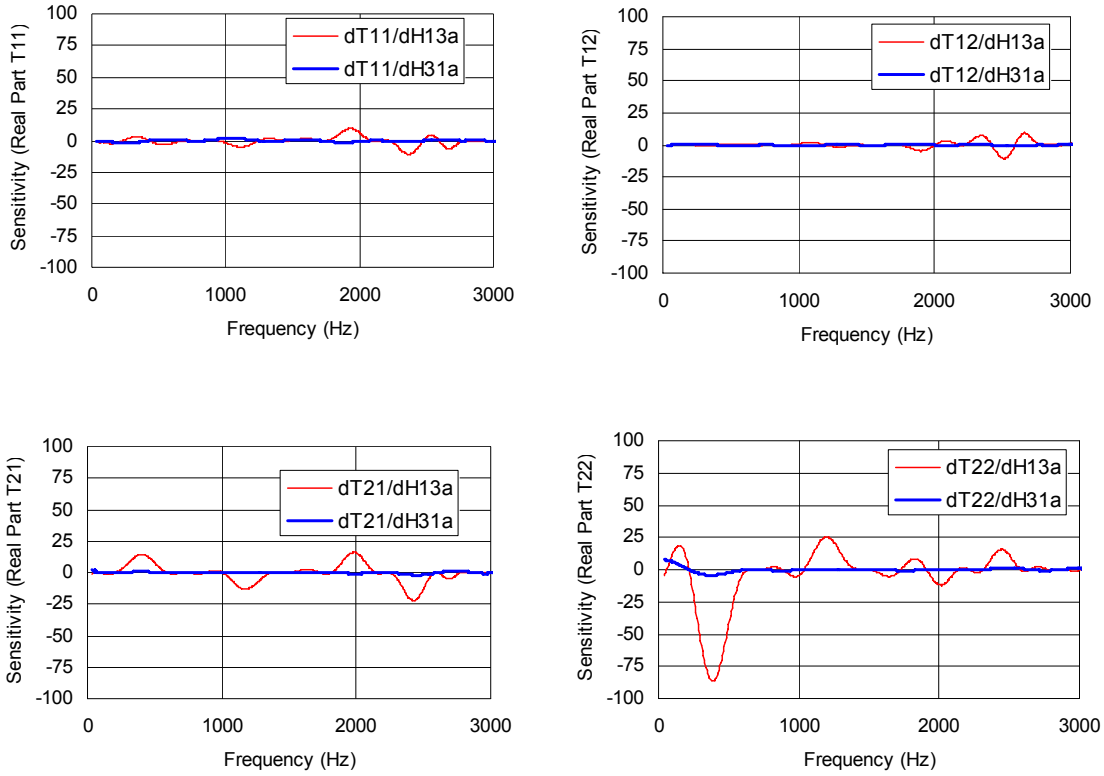

Figure 6.22 The sensitivities of each four-pole parameter to the H_{13a} and H_{31a} (real part) of the simple expansion chamber.

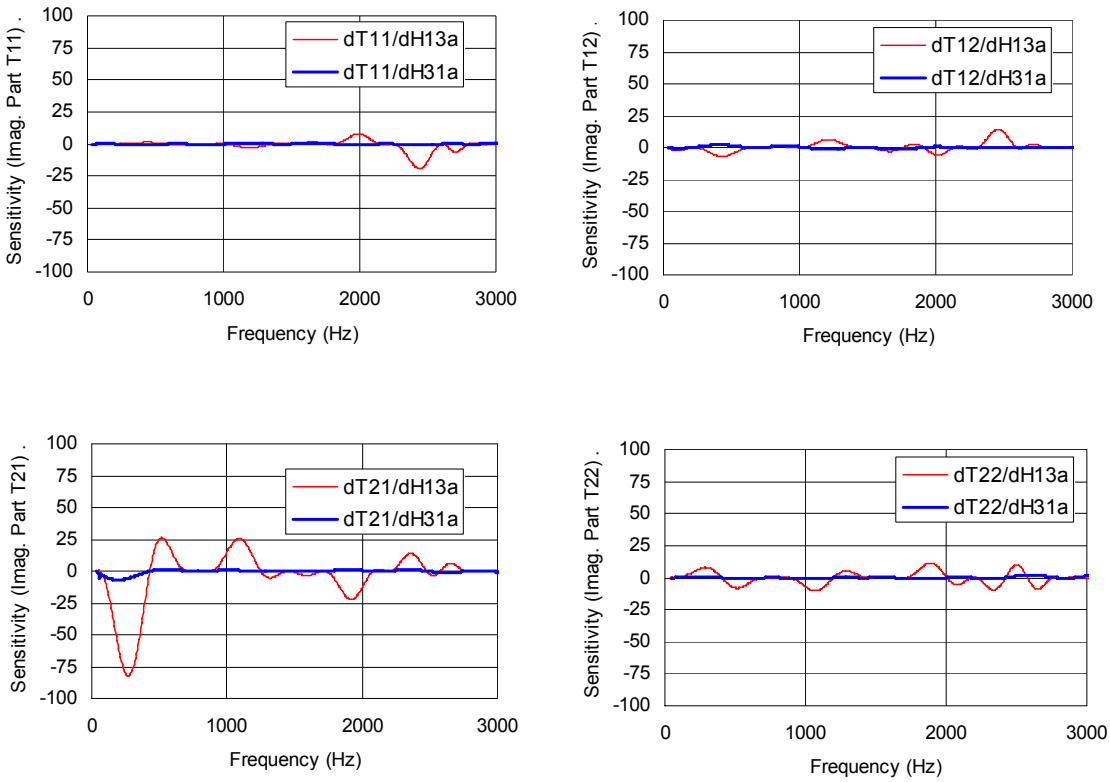

Figure 6.23 The sensitivities of each four-pole parameter to the H_{13a} and H_{31a} (imaginary part) of the simple expansion chamber.

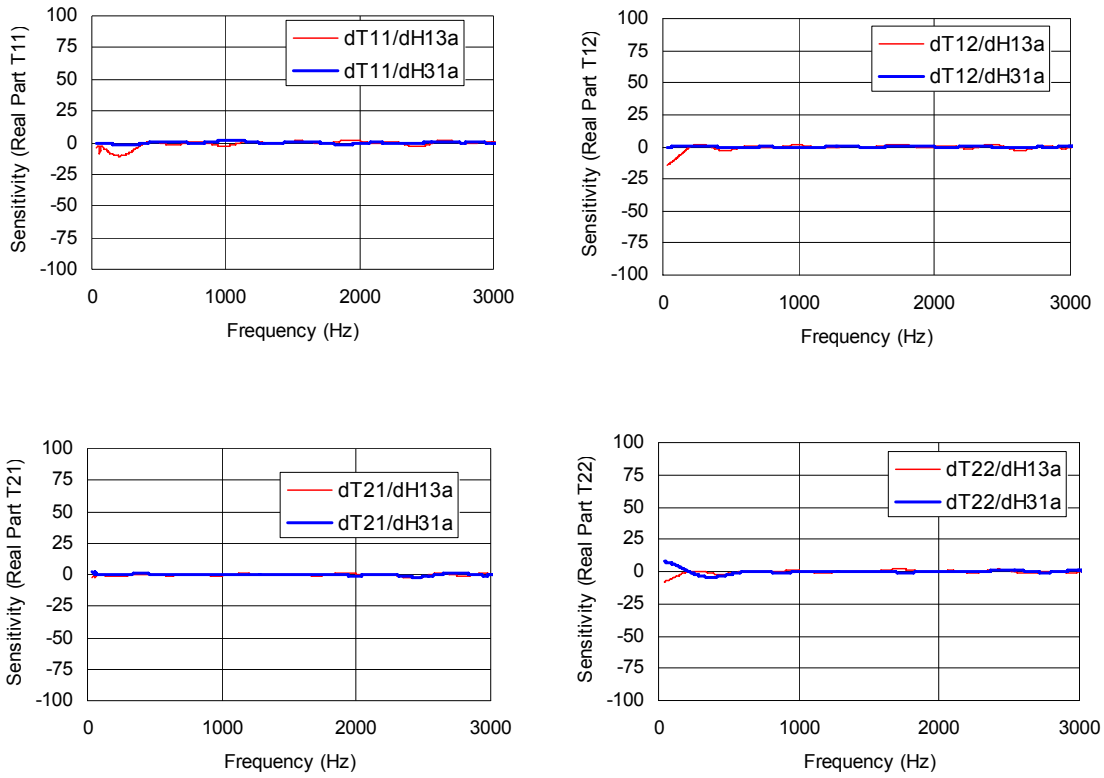

Figure 6.24 The sensitivities of each four-pole parameter to the H_{13a} and H_{31a} (real part) of the 50 mm foam.

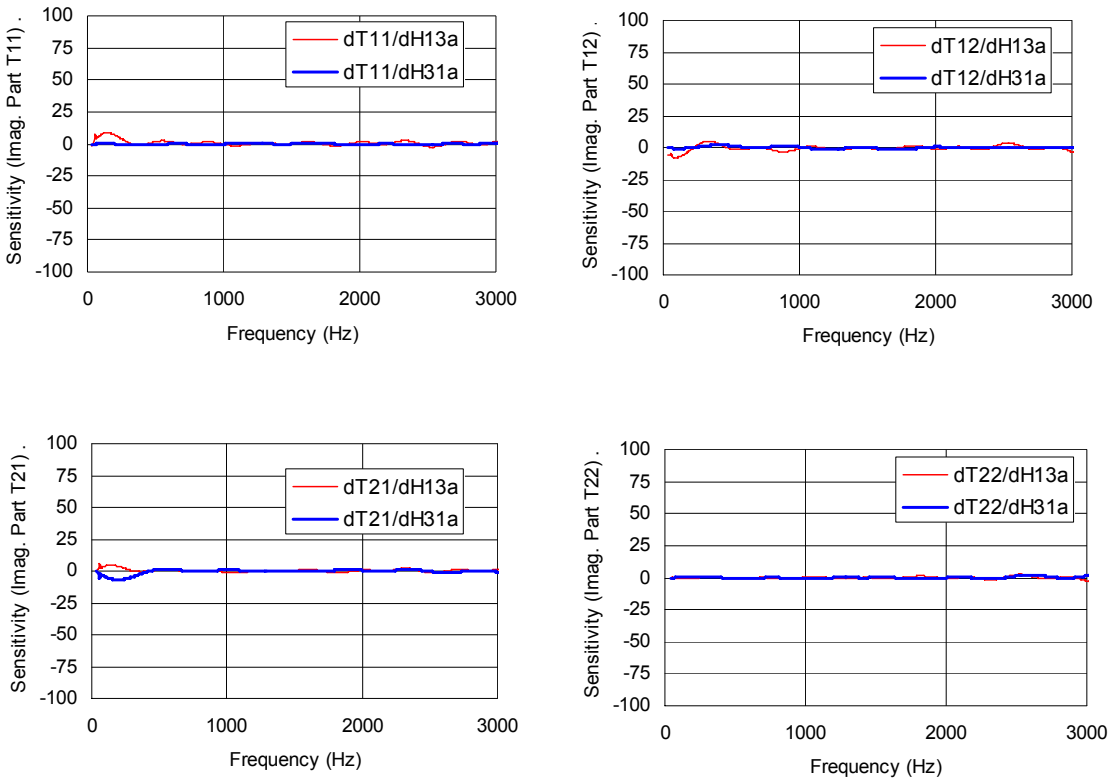

Figure 6.25 The sensitivities of each four-pole parameter to the H_{13a} and H_{31a} parameter (imaginary part) of the 50 mm foam.

6.5 Summary

Several aspects of using the two-load method to determine the transmission loss have been examined in this chapter. First of all, the effect of using conical adaptors was examined. It was demonstrated that conical adapters significantly effect the measurement of transmission loss at low frequencies. In order to minimize the effect the area ratio should be minimized and the length of the cone maximized. The effect of using conical adapters can be easily evaluated prior to an experiment by determining the transmission loss, either analytically or experimentally, of the two cones placed together as shown in Figure 6.9 and Figure 6.10.

The choice of reference has also been investigated experimentally, numerically and analytically. For measuring reactive mufflers with a reflective termination, transfer functions between an upstream microphone and a downstream microphone will have some errors, especially at those frequencies where a standing wave node coincides with the reference microphone. By examining the algorithm in Equations (6.1) to (6.9), it was shown that it is preferable that errors accumulate into the upstream wave amplitudes A and B rather than the downstream wave amplitudes C and D. It was shown that selecting a downstream microphone as a reference will improve the measurement quality. This conclusion will be applicable if the muffler is reactive and one of the acoustic loads is reflective. Moreover, it was assumed that white noise was used for the source and that flow was not included.

In prior work, Tao and Seybert (Tao, 2003) had noted that the two-source method might be superior to the two-load. However, this conclusion should be reevaluated since an upstream microphone was chosen as a reference.

Chapter 7 DESCRIPTION AND DETERMINATION OF TRANSMISSION AND INSERTION LOSS FOR MULTI-INLET MUFFLERS

7.1 Introduction

The extant literature on mufflers and silencers is primarily focused on the single inlet and outlet case (Alfredson, 1971, Cummings, 1975, Prasad, 1981, Jayaraman, 1981, Sullivan, 1979, Ih, 1985, Davis, 1987, Åbom, 1987, Munjal, 1987, Davies, 1988, Peat, 1988, Eriksson, 1983, Seybert, 1987, Åbom, 1990, Dokumaci, 1997, Selamet, 1997, Kar, 2005, and Lung, 1983). However, industry is increasingly using tools like AVL Boost (Hota and Munjal, 2008) and GT Power (Knutsson, 2005) to identify both the source strength and impedance for each cylinder. With that information in hand, analysts can develop models for complete exhaust systems even including multiple source strengths and source impedances. In light of that, there is a need to define suitable metrics for multiple inlet and outlet intake and exhaust systems.

For the single inlet and outlet case, transmission and insertion loss are the metrics that have been primarily used. Transmission loss is defined as the difference between the incident and transmitted power. It is a property of the exhaust system itself and does not depend on the source strength, or the source and termination impedances below the plane wave cutoff frequency for the intake and exhaust ducts. Finding transmission loss is straightforward using simulation because ideal boundary conditions can be applied easily. However, multiple acoustic load (To, 1979, To, 1979 and Lung, 1983) or source (Munjal, 1990) methods are used for measurement.

Insertion loss is defined as the difference in outlet sound pressure (or power) with and without the muffler or silencer in place (Ver, 2006). It can be directly measured but is difficult to simulate. Insertion loss is dependent on the source and termination impedances. Source impedance is challenging to measure though it is nowadays simulated using commercial 1D CFD packages like AVL Boost and GT Power.

In the field, insertion loss is the more practical metric to assess muffler performance. The sound pressure in dB at the outlet is simply measured with and without the muffler or silencer in place. It is notable that transmission loss will be equivalent to insertion loss if the source and termination impedances are anechoic.

Though the single inlet case is well understood, there have only been a few efforts aimed at defining suitable metrics for the multiple inlet case. Selamet and Ji (Selamet and Ji, 2000 [1]) investigated the transmission loss of circular expansion chambers for the easier multiple outlet case using a mode-matching approach. Later on, they investigated expansion chambers with two inlets and one outlet using a one-dimensional analytical approach and the boundary element method (Selamet and Ji, 2000 [2]). Denia et al. extended this work to elliptical mufflers with two outlets (Denia, 2003). In each of these studies, equations were developed for a specific muffler configuration. Accordingly, the equations developed, though convenient for certain configurations, were not easily extended to the general multiple inlet case and complicated geometries.

It seems that the most relevant work is by Jiang (2005) and similar work by Mimani and Munjal (2012). In both papers, an impedance matrix approach was used to define and evaluate transmission loss. Mimani and Munjal (2012) also developed expressions for insertion loss and noise reduction. Jiang et al. (2005) determined the impedance matrix using the boundary element method. Mimani and Munjal (2012) used a plane wave analysis approach to determine the impedance matrix. In both papers, it was noted that the transmission loss depended on the amplitude and phase relationship between the sources. A complex ratio of the incident sound pressure between each of the inlets was defined in order to calculate transmission loss.

In this work, the transmission and insertion loss definitions are extended to the multiple inlet case. First, the insertion loss is determined for the two-inlet case using the impedance matrix method. Insertion loss is calculated differently than by Mimani and Munjal (2012). Then, both the transmission and insertion loss are

determined using a superposition approach. The superposition approach is simpler to apply for cases having more than two inlets and can also be applied experimentally. The approach is demonstrated both using simulation and experiment.

7.2 Transmission Loss of Two-Inlet Mufflers

Transfer matrices (Munjal, 1987) are commonly used to describe the acoustic performance of single inlet/outlet mufflers assuming plane wave propagation. They relate the sound pressure (p) and particle velocity (v) on one side to the other side of the muffler. For convenience, Jiang et al. (Jiang, 2000) defined an impedance matrix which related the sound pressure at the inlets and outlets to the particle velocity. An impedance matrix approach is particularly convenient for the multiple inlet and outlet case and for use with numerical simulation procedures like the boundary and finite element methods.

7.2.1 Impedance Matrix Method for Transmission Loss

The development below follows Jiang's work (Jiang, 2000). For a muffler having two inlets and one outlet as shown in Figure 7.1, the impedance matrix is defined as

$$\begin{pmatrix} p_1 \\ p_2 \\ p_3 \end{pmatrix} = \begin{bmatrix} z_{11} & z_{12} & z_{13} \\ z_{21} & z_{22} & z_{23} \\ z_{31} & z_{32} & z_{33} \end{bmatrix} \begin{pmatrix} v_1 \\ v_2 \\ v_3 \end{pmatrix} \tag{7.1}$$

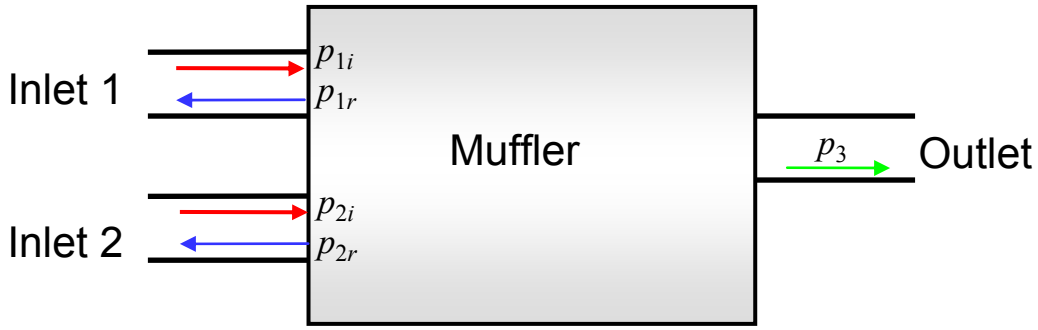

Figure 7.1 Two-inlet and one-outlet muffler.

where subscripts 1, 2 and 3 denote the first inlet, second inlet and outlet locations respectively. In each inlet duct, the sound wave can be decomposed as an incident (p_{1i} or p_{2i}) or a reflected wave (p_{1r} or p_{2r}). At the outlet (p_3), there is no reflected wave because an anechoic termination is assumed.

The impedance matrix can be obtained using the boundary element method (BEM) by setting a velocity boundary condition, v=1, alternately at locations 1, 2, and 3. For example, the first column of the matrix is obtained by setting v_1=1, v_2=v_3=0. Although three different BEM runs are needed to create the impedance matrix, they share the same BEM matrix, which need only be solved once. The three different boundary condition sets correspond to three trivial back substitutions.

In a nearly identical manner, the impedance matrix can be obtained from three 2×2 transfer matrices. Transfer matrices are defined between each pair of ports with the one port blocked (v=0). For example, the transfer matrix between ports 1 and 2 can be expressed as

$$\begin{Bmatrix} p_1 \\ v_1 \end{Bmatrix} = \begin{bmatrix} A_{12}^b & B_{12}^b \\ C_{12}^b & D_{12}^b \end{bmatrix} \begin{Bmatrix} p_2 \\ v_2 \end{Bmatrix} \tag{7.2}$$

where A_{12}^b, B_{12}^b, C_{12}^b, and D_{12}^b are the four pole parameters relating ports 1 and 2 with port 3 blocked. Similar equations can be written relating ports 1 and 3 (with port 2 blocked) as

$$\begin{Bmatrix} p_1 \\ v_1 \end{Bmatrix} = \begin{bmatrix} A_{13}^b & B_{13}^b \\ C_{13}^b & D_{13}^b \end{bmatrix} \begin{Bmatrix} p_3 \\ v_3 \end{Bmatrix} \tag{7.3}$$

and relating ports 2 and 3 (with port 1 blocked) as

$$\begin{Bmatrix} p_2 \\ v_2 \end{Bmatrix} = \begin{bmatrix} A_{23}^b & B_{23}^b \\ C_{23}^b & D_{23}^b \end{bmatrix} \begin{Bmatrix} p_3 \\ v_3 \end{Bmatrix} \tag{7.4}$$

Using Equations (7.2)-(7.4), the impedance matrix defined in Equation (7.1) can be determined by alternately setting one velocity (v_1, v_2, v_3) equal to 1 with the other two velocities set to 0. Then, Equation (7.1) can be re-written as

$$\begin{pmatrix} p_1 \\ p_2 \\ p_3 \end{pmatrix} = \begin{bmatrix} \dfrac{A_{13}^b}{C_{13}^b} & -B_{12}^b + \dfrac{A_{12}^b D_{12}^b}{C_{12}^b} & B_{13}^b - \dfrac{A_{13}^b D_{13}^b}{C_{13}^b} \\ \dfrac{1}{C_{12}^b} & \dfrac{A_{23}^b}{C_{23}^b} & B_{23}^b - \dfrac{A_{23}^b D_{23}^b}{C_{23}^b} \\ \dfrac{1}{C_{13}^b} & \dfrac{1}{C_{23}^b} & \dfrac{D_{13}^b}{C_{13}^b} \end{bmatrix} \begin{pmatrix} v_1 \\ v_2 \\ v_3 \end{pmatrix} \tag{7.5}$$

The sound pressure at any point inside an inlet tube is composed of an incident wave p_i and a reflected wave p_r. If the convention $e^{+j\omega t}$ is adopted, where ω is the angular frequency, the sound pressure and acoustic particle velocity in each inlet tube can be written as

$$p = p_i + p_r = P_i e^{-jkx} + P_r e^{+jkx} \tag{7.6}$$

$$v = \frac{p_i - p_r}{\rho c} \tag{7.7}$$

where P_i and P_r are the respective complex amplitudes of the incident and reflected waves. k is the wavenumber, ρ is the air density, and c is the speed of sound. If the termination impedance is anechoic, there will be no reflected wave

in the termination and $p_3 = p_{3i}$ where p_{3i} is the transmitted wave. Equation (7.1) becomes

$$\begin{pmatrix} p_{1i} + p_{1r} \\ p_{2i} + p_{2r} \\ p_3 \end{pmatrix} = \begin{bmatrix} \frac{z_{11}}{\rho c} & \frac{z_{12}}{\rho c} & \frac{z_{13}}{\rho c} \\ \frac{z_{21}}{\rho c} & \frac{z_{22}}{\rho c} & \frac{z_{23}}{\rho c} \\ \frac{z_{31}}{\rho c} & \frac{z_{32}}{\rho c} & \frac{z_{33}}{\rho c} \end{bmatrix} \begin{pmatrix} p_{1i} - p_{1r} \\ p_{2i} - p_{2r} \\ p_3 \end{pmatrix} \tag{7.8}$$

Adding p_{1i}-p_{1r} to both sides of the first equation and p_{2i}-p_{2r} to the second equation, yields

$$\begin{pmatrix} 2p_{1i} \\ 2p_{2i} \\ 2p_3 \end{pmatrix} = \begin{bmatrix} \frac{z_{11}}{\rho c} + 1 & \frac{z_{12}}{\rho c} & \frac{z_{13}}{\rho c} \\ \frac{z_{21}}{\rho c} & \frac{z_{22}}{\rho c} + 1 & \frac{z_{23}}{\rho c} \\ \frac{z_{31}}{\rho c} & \frac{z_{32}}{\rho c} & \frac{z_{33}}{\rho c} \end{bmatrix} \begin{pmatrix} p_{1i} - p_{1r} \\ p_{2i} - p_{2r} \\ p_3 \end{pmatrix} \tag{7.9}$$

For simplicity of notation, the above 3x3 matrix is denoted [A] and its components by a_{ij}.

Define a complex ratio α between the two incident sound pressures.

$$\alpha = \frac{p_{2i}}{p_{1i}} \tag{7.10}$$

Substitute Equation (7.10) into Equation (7.9), and divide both sides of the equations by p_3. It can be rearranged as

$$\begin{bmatrix} -2 & a_{11} & a_{12} \\ -2\alpha & a_{21} & a_{22} \\ 0 & a_{31} & a_{32} \end{bmatrix} \begin{pmatrix} \dfrac{p_{1i}}{p_3} \\ \dfrac{p_{1i}-p_{1r}}{p_3} \\ \dfrac{p_{2i}-p_{2r}}{p_3} \end{pmatrix} = \begin{pmatrix} -a_{13} \\ -a_{23} \\ 1-a_{33} \end{pmatrix} \tag{7.11}$$

By solving Equation (7.11),

$$\frac{p_{1i}}{p_3} = \frac{\begin{vmatrix} -a_{13} & a_{11} & a_{12} \\ -a_{23} & a_{21} & a_{22} \\ 1-a_{33} & a_{31} & a_{32} \end{vmatrix}}{\begin{vmatrix} -2 & a_{11} & a_{12} \\ -2\alpha & a_{21} & a_{22} \\ 0 & a_{31} & a_{32} \end{vmatrix}} \tag{7.12}$$

The transmission loss of the muffler can be expressed as

$$\begin{aligned} TL &= 10\log\frac{w_{1i}+w_{2i}}{w_3} = 10\log\frac{|p_{1i}|^2 S_1 + |p_{2i}|^2 S_2}{|p_3|^2 S_3} \\ &= 20\log\left|\frac{p_{1i}}{p_3}\right| + 10\log\frac{S_1 + |\alpha|^2 S_2}{S_3} \end{aligned} \tag{7.13}$$

where S_n is the cross-sectional area of duct n.

The complex ratio α represents the relationship between the two incident waves. However, it should be pointed out that this ratio cannot be easily predetermined, because the two incident waves are not independent.

With that qualification in mind, the sound pressure of each incident wave can be easily related to the source pressure if the source impedances are anechoic. The source impedance is defined as

$$z_{sn} = \frac{p_{sn} - p_n}{v_n} \tag{7.14}$$

where n indicates source n. By inserting Equations (7.6) and (7.7) into Equation (7.14) and assuming that the sources are anechoic, it can be seen that

$$p_{sn} = 2p_{ni} \tag{7.15}$$

Thus, the ratio between incident waves is equal to the ratio of the source strengths. According to this definition of transmission loss, the ratio between sources will significantly affect the transmission loss. In absence of information about the source, the ratio for α must be assumed.

7.2.2 Transfer Matrix Superposition Method for Transmission Loss

By applying the superposition principle, the sound pressure p_3 at the downstream tube can be divided into two separate contributions as shown in Figure 7.2. One, noted as ${p_3}^{1i}$, is the sound pressure contributed by the incident sound pressure wave at inlet 1 assuming that inlet 2 is anechoic and the source pressure is 0 ($p_{s2} = 0$). The other component, noted as ${p_3}^{2i}$ results from the incident wave at the second inlet tube p_2 assuming that inlet 1 is anechoic and $p_{s1} = 0$.

For each component, the two-inlet, one-outlet muffler system can be reduced to a one-inlet and one-outlet system, which can be described using a transfer matrix. The transfer matrix can be obtained using either numerical simulation, such as the boundary element or finite element method, or 1-D plane wave simulation (Munjal, 1987).

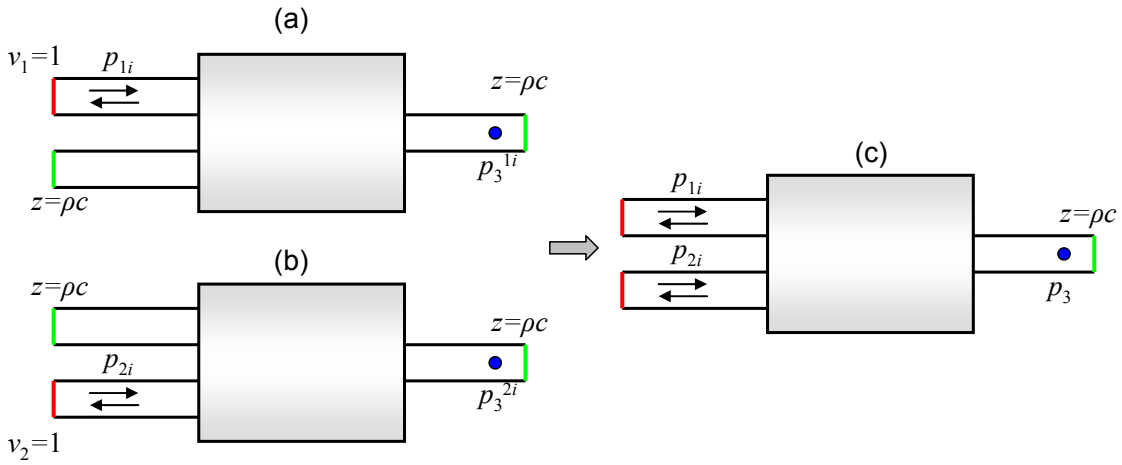

Figure 7.2 Superposition for transmission loss of two-inlet muffler.

For the first component as shown in Figure 7.2(a), the transfer matrix relating inlet 1 to the outlet is

$$\begin{pmatrix} p_1 \\ v_1 \end{pmatrix} = \begin{bmatrix} A_{13}^{an} & B_{13}^{an} \\ C_{13}^{an} & D_{13}^{an} \end{bmatrix} \begin{pmatrix} p_3^{1i} \\ v_3^{1i} \end{pmatrix} \tag{7.16}$$

where the 2×2 matrix is the transfer matrix from inlet 1 to the outlet with source 2 assumed to be anechoic.

By applying wave decomposition at the first inlet, Equation (7.16) can be re-written as

$$\begin{pmatrix} p_{1i} + p_{1r} \\ \dfrac{p_{1i} - p_{1r}}{\rho c} \end{pmatrix} = \begin{bmatrix} A_{13}^{an} & B_{13}^{an} \\ C_{13}^{an} & D_{13}^{an} \end{bmatrix} \begin{pmatrix} p_3^{1i} \\ \dfrac{p_3^{1i}}{\rho c} \end{pmatrix} \tag{7.17}$$

The transfer function H_{13} between the sound pressure at the outlet contributed by the first inlet, and the incident pressure at the first inlet can be expressed as

$$H_{13} = \frac{p_3^{1i}}{p_{1i}} = \frac{2}{A_{13}^{an} + \frac{B_{13}^{an}}{\rho c} + C_{13}^{an}\rho c + D_{13}^{an}} \tag{7.18}$$

where A_{13}^{an}, B_{13}^{an}, C_{13}^{an} and D_{13}^{an} are the four-pole parameters between the first inlet and the outlet with the second inlet anechoic as shown in Figure 7.2(a). Similarly, the transfer function H_{23} between the sound pressure at the outlet contributed by the second inlet, and the incident pressure at the second inlet can be expressed as

$$H_{23} = \frac{p_3^{2i}}{p_{2i}} = \frac{2}{A_{23}^{an} + \frac{B_{23}^{an}}{\rho c} + C_{23}^{an}\rho c + D_{23}^{an}} \tag{7.19}$$

where A_{23}^{an}, B_{23}^{an}, C_{23}^{an} and D_{23}^{an} are the four-pole parameters between the second inlet and the outlet with the first inlet anechoic as shown in Figure 7.2(b).

The transmission loss of muffler is defined as the sound power level difference between the incident power and the transmitted power. For the two-inlet one outlet muffler, the incident power is the summation of the power from both incident waves. The transmitted power is determined by the wave in the outlet tube. The transmission loss can be defined as

$$TL = 10\log_{10}\frac{|p_{1i}|^2 S_1 + |p_{2i}|^2 S_2}{|p_3|^2 S_3} \tag{7.20}$$

The transmission loss can be written as

$$TL = 10\log_{10}\frac{|p_{1i}|^2 S_1 + |p_{2i}|^2 S_2}{|p_{1i}H_{13} + p_{2i}H_{23}|^2 S_3} \tag{7.21}$$

By using the complex ratio (α) between the two incident sound pressures (Equation (7.10)), the transmission loss of the muffler can be expressed as

$$TL = 10\log_{10}\frac{S_1 + |\alpha|^2 S_2}{|H_{13} + \alpha H_{23}|^2 S_3} \tag{7.22}$$

7.2.3 Transmission Loss Example

A two-inlet simple expansion chamber system was used to validate the superposition method discussed above. The dimensions are shown in Figure 7.3. The length and the diameter of the expansion chamber are 0.5 m and 0.31 m respectively. The diameters of the two-inlets are 0.03 m and 0.04 m, and the diameter for the outlet is 0.05 m.

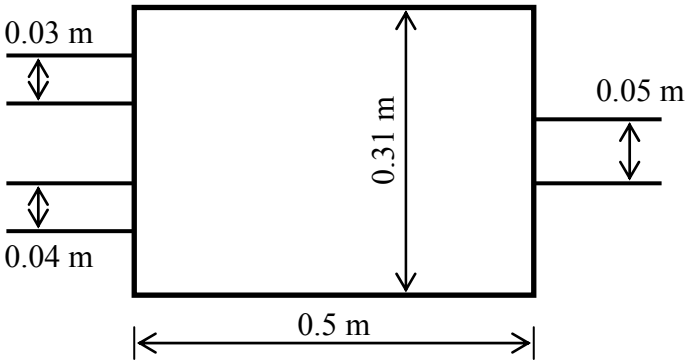

Figure 7.3 Dimensions of a two-inlet muffler.

Figure 7.4 compares the calculated transmission loss in the case where the two incident waves are equal in power and are coherent (α=1) using both the impedance matrix method and the superposition method. For the 1-D impedance matrix and 1-D superposition cases, the impedance matrix and transfer matrices are obtained using plane wave theory. For the two 3-D cases, the impedance matrix and transfer matrices are obtained using boundary element simulation. All the four results agree well with each other below the plane wave cutoff frequency. And the two 3-D results agree well above cutoff frequency.

When a 180° phase difference occurs between the two incident waves (α=-1), results below plane wave cutoff are compared with the 0° case in Figure 7.5. Notice that the muffler transmission loss can be improved by taking the phase difference between the two incident waves into consideration.

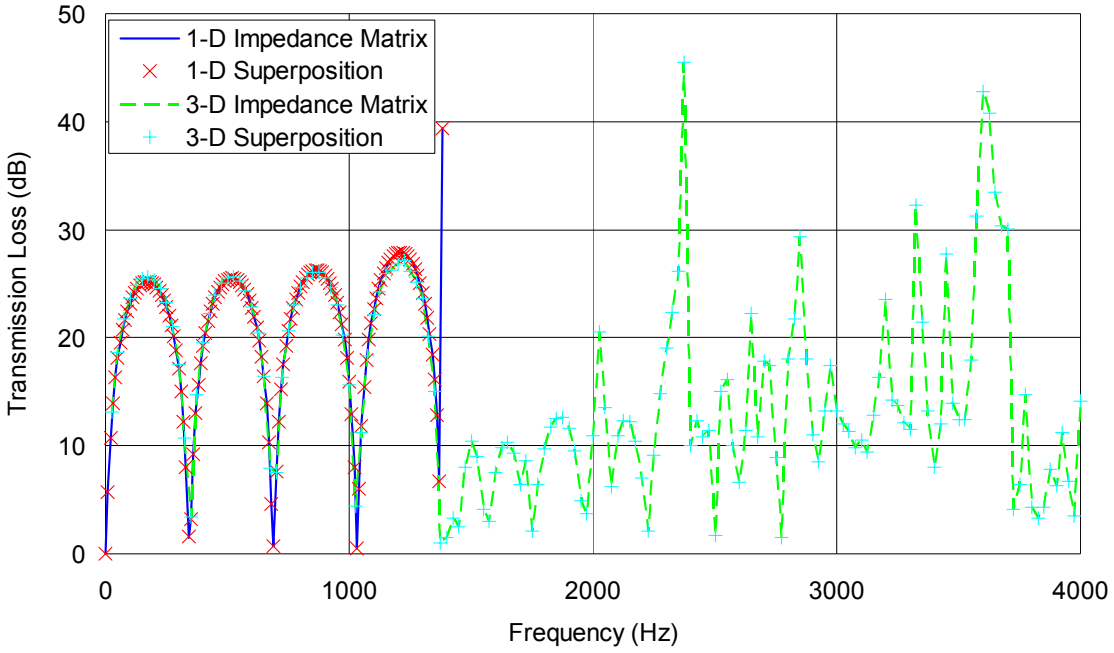

Figure 7.4 Transmission loss using impedance matrix method and pressure superposition method (α=1). Plane wave cutoff is around 1350 Hz.

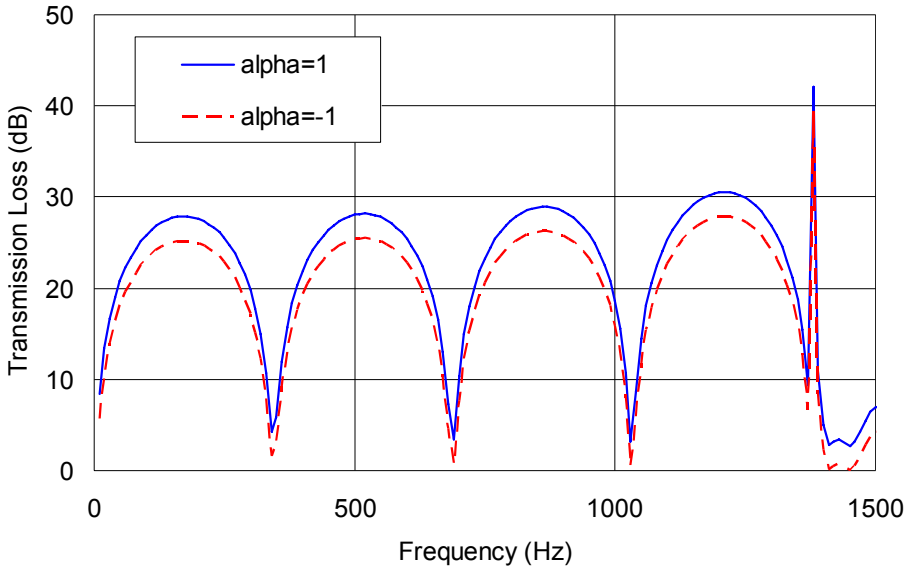

Figure 7.5 Transmission loss with different incident wave ratios (α=1 and α=-1).

The superposition method can be expanded to calculate the transmission loss of multi-inlet and one-outlet muffler systems. In that case, the transmission loss of n-inlet mufflers can be obtained via

$$TL = 10\log_{10}\frac{S_1 + |\alpha_2|^2 S_2 + \ldots + |\alpha_n|^2 S_n}{|H_{1o} + \alpha_2 H_{2o} + \ldots + \alpha_n H_{no}|^2 S_o} \tag{7.23}$$

where S_i is the cross-sectional area of the corresponding duct. α_i is the complex ratio between the incident wave in the n^{th} inlet and the incident wave in the 1st inlet. H_{no} is the sound pressure ratio between the sound pressure at the outlet contributed by the n^{th} incident pressure and the n^{th} incident pressure.

For traditional one-inlet and one-outlet mufflers, the transmission loss is a property of the muffler itself and is not affected by the source, if the flow and temperature gradient are ignored. However, the transmission loss for multi-inlet mufflers may be affected by the sources as well as the muffler, as shown in

Figure 7.4, which indicates that insertion loss could be a better evaluation metric for multi-inlet mufflers.

7.3 Insertion Loss of Two-Inlet Mufflers

Insertion loss is the metric used to assess muffler performance in the field. It is defined as the difference in sound pressure or sound power level at the termination with and without a muffler or silencer installed. A two-inlet muffler with two sources and a termination is shown in Figure 7.6. Assume the two sources have source strengths p_{s1} and p_{s2}, and source impedances z_{s1} and z_{s2}.

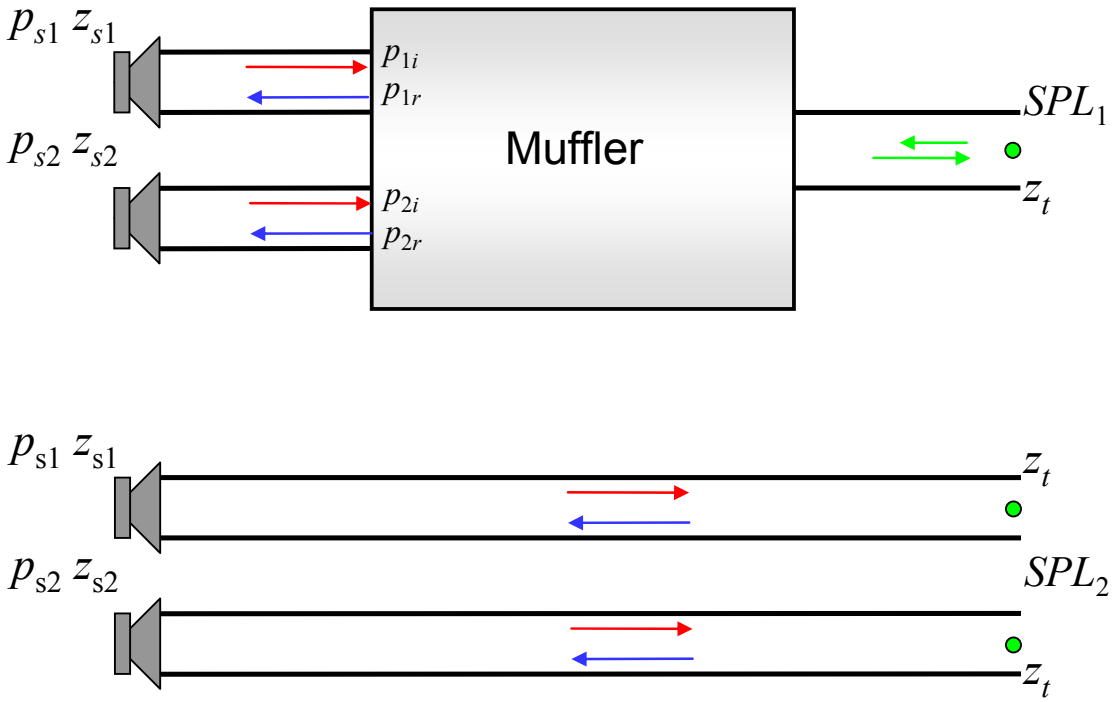

Figure 7.6 Insertion loss for two-inlet and one-outlet muffler.

7.3.1 Impedance Matrix Method for Insertion Loss

The impedance matrix approach can be extended to calculate the insertion loss for a two-inlet muffler. According to Bodén and Åbom (1995), the outgoing wave from the source (p_{s+}) can be calculated via

$$p_{s+} = p_s\left(\frac{1-R_s}{2}\right) \tag{7.24}$$

where p_s is the source strength and R_s is the source reflection coefficient. The reflection coefficient can be related to the source impedance by

$$z_s = \frac{1+R_s}{1-R_s} \tag{7.25}$$

The incident wave (p_i) in the tube consists of the outgoing wave from the source and the reflected wave from the source boundary ($p_r \cdot R_s$) as shown in Figure 7.7. By applying wave decomposition to each inlet duct, Equation (7.1) can be written as

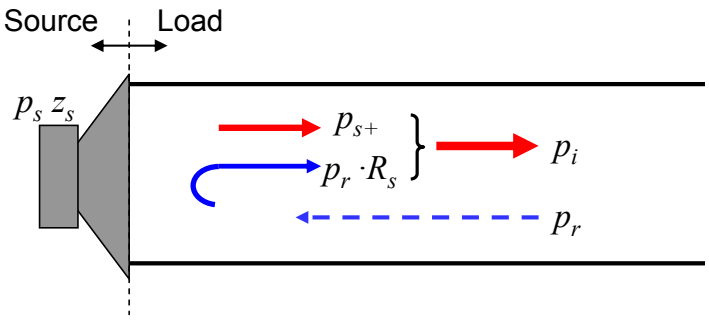

Figure 7.7 Wave decomposition at the source side with source impedance and source strength.

$$\begin{pmatrix} p_{s1}\dfrac{1-R_{s1}}{2}+R_{s1}p_{r1}+p_{r1} \\ p_{s2}\dfrac{1-R_{s2}}{2}+R_{s2}p_{r2}+p_{r2} \\ p_3 \end{pmatrix} = \frac{1}{\rho c}\begin{bmatrix} z_{11} & z_{12} & z_{13} \\ z_{21} & z_{22} & z_{23} \\ z_{31} & z_{32} & z_{33} \end{bmatrix} \begin{pmatrix} p_{s1}\dfrac{1-R_{s1}}{2}+R_{s1}p_{r1}-p_{r1} \\ p_{s2}\dfrac{1-R_{s2}}{2}+R_{s2}p_{r2}-p_{r2} \\ \dfrac{\rho c p_3}{z_t} \end{pmatrix} \quad (7.26)$$

Defining a complex ratio β between the two source strengths,

$$\beta = \frac{p_{s2}}{p_{s1}} \quad (7.27)$$

and dividing Equation (7.26) by p_3, the equation can be re-arranged as

$$[C]\begin{pmatrix} \dfrac{p_{s1}}{p_3} \\ \dfrac{p_{r1}}{p_3} \\ \dfrac{p_{r2}}{p_3} \end{pmatrix} = [B] \quad (7.28)$$

Where

$$[C] = \begin{bmatrix} \left(\dfrac{1-R_{s1}}{2}\right)\left(1-\dfrac{z_{11}}{\rho c}\right)-\beta\dfrac{z_{12}}{\rho c}\left(\dfrac{1-R_{s2}}{2}\right) & (R_{s1}+1)-\dfrac{z_{11}}{\rho c}(R_{s1}-1) & -\dfrac{z_{12}}{\rho c}(R_{s2}-1) \\ \beta\left(\dfrac{1-R_{s2}}{2}\right)\left(1-\dfrac{z_{22}}{\rho c}\right)-\dfrac{z_{21}}{\rho c}\left(\dfrac{1-R_{s1}}{2}\right) & -\dfrac{z_{21}}{\rho c}(R_{s1}-1) & (R_{s2}+1)-\dfrac{z_{22}}{\rho c}(R_{s2}-1) \\ -\dfrac{z_{31}}{\rho c}\left(\dfrac{1-R_{s1}}{2}\right)-\beta\dfrac{z_{32}}{\rho c}\left(\dfrac{1-R_{s2}}{2}\right) & -\dfrac{z_{31}}{\rho c}(R_{s1}-1) & -\dfrac{z_{32}}{\rho c}(R_{s2}-1) \end{bmatrix} \quad (7.29)$$

and

$$[B]=\begin{pmatrix} \frac{z_{13}}{z_t} \\ \frac{z_{23}}{z_t} \\ \frac{z_{33}}{z_t}-1 \end{pmatrix} \tag{7.30}$$

Solve Equation (7.28) and define τ as the ratio between the first source strength and the sound pressure at the termination,

$$\tau=\frac{p_{s1}}{p_3}=\frac{\begin{vmatrix} b_1 & c_{12} & c_{13} \\ b_2 & c_{22} & c_{23} \\ b_3 & c_{32} & c_{33} \end{vmatrix}}{\begin{vmatrix} c_{11} & c_{12} & c_{13} \\ c_{21} & c_{22} & c_{23} \\ c_{31} & c_{32} & c_{33} \end{vmatrix}} \tag{7.31}$$

where b_i and c_{ij} are corresponding elements of matrices [B] and [C]. Both b_i and c_{ij} are functions of the impedance matrix terms and can be determined for any given muffler geometry.

Replacing the muffler with two straight ducts having the same length, as shown in Figure 7.6, the sound pressure at the termination of the ducts can also be related to the source strength using transfer matrix theory. The transfer matrix for a straight duct can be expressed as (Munjal, 1987)

$$T=\begin{bmatrix} \cos(kl) & i\rho c\sin(kl) \\ \frac{i}{\rho c}\sin(kl) & \cos(kl) \end{bmatrix} \tag{7.32}$$

where l is the length of the both ducts. The ratio (τ_1) between the first source strength (p_{s1}) and the sound pressure at the termination (p_{d1}) of the first straight duct and can be calculated using

$$\tau_1 = \frac{p_{s1}}{p_{d1}} = \frac{T_{11}z_t + T_{12} + T_{21}z_{s1}z_t + T_{22}z_{s1}}{z_t} \tag{7.33}$$

where T_{ij} are the terms in matrix [T]. Similarly, the ratio (τ_2) between p_{s1} and p_{d2} can be calculated using

$$\tau_2 = \frac{p_{s1}}{p_{d2}} = \frac{T_{11}z_t + T_{12} + T_{21}z_{s2}z_t + T_{22}z_{s2}}{\beta z_t} \tag{7.34}$$

Then, the insertion loss of the muffler can be obtained via

$$IL = 10\log\frac{|p_{d1}|^2 S_1 + |p_{d2}|^2 S_2}{|p_3|^2 S_3} \tag{7.35}$$

By substituting τ_1 and τ_2 from Equations (7.33) and (7.34), the insertion loss can be simplified as

$$IL = 10\log\frac{\left|\frac{p_{s1}}{\tau_1}\right|^2 S_1 + \left|\frac{p_{s1}}{\tau_2}\right|^2 S_2}{\left|\frac{p_{s1}}{\tau}\right|^2 S_3} = 10\log\frac{\left|\frac{1}{\tau_1^2}\right| S_1 + \left|\frac{1}{\tau_2^2}\right| S_2}{\left|\frac{1}{\tau^2}\right| S_3} \tag{7.36}$$

7.3.2 Superposition Method for Insertion Loss

Similarly, the insertion loss can be determined by superimposing the contributions from each inlet or source as shown in Figure 7.8.

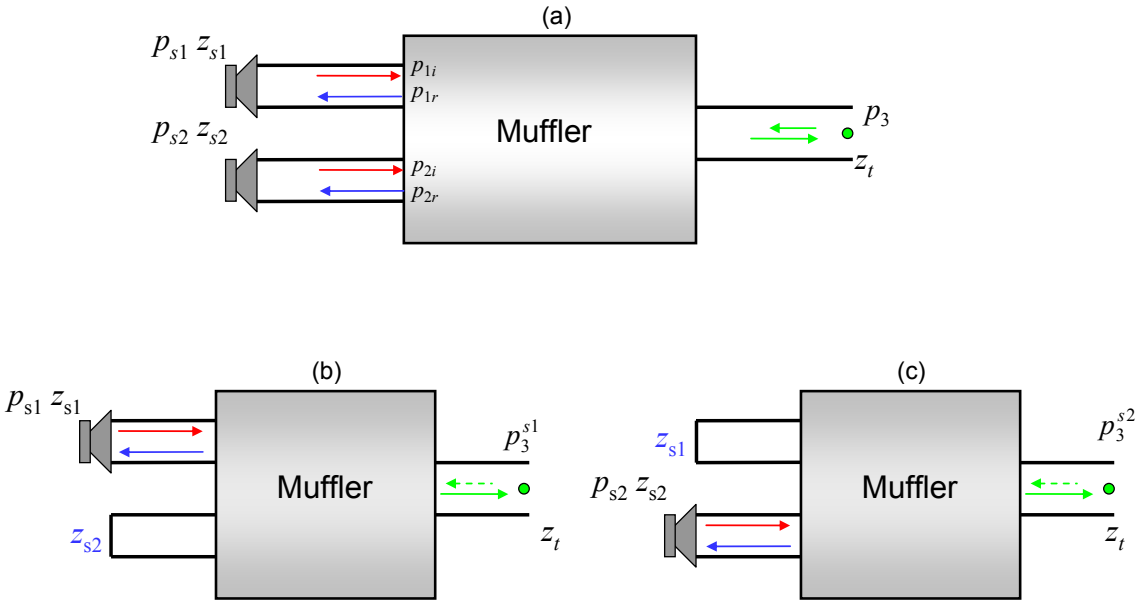

Figure 7.8 Superposition for insertion loss of two-inlet muffler.

The first source contribution can be determined by assuming the second source is passive. Thus, the source pressure of the second source is zero but the source impedance remains as indicated in Figure 7.8(b). The system can then be considered as a one-inlet and one-outlet muffler and the transfer matrix of the reduced system can be obtained using either numerical simulation or plane wave theory. The sound pressure at the termination contributed by the first source is

$$p_3^{s1} = \frac{p_{s1} z_t}{A_{13}^p z_t + B_{13}^p + C_{13}^p z_{s1} z_t + D_{13}^p z_{s1}} \tag{7.37}$$

where A_{13}^p, B_{13}^p, C_{13}^p, and D_{13}^p are the four-pole parameters relating source 1 to the outlet assuming that source 2 is passive. Similarly, the sound pressure at the termination contributed by the second source can be calculated as

$$p_3^{s2} = \frac{p_{s2} z_t}{A_{23}^p z_t + B_{23}^p + C_{23}^p z_{s2} z_t + D_{23}^p z_{s2}} \tag{7.38}$$

where A_{23}^p, B_{23}^p, C_{23}^p, and D_{23}^p are the four-pole parameters of source 2 to the outlet as shown in Figure 7.8(c). The total sound pressure at the termination is the summation of these two contributions and can be expressed as

$$p_3 = p_3^{s1} + p_3^{s2} \tag{7.39}$$

The sound pressure for straight ducts can be calculated using Equations (7.33) and (7.34) and the insertion loss can be calculated using Equation (7.30).

This method can conveniently be extended to the n-inlet and one-out muffler. The total pressure at the outlet can be expressed as

$$p_o = \sum_{n=1}^{N} p_o^{sn} \tag{7.40}$$

where $p_o{}^{sn}$ denotes the sound pressure contributed by the nth source with other sources being turned off. It follows that $p_o{}^{sn}$ can be obtained by

$$p_o^{sn} = \frac{p_{sn} z_t}{A_{no}^p z_t + B_{no}^p + C_{no}^p z_{sn} z_t + D_{no}^p z_{sn}} \tag{7.41}$$

where z_{sn} is the source impedance of the n^{th} source. A_{no}^p, B_{no}^p, C_{no}^p, and D_{no}^p are the four-pole parameters from the n^{th} source to the outlet with other sources being turned off.

7.3.3 Experimental Validation of Sound Pressure Superposition

In order to verify the superposition approach, an experiment was carried out as shown in Figure 7.9. Two impedance tubes were connecting to the two inlets of the muffler respectively. The loudspeakers at the entry to both impedance tubes are the sources. Random excitation was used for each loudspeaker. First, the source impedance and source strength of each speaker was measured. A two-load wave decomposition method (Bodén and Åbom, 1995) was applied to

determine the source impedance and the source strength. The source impedance was measured a second time after reducing the excitation by 24 dB and was unaffected by the difference in source amplitude. Figure 7.10 shows the real part of the source impedance with different amplitude of random excitation.

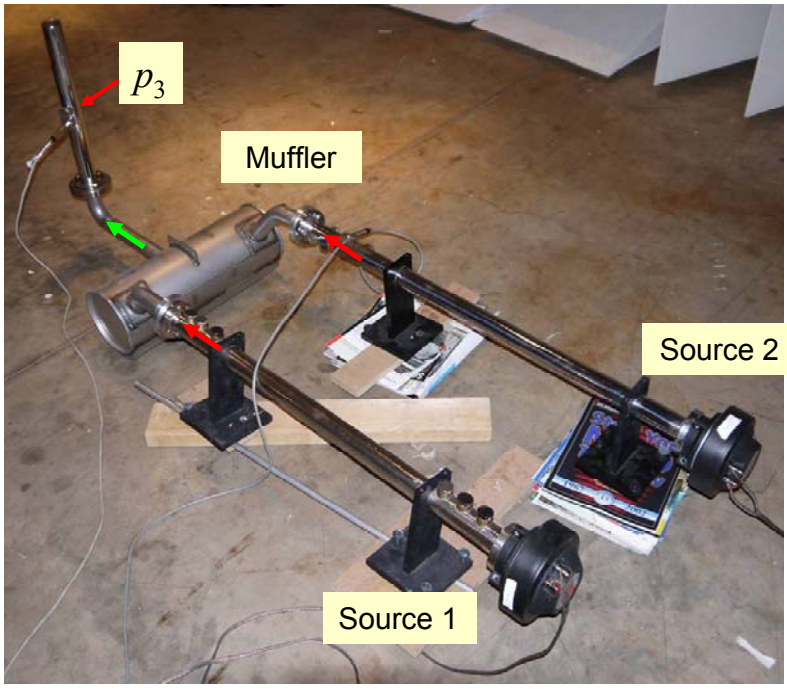

Figure 7.9 Experiment setup for pressure superposition of two-inlet muffler.

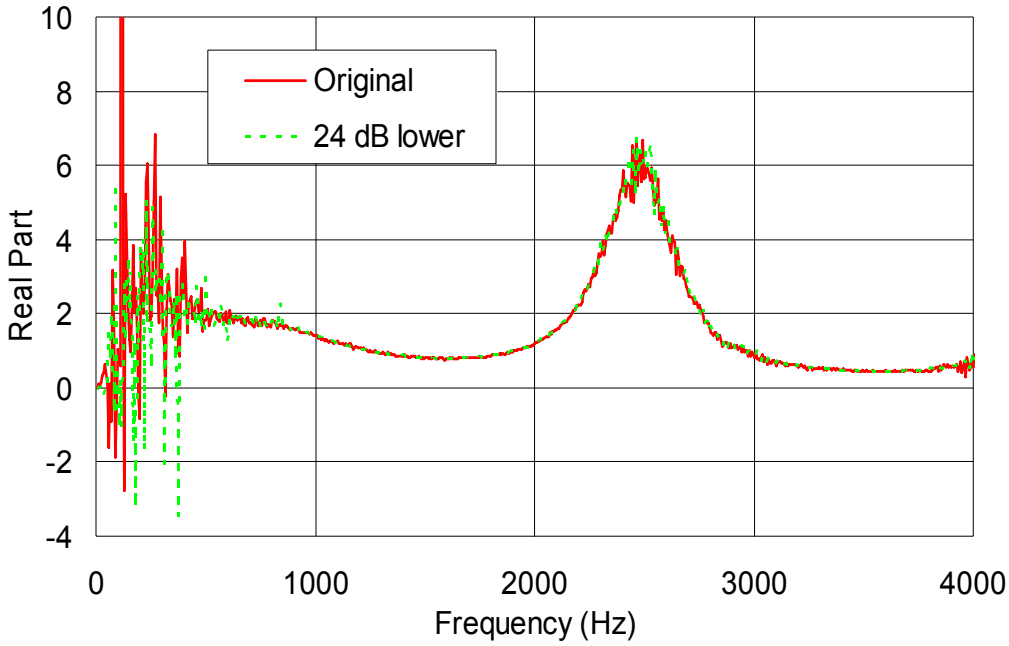

Figure 7.10 Measured source impedance (real part) of two source strength levels.

A third impedance tube was connecting to the outlet of the muffler. The termination impedance at the outlet was measured using the two microphone method (Seybert, 1997 and ASTM, 2009).

The contribution from each source was determined in the following way. In order to determine the contribution from source 1, the amplitude of source 2 was turned down so that its source strength was negligible compared to source 1. Accordingly, source 2 can be considered as passive, but the source impedance of source 2 should be nearly the same as if it were active. The two-load (ASTM, 2009) method was applied to measure the transfer matrix from the first inlet to the termination p_3 as shown in Figure 7.9. By multiplying the transfer matrix of the impedance tube, the transfer matrix from source 1 to the termination was obtained. Repeating the same procedure, the transfer matrix from source 2 to the termination was also obtained by reducing the amplitude of source 1.

After determining the transfer matrices, source strengths, source impedances,

and termination impedance, the sound pressure p_3 was calculated using superposition (Equations (7.37)-(7.39)). For comparison, the sound pressure p_3 was also measured directly with both sources set at the normal level. Results are compared in Figure 7.11. Note that in this measured case, the two source strengths were identical because the two speakers were the same with identical random excitation. Thus, β is equal to 1.

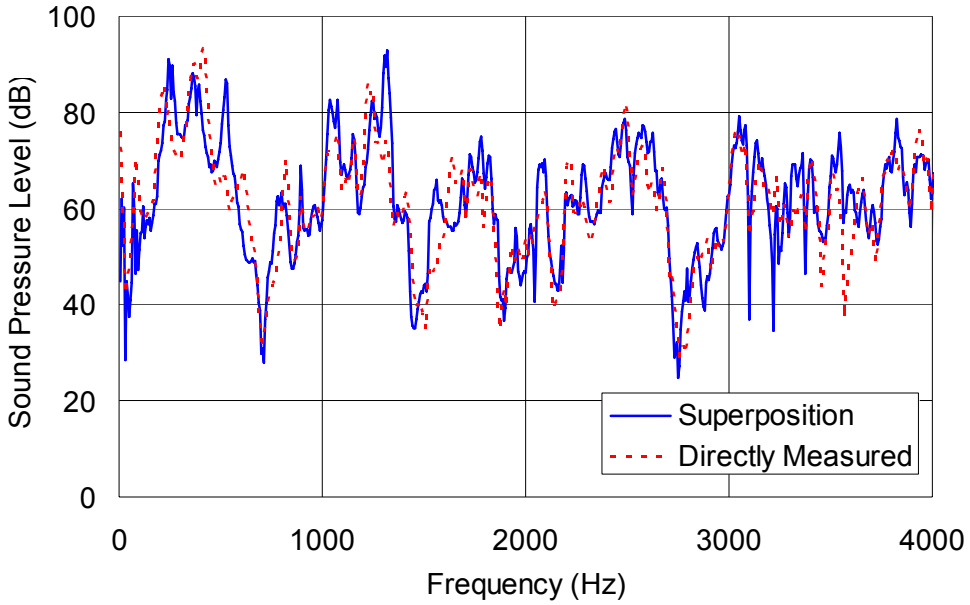

Figure 7.11 Sound pressure levels at the outlet using pressure superposition and direct measurement, when sources are in phase (β=1).

By switching the positive and negative wire connection of one of the two speakers, the two source strengths remained at the same level but were 180° out of phase (β = -1). In this case, the sound pressure p_3 was also calculated and directly measured. The sound pressure is compared in Figure 7.12.

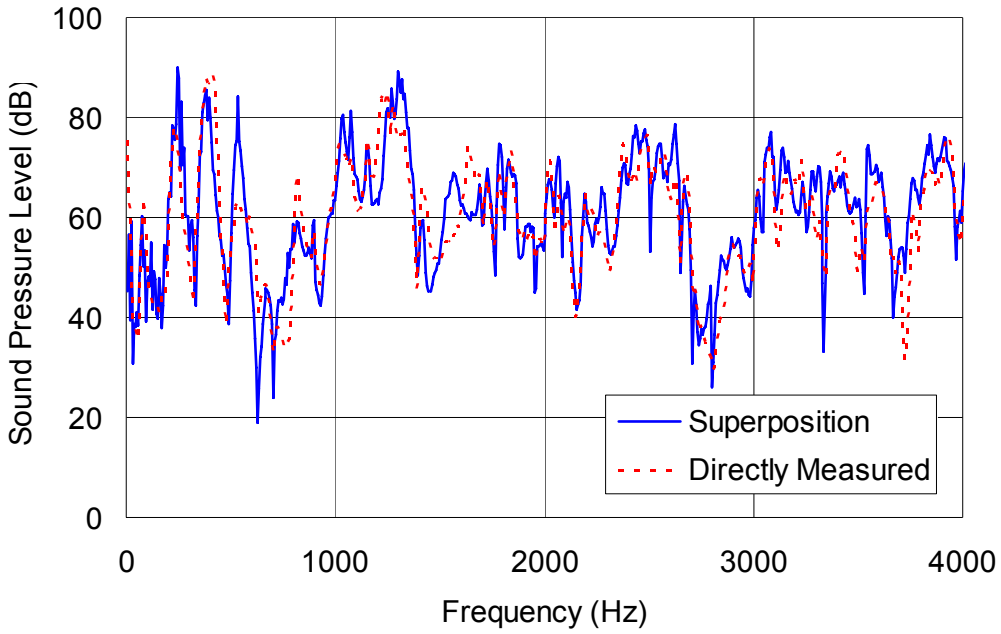

Figure 7.12 Sound pressure levels at the outlet using pressure superposition and direct measurement, when sources are in phase (β=-1).

The sound pressures (p_{d1}, p_{d2}) at the termination of the straight pipes (sans muffler) was calculated using transfer matrix theory (Equation (7.33) and Equation (7.34)) using the source strength, source impedance, and termination impedance. After which, insertion loss of the muffler system was determined using Equation (7.35) as shown in Figure 7.13. Notice that the phase difference between sources can have a substantial effect on the insertion loss especially at low frequencies.

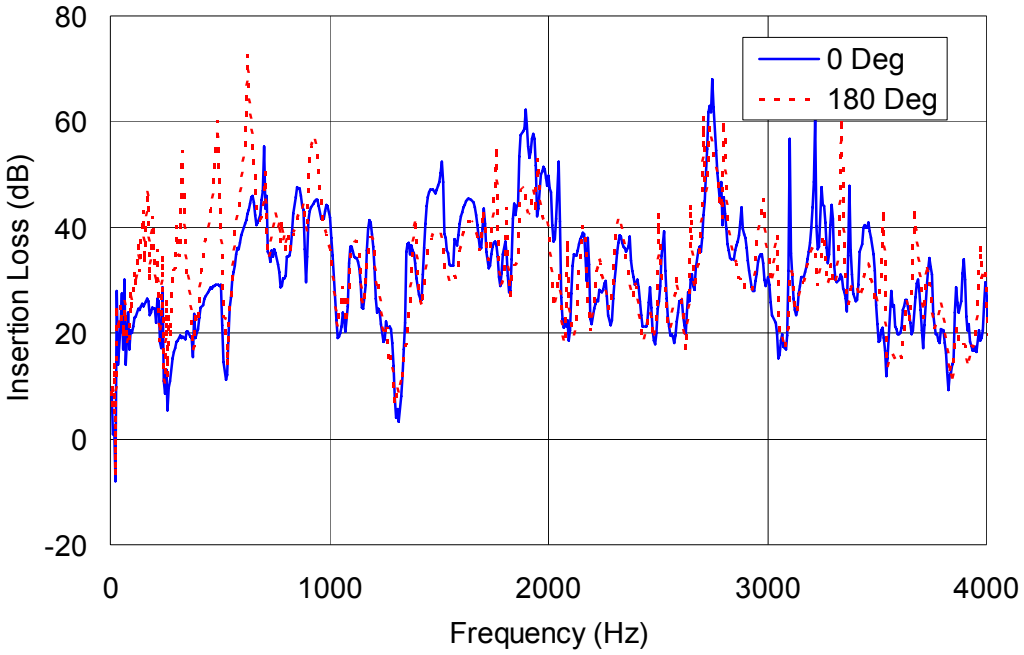

Figure 7.13 Insertion loss comparison with two sources in phase and out of phase.

7.3.4 Results Comparison

A two-inlet simple expansion chamber system, as shown in Figure 7.3, was used to compare the impedance matrix and pressure superposition approaches. The length and diameter of the chamber is 0.5 m and 0.31 m respectively. The diameters of the two-inlets and one outlet are 0.03 m, 0.04 m, and 0.05 m correspondingly. The source impedances of the two sources are (0.2-0.2i) ρc and (0.7-0.7i) ρc, respectively. The termination impedance is (0.3+0.3i) ρc. The ratio between the two source strengths (β) is 1, which indicates a 0° phase difference between the two sources.

The insertion loss for the system described above was calculated using both the impedance matrix and superposition approaches. The results agreed with one another and are shown in Figure 7.14. Two other cases were considered with for the same muffler but with different source strength ratios. β was selected to be i and -1. Figure 7.15 compares the insertion results using different source

strength ratios. The results show that multi-inlet mufflers can be designed to take advantage of the phase difference in between sources.

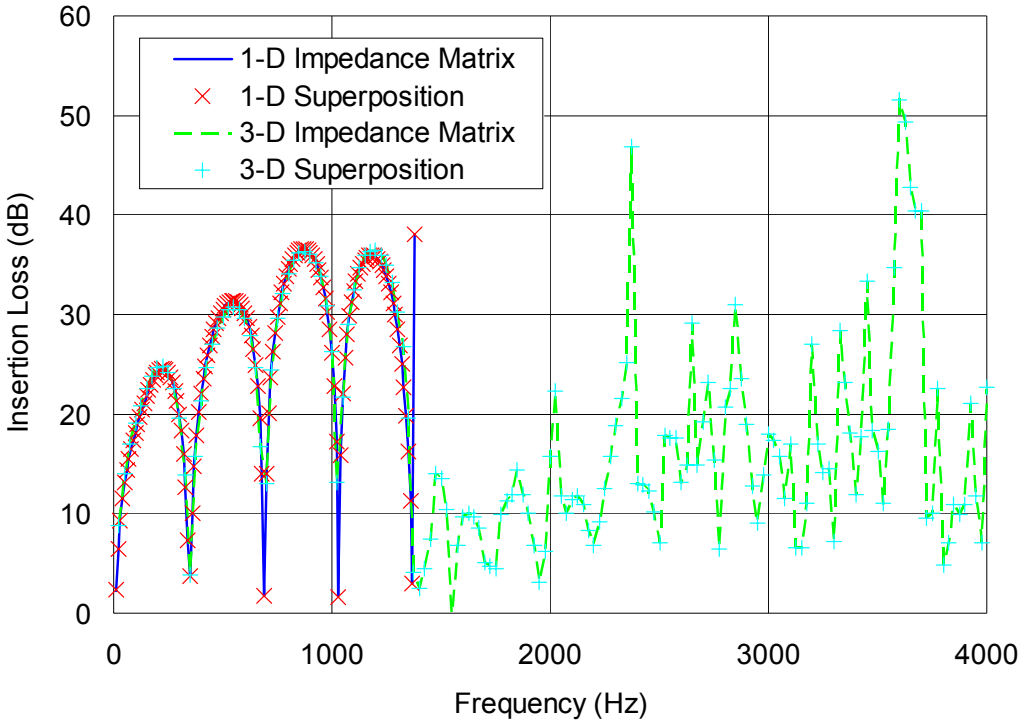

Figure 7.14 Insertion loss comparison using impedance matrix method and pressure superposition method.

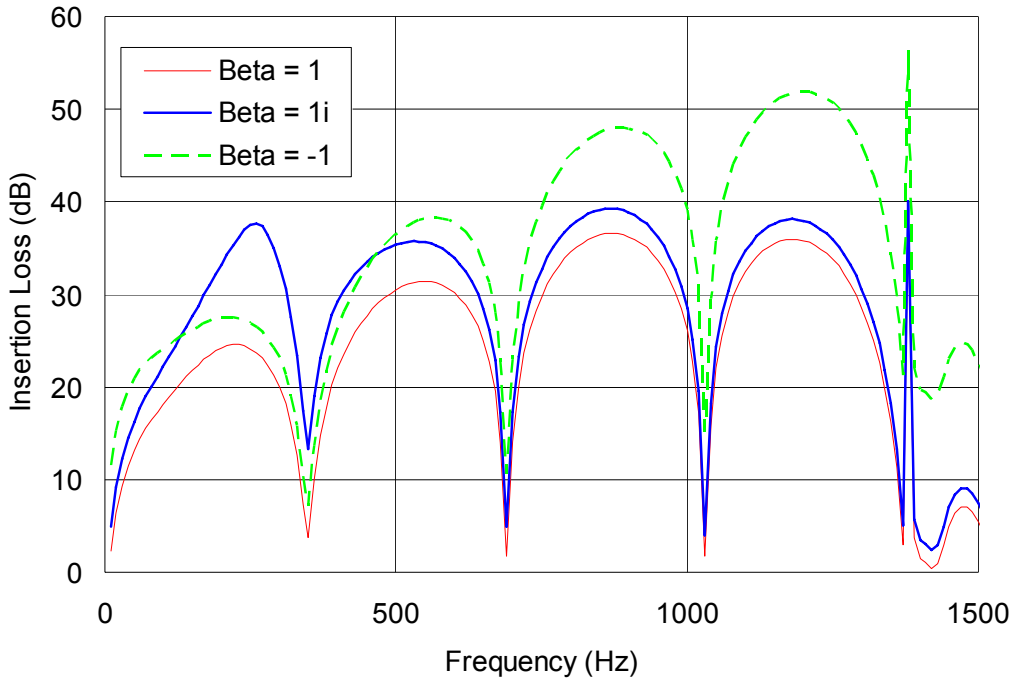

Figure 7.15 Insertion loss comparison with different source strength ratios.

7.4 Methods Comparison and Discussion

Both the impedance matrix and superposition methods can be used to predict two-inlet muffler transmission loss and insertion loss. No approximation is applied in either method.

When applying the impedance matrix method, the impedance matrix of the muffler must first be determined. Though simple to determine using numerical simulation or plane wave theory, the impedance matrix will be difficult to measure. Moreover, transmission or insertion loss involved the solution of a 3x3 matrix (Equation (7.1)). Using measured data, the matrix is not very well conditioned and results are noisy. There are some other practical difficulties with the impedance matrix method. If the number of sources is increased to three, a 4x4 matrix will be required. Accordingly, each additional source increases the size of the matrix and the complexity of the solution.

On the other hand, the superposition method is amenable to both numerical simulation and measurement approaches. The transfer matrix from each inlet to the outlet is first determined assuming that the other inlets are passive. If the muffler has two inlets, two transfer matrices are required. If the muffler has n inlets, n transfer matrices are required. Though the number of measurements increases as inlets are added, the measurements are not difficult to make.

One disadvantage of superposition method is that the solved transfer matrices for insertion loss are directly related to the source impedances. Hence, if any or some of the source impedances are changed, the transfer matrices must be solved or measured again. In addition, the source impedances must be known a priori.

If numerical simulation is used, the impedance matrix method is very convenient for using boundary or finite element simulation. By setting the inlet and outlet boundary conditions as a unit particle velocity, the impedance matrix can be determined after solving the boundary element equations and then using back substitution. On the other hand, the superposition method is convenient if plane wave methods are used. The transfer matrices from each inlet to each outlet can be solved easily as long as the source impedances are known or assumed.

7.5 Summary

In this chapter, metrics for assessing the performance of multi-inlet mufflers are discussed. Both the transmission and insertion loss are defined and methods for evaluating each of the using simulation or experimentally are discussed. The multi-inlet problem can be modeled using either an impedance matrix or superposition approach. Both methods are equivalent. However, the impedance matrix approach is more convenient if numerical simulation is used, and the superposition method is more applicable if experimentally assessed. Both methods are simple to apply if plane wave models are used. In prior work, the impedance matrix for transmission loss had been validated by Jiang et al. (2000). Both approaches were validated for numerical simulation and plane wave

methods. In addition, the insertion loss was determined by measuring the four pole parameters, source strengths and impedances, and termination impedance.

Unlike a single inlet and outlet muffler, the transmission loss of multi-inlet mufflers is dependent to the amplitude ratio and phase difference between sources. It was shown that the phase difference between sources is especially important at low frequencies. Accordingly, engineers can design a muffler which will take advantage of the phase difference between sources.

Chapter 8 CONCLUSION AND RECOMMENDATION

This dissertation was comprised of five self-contained articles. A high level summary of the major conclusions from each article is included in the discussion which follows.

8.1 Micro-Perforated Panel Absorber

A micro-perforated panel absorber should be thought of as a system which includes the perforate itself and the backing cavity. The panel and absorber function as a set of band absorbers. The lowest and widest frequency band can be moved lower in frequency by increasing the cavity depth. It has been shown that broadband sound absorption is achievable by creatively partitioning the backing cavity into channels. Longer channels can be created by folding a channel around other channels. This will enhance the sound absorption at lower frequencies. Several partitioning techniques have been investigated in this work. A two-channel cavity design improved the absorption at low frequencies, and a three-channel design provided better broadband performance. Two other designs (*schizophonium* and triangular prism) were suggested that took advantage of a gradual change in the area of a channel. The results demonstrate that clever backings can be created to significantly improve the sound absorption of MPP absorbers.

The suggested backing cavity designs appear very promising in applications such as HVAC ducting in elementary school classrooms and hospitals where fiberglass and foam should be avoided. In these applications, large cavity volumes can be taken advantage of since space is generally available.

8.2 Diesel Particulate Filters

A diesel particulate filter contains hundreds or even thousands of tiny channels with permeable ceramic walls. An entire acoustic model for a diesel particulate filter (DPF) unit including these channels and walls is extremely resource-consuming. However, a symmetric finite element model for a single channel with

its neighboring channels can be used to determine the properties of the entire filter by taking advantage of the 1-D acoustic behavior inside the channels. The walls between channels are not modeled in detail. Instead, they are modeled using a transfer impedance boundary condition. In finite element software, an element face to element face transfer relationship can be used to implement a transfer impedance.

Results indicate that the orientation and layout of the inlet and outlet ducts can have a significant effect on the transmission loss. This suggests that the orientation and shape of the inlet and outlet ducts are an important design consideration.

8.3 Source Impedance

Acoustic sources are modeled as a combination of a pressure source connected by a series or source impedance to the acoustic domain. That source impedance is mathematically defined as a series impedance though it can alternatively be defined as a parallel impedance. Several direct and indirect experimental approaches have been used to measure the acoustic source impedance. These were reviewed and an approach for simulating acoustic sources in finite element model was introduced.

Results have demonstrated the validity of the approach at low frequencies. Alternatively, the source strength can be modeled as an active term in the transfer relation instead of modeling it as a pressure boundary condition. This model allows the entire system with source and load characteristics to be simulated. Moreover, the insertion loss can be simulated and resonances which lead to negative insertion loss (an amplification of sound by the exhaust system) can be identified and better understood.

8.4 Multi-Inlet Mufflers

Approaches for defining and determining the transmission and insertion loss of a multi-inlet muffler are described. Two approaches can be used. One approach

is based on an impedance matrix that can be computed using either finite or boundary element methods. This approach is especially useful if deterministic methods are used. The other approach is based on the superposition principle. This approach is especially applicable to measurement because measured four-pole parameters are utilized.

It is demonstrated that both the impedance matrix and superposition approaches produce identical results and are equivalent. Both approaches assume that the source is broadband. Unlike a single inlet and outlet muffler, the transmission loss of multi-inlet mufflers is dependent on the amplitude ratio and phase difference between sources. It was shown that the phase difference between sources is especially important at low frequencies. Accordingly, engineers can design a muffler which will take advantage of the phase difference between sources.

Appendix Transmission Loss in Octave Band

Often, sound pressures are measured in octave or third-octave bands. This is a feature of most handheld sound level meters and is a convenient way to condense the amount of data examined. Muffler transmission loss is normally measured in narrow band. However, band results are preferred especially if the source has been measured in octave bands.

One way to convert transmission loss to octave bands is by using a simple averaging approach. The arithmetic mean value of all the transmission loss points within each frequency band is calculated and represents the transmission loss of the entire band. The approach is straightforward and easy to apply. Nevertheless, it is not an energy based approach, which may cause some bias.

Since the transmission loss is defined based on the difference between the incident and transmitted powers, a more proper approach to obtain octave band transmission loss is to first convert the narrow band incident and transmitted powers into octave bands respectively and then calculate the octave band transmission loss. Based on the measured four-pole matrix, the narrow band incident and transmitted powers can be calculated by using the definition of insertion loss.

Insertion loss is the difference of sound power or pressure in dB resulting from the insertion of the muffler in a straight duct. As shown in Figure A.1, the sound pressure level in dB at the end of a straight tube is SPL_1 and the sound pressure level at the end of the tube with an inserted muffler is SPL_2. The insertion loss of the muffler is

$$IL = SPL_1 - SPL_2 \tag{A.1}$$

It is well known that if the source and termination are both anechoic, the transmission and insertion loss of the muffler are identical (Munjal, 1987). In that case, the insertion loss equation can be used with anechoic source and

termination impedances. The sound pressure level without the muffler (SPL_1) is the incident power and with the muffler (SPL_2) is the transmitted power. The difference between these two sound pressure levels (in octave or third-octave bands) will be the transmission loss. The insertion loss in bands is the difference between the incident and transmitted powers in bands.

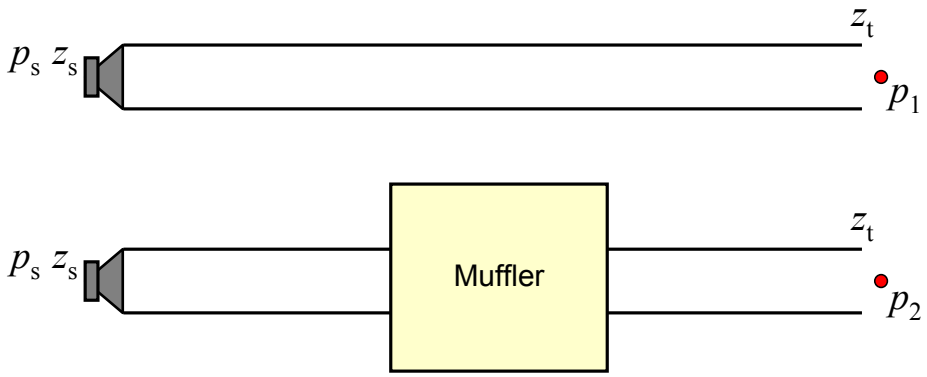

Figure A.1 Schematic of muffler insertion loss.

Assuming a unit source strength for the unit source strength p_s, the sound pressure SPL_1 and SPL_2 can be calculated using the equation

$$SPL_1 = 20\log_{10}\left|\frac{p_s}{\left(T_{11}^{duct} + T_{12}^{duct}/\rho c + T_{21}^{duct}\rho c + T_{22}^{duct}\right)p_{ref}}\right| \quad \text{(A.2)}$$

$$SPL_2 = 20\log_{10}\left|\frac{p_s}{\left(T_{11}^{muff} + T_{12}^{muff}/\rho c + T_{21}^{muff}\rho c + T_{22}^{muff}\right)p_{ref}}\right| \quad \text{(A.3)}$$

where T^{duct} and T^{muff} are the four-pole matrices of the straight duct and the muffler respectively and p_{ref} is the reference sound pressure, which is usually 2×10^{-5} Pa.

The two approaches to obtain octave band transmission loss are compared. The first case is an analytical simple expansion chamber below the plane wave cutoff

frequency. Results are compared in Figure A.2. The second case is a real muffler and the results are compared in Figure A.3.

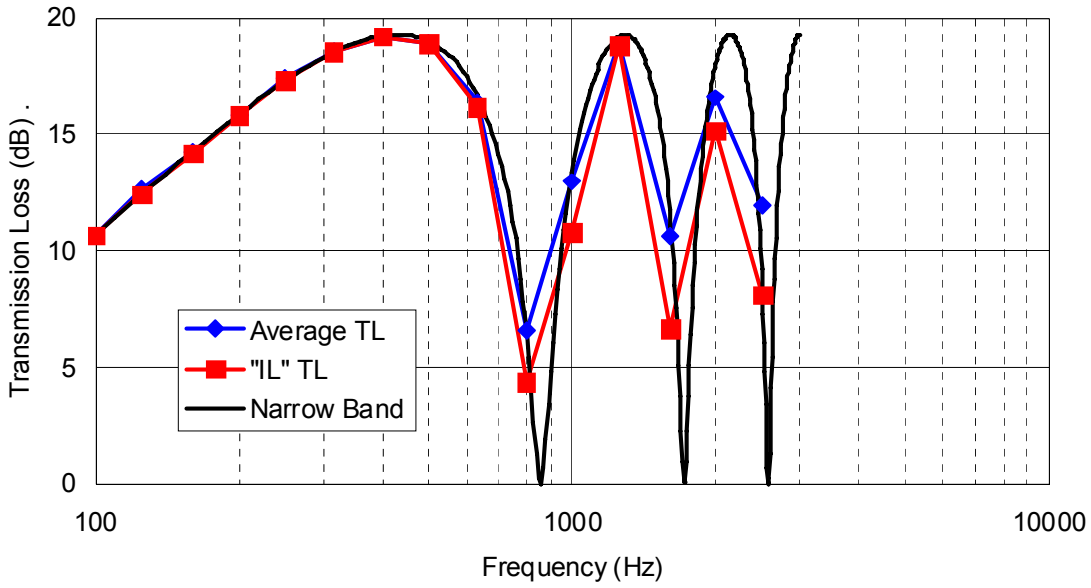

Figure A.2 One-third octave band transmission loss comparison of a simple expansion chamber.

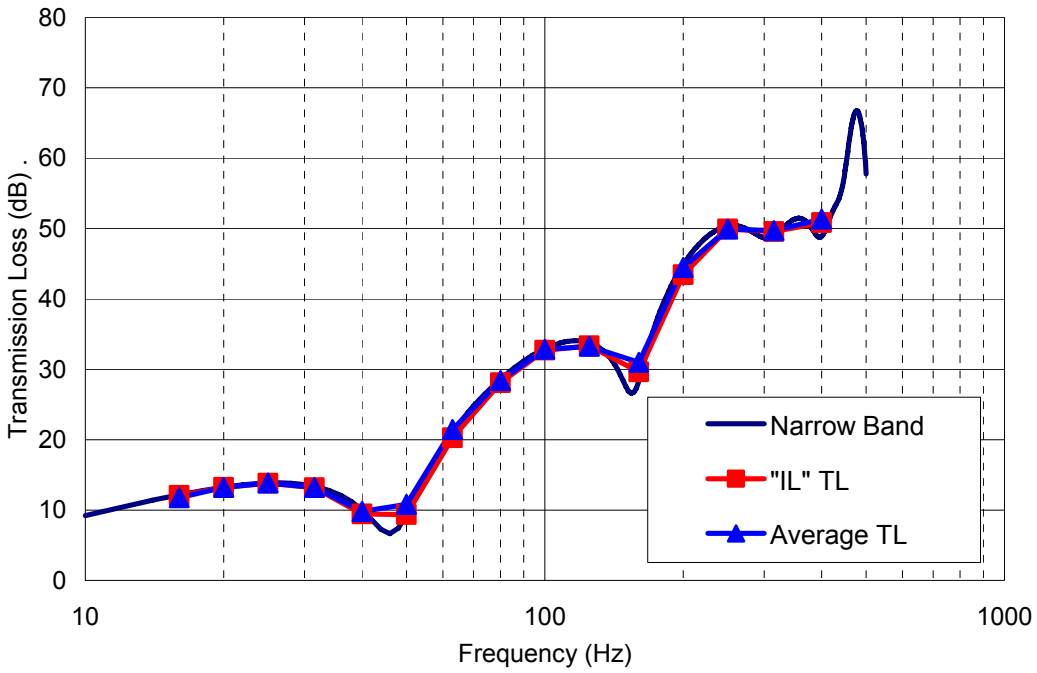

Figure A.3 One-third octave band transmission loss comparison of a real muffler.

References

M. Åbom, (1987). “An Analytical Model for Reactive Silencers Based on Bragg-Scattering,” Journal of Sound and Vibration 112, 384–388.

M. Åbom, and H. Bodén, (1988). “Error Analysis of Two-microphone Measurements in Ducts with Flow,” Journal of the Acoustical Society of America, 83(6), 2429-2438.

M. Åbom, (1990). “Derivation of the Four-pole Parameters Including Higher Order Mode Effects for Expansion Chamber Mufflers with Extended Inlet and Outlet,” Journal of Sound and Vibration, 137(3), 403-418.

M. Åbom, (1992). “A Note on the Experimental Determination of Acoustical Two-port Matrices,” Journal of Sound and Vibration 155(1), 185-188.

ACUPRO (2013). *ACUPRO Measurement System*, SpectronicsInc. USA. www.spectronics.net.

R. J. Alfredson and P. O. A. L. Davies, (1971). “Performance of Exhaust Silencer Components,” Journal of Sound and Vibration 15(2), 175-19.

S. Allam and M. Åbom, (2005). “Acoustic Modelling and Testing of Diesel Particulate Filters,” Journal of Sound and Vibration 288 255-273.

S. Allam and M. Åbom, (2006). “Sound Propagation in an Array of Narrow Porous Channels with Application Diesel Particulate Filters,” Journal of Sound and Vibration 291 882-901.

S. Allam, Y. Guo and M. Åbom, (2009). “Acoustical Study of Micro-Perforated Plates for Vehicle Applications,” SAE Noise and Vibration Conference Proceedings 2009-01-2037, St. Charles, IL.

H. S. Alves and A. G. Doige, (1987). “A Three-load Method for Noise Source Characterization in Ducts”, Noise-Con 87 329-334.

F. Asdrubali and G. Pispola, (2007). “Properties of Transparent Sound Absorbing Panels for use in Noise Barriers,” Journal of the Acoustical Society of America, 121, 214–221.

ASTM Standard, C423-09, (2009). “Standard Test Method for Sound Absorption and Sound Absorption Coefficients by the Reverberation Room Method.”

ASTM Standard C522, (2003). “Standard Test Method for Airflow Resistance of Acoustical Materials.”

ASTM Standard E1050, (1998). “Standard Test Method for Impedance and Absorption of Acoustical Material Using a Tube, Two Microphones and a Digital Frequency Analysis System.”

ASTM Standard E2611, (2009). “Standard Test Method for Measurement of Normal Incidence Sound Transmission of Acoustical Materials Based on the Transfer Matrix Method.”

H. Bodén and M. Abom, (1986). “Influence of Errors on the Two-microphone Method for Measuring Acoustic Properties in Ducts”, Journal of the Acoustical Society of America, Vol. 79, pp. 541-549.

H. Bodén, (1988). “Error Analysis for the Two-Load Method used to Measure the Source Characteristics of Fluid Machines”, Journal of Sound and Vibration, 126, 173-177.

H. Bodén, (1991). “The Multiple Load Method for Measuring the Source Characteristics of Time-Variant Sources”, Journal of Sound and Vibration, 148, 437-453.

H. Bodén, (1992). “Characterization of IC-Engines as Source of Exhaust and Intake Noise”, Proceedings of the 25th ISATA Conference on Mechatronics.

H. Bodén, (1995). “On Multi-Load Methods for Determination of the Source Data of Acoustic One-Port Source”, Journal of Sound and Vibration 180 725-743.

H. Bodén and M. Åbom, (1995). “Modelling of Fluid Machines as Sources of Sound in Duct and Pipe Systems”, Acta Acoustica, Vol. 3, 549-560.

H. Bodén, M. Tonse and R. Fairbrother, (2004). “On Extraction of IC-Engine Acoustic Source Data from Non-linear Simulations,” Proceedings of the 11th International Congress on Sound and Vibration, St. Petersburg, Russia.

T. Bravo, C. Maury and C. Pinhede, (2013). “Enhancing Sound Absorption and Transmission through Flexible Multi-Layer Micro-Perforated Structures,” Journal of the Acoustical Society of America, 134(5) 3663-3673.

R. Corin and L. Weste (2005). “Sound of silence, iVT International,” 105-107.

A. Cummings, (1975). “Sound Transmission at Sudden Area Expansions in Circular Ducts, with Superimposed Mean Flow,” Journal of Sound and Vibration 38, 149–155.

P. O. A. L. Davies and E. A. A. Yaseen, (1987). “High Intensity Sound Propagation in Flow Ducts,” Journal of Sound and Vibration 114, 153–157.

P. O. A. L. Davies, (1988). “Practical Flow Duct Acoustics,” Journal of Sound and vibration 124 91-115.

F. D. Denia, L. Baeza, J. Albelda and F. J. Fuenmayor, (2003). “Acoustic Behaviour of Elliptical Mufflers with Single-Inlet and Double-Outlet,” Tenth International Congress on Sound and Vibration, Stockholm, Sweden.

L. Desmons, J. Hardy, (1994). “A Least Squares Method for Evaluation of Characteristics of Acoustical Sources,” Journal of Sound and Vibration 175 365-376.

E. Dokumaci, (1997). “A Note on Transmission of Sound in a Wide Pipe with Mean Flow and Viscothermal Attenuation,” Journal of Sound and Vibration 208(4), 653–655.

D. Egolf and R. Leonard, (1977). “Experimental Scheme for Analyzing the Dynamic Behavior of Electroacoustic Transducers,” Journal of the Acoustical Society of America, 62 1013-1023.

T. Elnady, (2004). “Modelling and Characterization of Perforates in Lined Ducts and Mufflers (Paper III),” Ph.D. Thesis, the Royal Institute of Technology (KTH), Stockholm, Sweden.

T. Elnady and M. Åbom, (2006). “SIDLAB: New 1D Sound Propagation Simulation Software for Complex Duct Networks,” Proceedings of the 13th for Sound and Vibration, Vienna.

L. J. Eriksson, P. T. Thawani, and R. H. Hoops, (1983). “Acoustical Design and Evaluation of Silencers,” Journal of Sound and Vibration 17(7), 20-27.

F. Fahy, (2001). *Foundations of Engineering Acoustics*, London: Elsevier Academic Press.

R. Fairbrother, H. Bodén and R. Glav, (2005). “Linear Acoustic Exhaust System Simulation Using Source Data from Linear Simulation,” SAE Technical Paper, 2005-01-2358.

A. Galaitsis and E. Bender, (1975). “Measurement of the Acoustic Impedance of an Internal Combustion Engine,” Journal of the Acoustical Society of America, 58, S8.

R. N. Hota, M. L. Munjal and N. K. Mukherjee, (2008). “Evaluation of Engine Acoustic Source Characteristic using AVL BOOST Sofrware,” AVL Advanced Simulation Technologies Indian User Conference.

J. G. Ih and B. H. Lee, (1985). “Analysis of Higher-Order Mode Effects in the Circular Expansion Chamber with Mean Flow,” Journal of the Acoustical Society of America, 77, 1377–1388.

J. Ih and K. S. Peat, (2002). “On the Causes of Negative Source Impedance in the Measurement of Intake and Exhaust Noise Sources,” Applied Acoustics, 63(2) 153-171.

K. U. Ingard and T. A. Dear, (1985). “Measurement of Acoustic Flow Resistance,” Journal of Sound and Vibration, Vol. 103, pp. 567-572.

K. U. Ingard, (1994). *Notes on Sound Absorption Technology* Version 94-02, Noise Control Foundation, New York.

U. Ingard, (2010). *Noise Reduction Analysis*, Jones and Barlett Publishers, London, United Kingdom, pp. 389-395.

ISO 10534-2, (1998). “Acoustics—Determination of Sound Absorption Coefficient and Impedance in Impedance Tubes—Part 2: Transfer-Function Method.”

P. Jackson, (2003). “Design and Construction of a Small Reverberation Chamber,” SAE Noise and Vibration Conference, Traverse City, MI, Paper No. 2003-01-1679.

K. Jayaraman and K. Yam, (1981). “Decoupling Approach to Modelling Perforated Tube Muffler Components,” Journal of the Acoustical Society of America, 69, 390–396.

C. Jiang, T. W. Wu and C. Y. R. Cheng, (2005). “Evaluation of Transmission Loss using the Boundary Element Method for Mufflers with Two Inlets,” Noise-Con 2005, Minneapolis, Minnesota.

C. Jiang, T. W. Wu, M. B. Xu, and C. Y. R. Cheng, (2010). “BEM Modeling of Mufflers with Diesel Particulate Filters and Catalytic Converters,” Noise Control Engineering Journal, Vol. 58, pp. 244-250.

W. Jiang, X. Liu, and C. Wang, (2006). “Some Numerical and Experimental Study of Micro-Perforated Panel Acoustic Absorbers with Heterogeneous Cavities,” ICSV13, Vienna, Austria.

J. Kang and M. W. Brocklesby, (2005). “Feasibility of Applying Micro-perforated Absorbers in Acoustic Window Systems,” Applied Acoustics 66(6) 669–689.

T. Kar, M. L. Munjal, (2005). “Generalized analysis of a muffler with any number of interacting ducts,” Journal of Sound and Vibration 285, 585-596.

M. L. Kathuriya and M. L. Munjal, (1979). “Exprimental Evaluation of the Aeroacoustic Characteristics of a Source of Pulsating Gas Flow,” Journal of the Acoustical Society of America, 65 240-278.

D. H. Keefe, (1984). “Acoustic Wave Propagation in Cylindrical Ducts: Transmission Line Parameter Approximations for Isothermal and Nonisothermal Boundary Conditions,” Journal of the Acoustical Society of America, 75 (1) 58-62.

M. Knutsson, H. Bodén and J. Lennblad, (2005). “On Extraction of IC-Engine Intake Acoustic Source Data from Non-Linear Simulations,” Twelfth International Congress on Sound and Vibration, Lisbon.

D. Lee and Y. Kwon, (2004). “Estimation of the Absorption Performance of Multiple Layer Perforated Panel Systems by Transfer Matrix method,” Journal of Sound and Vibration, Vol. 278, pp. 847-860.

H. Levine and J. Schwinger, (1948). “On the Radiation of Sound from an Un-flanged Circular Pipe,” Physical Review, Vol. 73, pp. 383.

J. Liu, D. W. Herrin, and A. F. Seybert, (2007). “Sound Attenuation Performance of Micro-Perforated Panels,” SAE Noise and Vibration Conference, St. Charles, Illinois, May 15-17, Paper No.2007-01-2196.

J. Liu and D. Herrin, (2009). “Load Effect on Source Impedance Measurement Accuracy,” Proceedings of SAE 2009 Noise and Vibration Conference and Exhibition, St. Charles, IL.

J. Liu, and D. W. Herrin, (2010). “Enhancing Micro-perforated Panel Attenuation by Partitioning the Adjoining Cavity,” Applied Acoustics 71(2) 120-127.

J. Liu, X. Hua, and D. W. Herrin, (2014). “Effective Parameters Estimation for Microperforated Panel Absorbers and Applications,” Applied Acoustics Vol 75 pp. 85-93.

G. Lou, T. W. Wu, and C. Y. R. Cheng, (2003). “Boundary Element Analysis of Packed Silencers with a Substructuring Technique,” Engineering Analysis with Boundary Elements, Vol. 27, pp. 643-653.

T. Y. Lung and A. G. Doige, (1983). “A Time-averaging Transient Testing Method for Acoustic Properties of Piping Systems and Mufflers,” Journal of the Acoustical Society of America, 73 867-876.

D. Y. Maa, (1975). “Theory and Design of Microperforated-panel Sound-absorbing Construction,” Scientia Sinica XVIII 55-71.

D. Y. Maa, (1998). “Potential of Microperforated Panel Absorber,” Journal of the Acoustical Society of America, 104(5) 2861-2866.

D. Y. Maa, (2000). “Theory of Micro Slit Absorbers,” Acta Acustica, 2000-06.

F. Masson, P. Kogan and G. Herrera, (2008). “Optimization of Muffler Transmission Loss by using Microperforated Panels,” FIA2008, Buenos Aires.

F. P. Mechel, P. M. Mertens and W. A. Schilz, (1965). “Research on sound propagation in sound absorbent ducts with superimposed air streams,” AMRL-TR-65-53.

T. Melling, (1973). “The acoustic impedance of perforates at medium and high sound pressure levels,” Journal of Sound and Vibration, Vol. 29, pp.1–65.

T. Melling, (1973). “An impedance tube for precision measurement of acoustic impedance and insertion loss at high sound pressure levels,” Journal of Sound and Vibration, Vol. 28, pp. 23–54.

A. Mimani and M. L. Munjal, (2012). “Acoustical Analysis of a General Network of Multi-Port Elements – An Impedance Matrix Approach,” International Journal of Acoustics and Vibration, Vol. 17, No. 1, pp. 23-46.

C. Morfey, (2001). *Dictionary of Acoustics*, Academic Press, London.

M. L. Munjal, (1987). *Acoustic of Duct and Mufflers*, John Wiley, New York (1987).

M. L. Munjal and A. G. Doige, (1990). “Theory of a Two Source-location Method for Direct Experimental Evaluation of the Four-pole Parameters of an Aeroacoustic Element,” Journal of Sound and Vibration, 141(2), 323-333

M. L. Munjal and R. N. Hota, (2010). “Acoustic Source Characteristics of the Exhaust and Intake Systems of a Spark Ignition Engine,” Inter-noise conference, Lisbon, Portugal.

J. Pan, R. Ming and J. Guo, (2004). “Wave Trapping Barriers,” Proceedings of ACOUSTICS 2004, Gold Coast, Australia.

K. S. Peat, (1988). “A Numerical Decoupling Analysis of Perforated Pipe Silencer Elements,” Journal of Sound and Vibration 123, 199–212.

A. D. Pierce, (1981). *Acoustics, an Introduction to Its Physical Principles and Applications*, McGraw-Hill.

A. D. Pierce, (1991). *Acoustics: An Introduction to Its Physical Principles and Applications*, 2nd ed., Acoustical Society of America, New York.

M. G. Prasad and M. J. Crocker, (1981). “Insertion Loss Studies on Models of Automotive exhaust systems,” Journal of the Acoustical Society of America, 70, 1339-1344.

M. G. Prasad and M. J. Crocker, (1983). “On the Measurement of the Internal Source Impedance of a Multi-Cylinder Engine Exhaust System,” Journal of Sound and Vibration 90 491-508.

M. G. Prasad, (1987). “A Four Load Method for Evaluation of Acoustical Source Impedance in a Duct,” Journal of Sound and Vibration 114(2) 347-356.

K. N. Rao and M. L. Munjal, (1986). “Experimental Evaluation of Impedance of perforate with grazing flow,” Journal of Sound and Vibration 108 283-295.

D. Renneberger, (1967). “Experimentelle Untersuchungen Zum Akustischen Reflexionsfaktor Von Unstetigen Querschnittsänderungen in Einem Luftdurchströmten Rohr,” Acustica, Vol. 19 222-235.

D. Ross and M. J. Crocker, (1983). “Measurement of the Acoustic Internal Source Impedance of an Internal Combustion Engine,” Journal of the Acoustical Society of America, 74(1) 18-27.

H. Ruiz, P. Cobo, and F. Jacobsen, (2011). “Optimization of Multi-layer Microperforated Panels by Simulated Annealing,” Applied Acoustics 72(10) 772-776.

K. Sakagami, M. Morimoto, and W. Koike, (2006). “A Numerical Study of Double-leaf Micro-perforated Panel Absorbers,” Applied Acoustics 67 609-619.

K. Sakagami, T. Nakamori, M. Morimoto, and M. Yairi, (2009). “Double-leaf Microperforated Panel Space Absorbers: A Revised Theory and Detailed Analysis,” Applied Acoustics 70 703–709.

T. Schultz, M. Sheplak, L. Cattafesta, (2007). “Uncertainty Analysis of the Two-microphone Method,” Journal of Sound and Vibration, Vol. 304, pp. 91-109.

A. Selamet and Z. L. Ji, (1997). “Acoustic attenuation performance of circular expansion chambers with offset inlet/outlet: I. Analytical approach,” Journal of Sound and Vibration 213, 407-426.

A. Selamet and Z. L. Ji, (2000). “Acoustic Attenuation Performance of Circular Expansion Chambers with Single-Inlet and Double-Outlet,” Journal of Sound and Vibration 229(1), 3-19.

A. Selamet and Z. L. Ji, (2000). “Acoustic Attenuation Performance of Circular Expansion Chambers with Two End-Inlets/One Side-Outlet,” Journal of Sound and Vibration 231(4), 1159-1167.

A. F. Seybert and D. F. Ross, (1977). “Experimental Determination of Acoustic Properties using a Two-Microphone Random-Excitation Technique,” Journal of the Acoustical Society of America, 61, 1362.

A. F. Seybert, B. Soenarko, (1981). “Error Analysis of Spectral Estimates with Application to the Measurement of Acoustic Parameters Using Random Sound Fields in Ducts,” Journal of the Acoustical Society of America, Vol. 69, pp. 1190–1199.

SIDLAB (2011). *SIDLAB Acoustics User’s Manual*, Version 2.6.

A. F. Seybert, and C. Y. R. Cheng, (1987). “Applications of the Boundary Element Method to Acoustic Cavity Response and Muffler Analysis,” ASME Trans. J. Vib. Acoust. Stress Rel. Des., 109, 15–21.

B. H. Song and J. S. Bolton, (2000). “A Transfer-Matrix Approach for Estimating the Characteristic Impedance and Wave Number of Limp and Rigid Porous Materials,” Journal of the Acoustical Society of America, 107 (3) 1131-1152.

B. S. Sridhara and M. J. Crocker, (1992). “Error Analysis for Four-Load Method Used to Measure the Source Impedance in Ducts,” Journal of the Acoustical Society of America, 92 2924-2931.

J. W. Sullivan, (1979). “A Method for Modeling Perforated Tube Muffler Components. I. Theory,” Journal of the Acoustical Society of America, 66, 779–788.

K. Sum, J. Pan, and S. Peng, (2006) “Use of Parallel Microperforated Panel Subabsorbers for Noise Control in Ducts,” Proceeding of ICSV13, Vienna, Austria.

Z. Tao and A. F. Seybert, (2003). “A Review of Current Techniques for Measuring Muffler Transmission Loss,” SAE Technical Paper No. 2003-01-1653

Z. Tao, B. Zhang, D. Herrin, and A. Seybert, (2005). “Prediction of Sound-Absorbing Performance of Micro-Perforated Panels Using the Transfer Matrix Method,” 2005 SAE Noise and Vibration Conference Proceedings, Traverse City, MI.

Z. Tao, J. Liu, D. W. Herrin, and A. F. Seybert, (2007). “Measurement of Source Impedance for an Intake System,” Inter-Noise 2007, Istanbul, Turkey.

C. W. S. To and A. G. Doige, (1979). “A Transient Testing Technique for the Determination of Matrix Parameters of Acoustic Systems, 2: Experimental Procedures and Results,” Journal of Sound and Vibration, 62, 223-233.

C. W. S. To and A. G. Doige, (1979). “A Transient Testing Technique for the Determination of Matrix Parameters of Acoustic Systems, 1: Theory and Principles,” Journal of Sound and Vibration, 62, 207-222.

M. Toyota and D. Takahashi, (2008). “Sound Transmission through a Microperforated-Panel Structure with Subdivided Air Cavities,” Journal of the Acoustical Society of America, 124(6) 3594-3603.

H. Utsuno, T. Tanaka, T. Fujikawa and A. F. Seybert, (1989). “Transfer Function Method for Measuring Characteristic Impedance and Propagation Constant of Porous Materials,” Journal of the Acoustical Society of America, 86 (2) 637-643.

I. L. Ver and L. L. Beranek, (2006). *Noise and Vibration Control Engineering Principles and Applications*, Chapter 9, John Wiley & Sons, Hoboken, New Jersey.

H. P. Wallin, U. Carlsson, M. Åbom, H. Bodén and R. Glav, (2012). *Sound and Vibration*, Marcus Wallenberg Laboratoriet.

L. S. Wirt, (1975). “Sound-Absorptive Materials to Meet Special Requirements,” Journal of the Acoustical Society of America, Vol. 57, No. 1, pp. 126-143.

Q. Wu, (1988). “Empirical Relations between Acoustical Properties and Flow Resistivity of Porous Plastic Open-Cell Foam,” Applied Acoustics, Vol. 25, 141-148.

M. Q. Wu, (1997). “Micro-Perforated Panels for Duct Silencing,” Noise Control Eng. J. 45(2) 69-77.

T. W. Wu, P. Zhang, C. Y. R. Cheng and A. F. Seybert, (1998). “Boundary Element Analysis of Mufflers with and Improved Method for Deriving the Four-Pole Parameters,” Journal of Sound and Vibration 217 767-779.

T. W. Wu, C. Y. R. Cheng and Z. Tao, (2003). “Boundary Element Analysis of Packed Silencers with Protective Cloth and Embedded Thin Surfaces,” Journal of Sound and Vibration, Vol. 261, pp. 1-15.

M. Yairi, K. Sakagami, M. Morimoto and M. Minemura, (2005). “Acoutical Properties of Microperforated Panel Absorbers with Various Configurations of the Back Cavity,” Proceedings of ICSV12, Lisbon, Portugal.

T. Yoo, (2008). *The Modeling of Sound Absorption by Flexible Micro-perforated Panels*, Doctoral Dissertation, Purdue University.

J. Zou, Y. Shen, J. Yang and X. Qiu, (2006). “A note on the prediction method of reverberation absorption coefficient of double layer micro-perforated membrane,” Applied Acoustics 67 106-111.

VITA

Xin Hua was born in Zhenjiang, China in 1983. He received the Bachelor's Degree of Science in Automotive Engineering from Jilin University, China in 2005. Subsequently, he received the Master's Degree of Science in Automotive Engineering from Jilin University, China in 2007.

In August 2007, he enrolled in the Department of Mechanical Engineering, University of Kentucky. During his graduate years at University of Kentucky, he has published 6 journal articles (first author on 4) and 10 conference proceeding articles (first author on 8) including 2 invited papers in Inter-Noise Conference, Innsbruck, Austria in 2013. In 2013, he was named Outstanding Graduate Student of the Department of Mechanical Engineering. Additionally he received Leo Beranek Student Medal for Excellence in the Study of Noise Control and Michiko So Finegold Awards from the Institute of Noise Control Engineering (INCE) in 2013.

Xin Hua